UNIVERSIDAD NACIONAL DE COLOMBIA

Exploration of hybrid simulation methodologies for the computational study of fluid flow phenomena in airways

Andres Santiago Espinosa Moreno

Universidad Nacional de Colombia
Departamento de Ingeniería mecánica y mecatrónica
Bogotá, Colombia
2022

Exploration of hybrid simulation methodologies for the computational study of fluid flow phenomena in airways

Andres Santiago Espinosa Moreno

Thesis presented as a partial requirement to opt for the degree of:
Magister en Ingeniería - Ingeniería Mecánica

Thesis Advisor:
Ph.D. Carlos Alberto Duque Daza

Line of research:
Thermal and fluid sciences
Research group:
GNUM - Grupo de modelado y métodos numéricos en ingeniería

Universidad Nacional de Colombia
Departamento de Ingeniería mecánica y mecatrónica
Bogotá, Colombia
2022

Dedicatory

To my family, the true reason for my achievements.

Abstract

Exploration of hybrid simulation methodologies for the computational study of fluid flow phenomena in airways

In recent years, numerical simulation has emerged as a robust tool for the analysis of physiological phenomena. The application of computational fluid dynamics (CFD) techniques to the study of biofluids is a constantly growing field, especially the focus given to simulations of blood through the circulatory system and air within the human airways. A high complexity arises in the analysis of these systems. On the one hand, the extension and configuration of the geometrical model (branches, networks), and on the other hand, the multiphysics nature of many of these phenomena. This research work was developed with the aim of exploring methodologies that help to simplify the complexity of simulations associated with biofluids, particularly in human airways. In the first part, a specification of the basic concepts was developed, focusing on the description of the airways and the fluid dynamics associated with air transport in the respiratory system. In turn, a background of numerical simulation applied to biofluids, and a classification of the hybrid simulation methodologies was discussed. In the second part, a first simplification strategy was studied, specifically the use of synthetic airway models. For this purpose, a comparison study of the use of these models vs real patient-specific models was carried out. In addition, a study of the effect of the variation of some morphological parameters on the flow, such as bifurcation angle and carina radius rounding, was developed. In the third part, the implementation and validation of a hybrid simulation methodology was performed, based on a dimensional reduction from the airway homothety ratios. A boundary condition for the pressure, which is the result of this methodology, was implemented in a open source, and tested with two application cases: a study of airways in asthma condition and a study of branch collapse. Finally, general conclusions about the application of the spatial simplification strategy and the use of the hybrid simulation methodology were detailed, as well as recommendations and future work.

Keywords: Computational Fluid Dynamics (CFD), Hybrid Numerical Simulation, Lower Airways, Homothety ratios, Real Airway Patient-Specific, Synthetic Airway Models.

Resumen

Exploración de metodologías de simulación híbridas para el estudio computacional de fenómenos de flujos de fluidos en vías respiratorias

En los ultimos años, la simulación numérica se ha potenciado como una herramienta robusta para el análisis de fenómenos fisiológicos. La aplicación de técnicas de dinámica de fluidos computacional (CFD) para el estudio de biofluidos es un campo en constante crecimiento, en especial, el enfoque dado a las simulaciones de sangre a través del sistema circulatorio y de aire a través de las vías respiratorias. Una elevada complejidad surge en el análisis de estos sistemas. Por un lado, la extensión y la configuración del modelo geometríco (ramificaciones, redes), y por otro, la naturaleza multifisica de muchos fenómenos. Este trabajo de investigación fue desarrollado con la intención de explorar metodologías que ayuden a simplificar la complejidad de las simulaciones asociadas a biofluidos, particularmente en vías respiratorias humanas. En la primera parte, una especificación de los conceptos básicos fue desarrollada, centrándose en la descripción de las vías respiratorias y la dinámica de fluidos asociada al transporte de aire en el sistema respiratorio. A su vez, un background de la simulación numérica aplicada a biofluidos, y la consecución de una clasificación de las metodologías de simulación híbridas, fue discutido. En la segunda parte, una primera estrategia de simplificación fue estudiada, específicamente el uso de modelos sintéticos de vías respiratorias. Para esto, un estudio de comparación del uso de estos modelos contra los modelos reales específicos de paciente fue llevado a cabo. Ademas, un estudio del efecto de la variación de algunos parámetros morfológicos sobre el flujo, como lo son el ángulo de bifurcación y el redondeo de radio de carina, fue desarrollado. En la tercera parte, la implementación y validación de una metodología de simulación híbrida fue realizada, basados en una reducción dimensional a partir de los factores homotéticos de vías respiratorias. Una condición de frontera para la presión, la cual es el resultado de dicha metodología, fue implementada en un software libre, y puesta a prueba con dos casos aplicativos: un estudio de vías respiratorias en condición de asma y un estudio de colapso de ramificaciones. Finalmente, las conclusiones generales acerca de la aplicación de la estrategia de simplificación espacial y del uso de la metodología de simulación híbrida fueron detalladas, así como las debidas recomendaciones y trabajos futuros.

Palabras clave: Dinámica de fluidos computacional (CFD), Simulación numérica híbrida, vías respiratorias inferiores, Factores homotéticos, Modelos de vías respiratorias reales de paciente específico, Modelos sintéticos de vías respiratorias.

Content

Abstract vii

1. Introduction and background 2
1.1. Human respiratory system . . . 3
1.1.1. Morphophysiology . . . 3
1.1.2. Breathing mechanics . . . 5
1.1.3. Respiratory pathophysiology . . . 8
1.2. Numerical simulation of biofluids . . . 9
1.2.1. Hybrid simulation techniques . . . 14

2. Airways fluids dynamics 22
2.1. Mathematical model . . . 22
2.1.1. Governing fluid equations . . . 22
2.1.2. Dimensionless parameters . . . 23
2.2. Numerical methods . . . 24
2.2.1. Pre-processing . . . 24
2.2.2. Solver . . . 25
2.2.3. Post-processing . . . 27

3. Spatial complexity reduction 29
3.1. Real vs Synthetic airways models . . . 29
3.1.1. Specific-patient airways model . . . 29
3.1.2. Synthetic human airways models . . . 30
3.1.3. Numerical method . . . 32
3.1.4. Comparative numerical results between real and synthetic models . . . 32
3.2. Influence of morphological parameters on airway flow . . . 36
3.2.1. Effect of branch bifurcation angle . . . 36
3.2.2. Effect of carina rounding radius . . . 50

4. Reduced dimensional methodology based on homothety airway ratios 57
4.1. Algorithm development and validation . . . 58
4.1.1. Mathematical development and Sensitivity analysis . . . 58
4.1.2. CFD Numerical Validation . . . 60
4.1.3. Algorithm implementation as a OpenFOAM boundary condition . . . 64

4.1.4. Computational cost analysis . . . 71
4.2. Application cases . . . 71
4.2.1. CASE I: Asthmatic human airways . . . 71
4.2.2. CASE II: Patient-specific analysis . . . 75
4.3. Algorithm performance for pulsating flows . . . 79
4.3.1. Pressure and velocity curves analysis . . . 80

5. Conclusions and recommendations **84**
5.1. Conclusions . . . 84
5.2. Recommendations . . . 86

A. Appendix: Compilation files for Boundary Conditions **88**
A.1. pressureHomothetyAirwaysModel . . . 88
A.1.1. pressureHomothetyAirwaysModel.C . . . 88
A.1.2. pressureHomothetyAirwaysModel.H . . . 93
A.2. pressureBetaAirwaysModel . . . 98
A.2.1. pressureBetaAirwaysModel.C . . . 98
A.2.2. pressureBetaAirwaysModel.H . . . 103

Bibliography **109**

Figure list

1-1. Respiratory system composition. Taken from Bair [4] 4
1-2. Volume, pressure, and airflow changes during a single idealized respiratory cycle. Taken from Levitzky [60] 6
1-3. Curves comparison between VCV (left) and PSV (right) modes. Taken from Warner and Patel [116] 8
1-4. Bronchial wall contraction for healthy (left) and asthmatic (right) airways. Taken from West [119] 9
1-5. Velocity streamlines in a Carotid Artery Treated with Stent. Taken from Joel and Anburajan [50] 11
1-6. Numerical study of a prostatic urethra after transurethral surgery. Taken from Zhang et al. [126] 12
1-7. Wall shear stress comparison in healthy and stenotic airways. Taken from Taherian et al. [110] 13
1-8. Weibel's airways model. Taken from Levitzky [60] 13
1-9. Nonlinear single-compartment model of the lung. Taken from Bates [6] . . . 16
1-10.Parts of the hybrid airway model. Taken from Ismail et al. [48] 17
1-11.Continuous micro solution-intermittent coupling (CI) method. Taken from Fan et al. [31] 18
1-12.Particle dispersation in airways single model. Taken from Chen et al. [21] . . 19
1-13.CFD vs Hybrid CFD+DEM simulation. Taken from Ponzini et al. [92] . . . 20
1-14.Comparison between rigid and flexible walls. Taken from Xia et al. [123] . . . 20

2-1. CFD structure process 24
2-2. Indicative scheme of the zones and points where the results are reported . . 28

3-1. Step 1 and 2 in the specific-patient airways model generation 30
3-2. Step 3 and 4 in the specific-patient airways model generation 31
3-3. Models comparison 31
3-4. Velocity streamlines for Re=500 33
3-5. Wall pressure distribution for Re=2000 34
3-6. Wall shear stresses for Re=2000 35
3-7. Location of Maximun WSS for real model. Re 2000 35
3-8. Aiways tree with the notation described by Christou et al. [24] 37
3-9. Velocity profiles on coronal plane 39

3-10.Velocity profiles on sagittal plane . . . 40
3-11.Velocity profiles at exhalation stage for TRA branch . . . 41
3-12.V-W profile (taken at coronal plane) and secondary flow patterns in LMB airway. Inhalation stage. . . . 42
3-13.V-W profile (taken at coronal plane) and secondary flow patterns in LLB airway. Inhalation stage. . . . 43
3-14.V-W profile (taken at coronal plane) and secondary flow patterns in LLU airway. Inhalation stage. . . . 44
3-15.V-W profile (taken at coronal plane) and secondary flow patterns in TRA airway. Exhalation stage. . . . 45
3-16.V-W profile (taken at saggital plane) and secondary flow patterns in TRA airway. Exhalation stage. . . . 46
3-17.V-W profile (taken at coronal plane) and secondary flow patterns in LMB airway. Exhalation stage. . . . 47
3-18.Pressure drops across the axial axes of the branches at inhalation stage . . . 48
3-19.Pressure drop coefficient (Cp) vs Reynolds number . . . 48
3-20.Pressure drops across the axial axes of the branches at exhalation stage . . . 49
3-21.Wall Shear Stress on inner wall for inhalation . . . 49
3-22.Wall Shear Stress on outer wall for exhalation . . . 50
3-23.Bifurcation model geometry . . . 52
3-24.Refinement near the carina . . . 53
3-25.Velocity profiles on coronal plane. Taken at 20 % of the LMB length . . . 53
3-26.Velocity profiles on coronal plane. Taken at 50 % of the LMB length . . . 54
3-27.Velocity profiles on sagittal plane. Taken at 20 % of the LMB length . . . 54
3-28.Velocity profiles on sagittal plane. Taken at 50 % of the LMB length . . . 54
3-29.Vorticity profile on coronal plane. Taken at 20 % of the LMB length . . . 55
3-30.V-W profile (taken at coronal plane) and secondary flow patterns in LMB airway. . . . 55
3-31.Pressure drop through the branch inner wall . . . 56
3-32.Wall Shear Stress on inner wall for inhalation . . . 56

4-1. Standard deviation for 0 to 16 generation tree using aleatory homothety and beta factors . . . 61
4-2. Pressure drop comparison for *Homothety model* . . . 63
4-3. Pressure drop comparison for *Beta model* with $\beta = 6$ . . . 63
4-4. Pressure drop comparison for *Beta model* with $\beta = 3{,}25$ . . . 64
4-5. OF-BC workflow . . . 65
4-6. Models used in CFD validation . . . 67
4-7. Pressure drop comparison for *Homothety model* . . . 68
4-8. Pressure drop comparison for *Beta model* with $\beta = 6$ . . . 68

4-9. Velocity profile comparison for *Homothety model* 69
4-10.Velocity profile comparison for *Beta model* 69
4-11.Wall shear stress comparison for *Homothety model* 70
4-12.Wall shear stress comparison for *Beta model* 70
4-13.Homothety and beta factor for healthy airways 73
4-14.Homothety and beta factor for asthmatic airways 73
4-15.Wall pressure distribution. Items (a) and (c) taken from Tsega and Katiyar [111] 74
4-16.Healthy and asthmatic airways comparison 76
4-17.Real specific-patient airways model 77
4-18.Velocity streamlines for Re=500 78
4-19.Pressure wall distribution for Re=1600 78
4-20.Wall shear stresses for Re=1600 79
4-21.Pressure vs time comparison. Wo = 8.29 81
4-22.Pressure vs time comparison. Wo = 4.14 81
4-23.Pressure and velocity vs time at trachea probe. Wo = 8.29 82
4-24.Pressure and velocity vs time at generation 1 probe. Wo = 8.29. The red lines represent the points where for a maximum pressure, there is a minimum velocity. 82

Table list

1-1. Reference values for resting breathing 7
1-2. Dimensions of healthy (relaxed) and asthmatic (contracted) airways. Model proposed by Wiggs et al. [121] 10

3-1. 5 Generation Model parameters 32
3-2. Comparison of maximum values 34
3-3. Weibel's model parameters in the first three generations 36
3-4. Subcarinal angles obtained by Haskin and Goodman [42] 38
3-5. Model Parameters values 51

4-1. Model parameters for sensitivity analysis 60
4-2. Model parameters for CFD validation 61
4-3. Parameters for *Homothety* and *Beta* models 62
4-4. Computational cost analysis 71

1. Introduction and background

The human body is a structured organism made up of a large number of systems with specific functions. From the muscles and skeleton, to the respiratory and reproductive systems, each of these systems works and interacts with the others in order to maintain life. Some of these processes carried out inside the body involve the transport of a fluid (more commonly known as *biofluids*), covering blood circulation, urine production, saliva generation or air transport, among others. The main human biological systems associated with fluid transport are:

- ◇ The ***circulatory system*** has the function of transporting blood through the body. The blood is a non-Newtonian fluid containt living cells and plasma (Formaggia et al. [35]). As Shi et al. [102] indicates, the circulation can be divided according to its functionality into: pulmonary, which refers to the transport of blood to the lungs and its respective oxygenation process; and systemic, which refers to the distribution of blood to the rest of the organs. The circulatory system consists of the four chamber heart, the aorta/pulmonary artery, main and small arteries, arterioles, capillaries, venules, veins, and vena cava/pulmonary vein.

- ◇ The ***urinary system***, as illustrated by Marieb and Hoehn [67], has as its main function the elimination of waste products (toxins, drugs), the regulation of homeostasis (water balance, red cell production, and others) and converting vitamin D into its active form. This system is composed of kidney, renal vein, renal artery, ureter, urinary bladder and urethra (Sherwood [101]). The fluid transported by this system is urine. Urine is a fluid that, as denoted by studies such as those carried out by Kren et al. [56] and Herranz et al. [43], is generally described as Newtonian, although under certain compositional considerations it may behave as non-Newtonian fluid.

- ◇ The ***lymphatic system*** has the main function of regulate the amount of fluids in the human body, and nowadays, as described by Nipper and Dixon [80], it has also been shown to be relevant in the generation of immune cells and in pathological processes such as cancer and tissue inflammation. This system is composed, as indicated by Swartz [109], by lymph nodes, capillaries, collecting vessels, trunks, and ducts. The fluid transported by this system is the lymph, a liquid which, like blood, contains white blood cells.

- ◇ The ***respiratory system*** is the main focus of this research work. Therefore, a more detailed description of the study is presented below.

1.1. Human respiratory system

As indicated by West [120], the human respiratory system is responsible for the transport of oxygen from the outside into the venous blood, and carbon dioxide in the opposite direction. The respiratory morphophysiology, breathing mechanics and the main pathologies that affect this system are briefly described in this section.

1.1.1. Morphophysiology

The respiratory system is analyzed by Bair [4] as a succession of three zones: extrathoracic region, tracheobrochial region and the alveolar region. This distribution and its respective components can be seen in the Figure **1-1**. The particularities of each of the regions are presented in the following diagram:

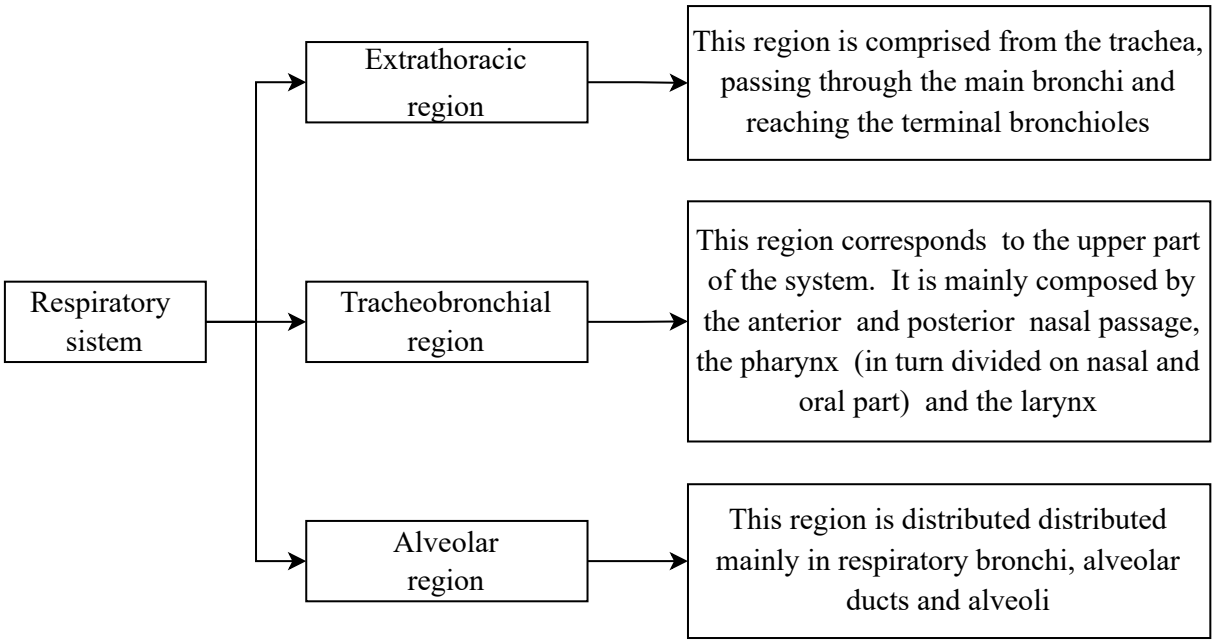

In a similar manner, authors such as West [120] and Finucane et al. [34] identify two regions into which the airways are divided: lower and upper. The upper airway begins in the nose, continuing to the oral cavity and pharynx (being then an analogy to Extrathoracic region). On the other hand, the lower airway comprise the Tracheobronchial and alveolar region. As discussed by West [120], this region is divided in the following parts:

1. **Conducting zone**

   Its main function is the transport of air from the upper airways to the respiratory transition zone. This area consists of:

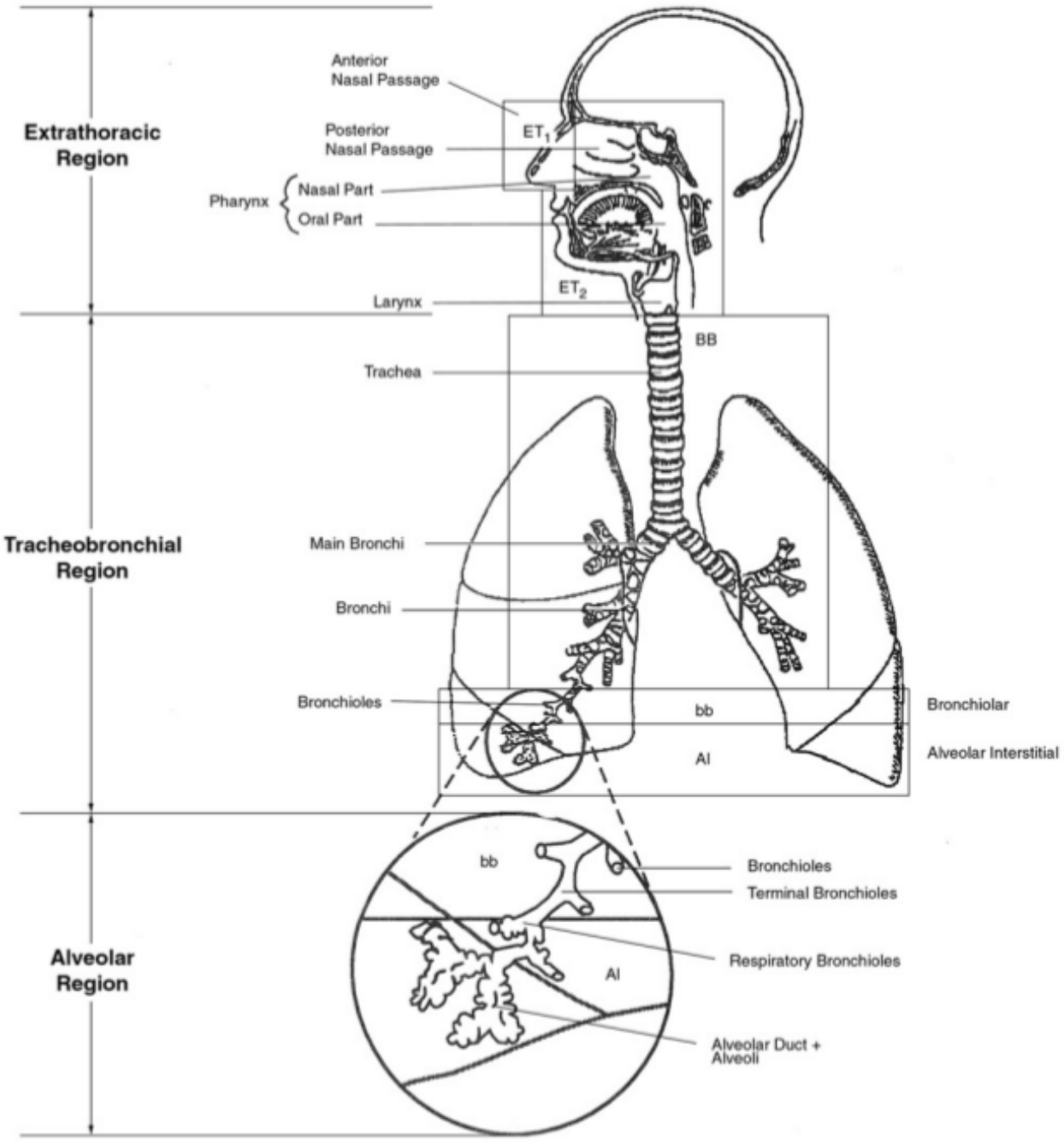

Figure 1-1.: Respiratory system composition. Taken from Bair [4]

- ***Trachea:*** As explained by Minnich and Mathisen [72], the trachea extends from the lower border of the cricoid cartilage to the carina, this being the exact point of bifurcation. Its dimensions range from 2.3 cm (measured in the coronal plane) to 1.8 cm (measured in the sagittal plane) for the diameter, while the length varies

between 10 cm and 13 cm. The trachea are compsed by cartilaginous rings, as indcated Levitzky [60].

- ***Main bronchi:*** At the carina point the airways divide into two branches known as main bronchi. Generally, as indicated by Suarez et al. [108], the right main bronchus is shorter than the left main bronchus. In turn, the right bronchus divides into three lobar bronchi and the left bronchus divides into two lobar bronchi.
- ***Bronchioles:*** the bronchioles are branches coming from the main bronchi. Their main characteristic is that they do not have cartilaginous rings, so they are prone to collapse (Levitzky [60]).

2. **Transitional and respiratory zone**

   Comprised from the respiratory bronchioles to the alveolar sacs. Its function involves gas exchange. This area consists of:

   - ***Respiratory Bronchioles:*** The respiratory bronchioles supply the smallest anatomic unit of the lung, i.e the pulmonary lobule (Suarez et al. [108]). In addition, each of these contain a number of alveolar ducts varying from 2 to 11. As stated by Basil and Morrisey [5], the respiratory bronchioles are involved in obstructive pathologies of the respiratory system such as COPD.
   - ***Alveolar ducts:*** as explained by Suarez et al. [108], alveolar ducts are structures that have a wall formed by alveoli and sparse bundles of smooth muscle
   - ***Alveolar sacs:*** the alveolar sacs are the last structure found in the morphology of the airways, and are mainly responsible for gas exchange. As reported by Suarez et al. [108], each alveolar duct is derived from six alveolar sacs.

1.1.2. Breathing mechanics

The human breathing cycle can be either natural or assisted (i.e., using mechanical ventilation techniques). The two types are summarized below:

1. **Natural breathing**

   As described by Aliverti and Pedotti [3], the act of breathing is due to the generation of a pressure gradient between the environment and the alveolar zone. ***Alveolar pressure*** is the air pressure contained in the alveoli. As indicated by Levitzky [60], when discussing breathing mechanics it is convenient to assume a value of 0 cmH_2O for atmospheric pressure. Thus, if the alveolar pressure is less than atmospheric pressure it is considered as *negative pressure breathing*. During the process of respiratory *inhalation*, the alveolar pressure is lower than the atmospheric pressure, and the internal muscles (mainly the diaphragm and the externals intercostals) are contracted allowing the increase of thoracic space, inciting the transport of air from the nose. On the other

hand, during respiratory *exhalation*, relaxation of the internal muscles and pulmonary elastic recovery influence the outflow of carbon dioxide from the alveolar zone to the exterior.

In a breathing process, the ***tidal volume*** is the volume of air that circulates during inhalation and exhalation of breath. Figure **1-2** shows the curves for an idealized breathing cycle, with a flow rate of 0,5 L/s. It can be seen how during inhalation (from 0 to 2 seconds) the alveolar pressure varies between 0 cmH_2O and -1 cmH_2O, thus producing the gradient with the environment, being this negative value the reference for inhalation. Then, during the other two seconds, the positive alveolar between 0 cmH_2O and 1 cmH_2O pressure value indicates exhalation.

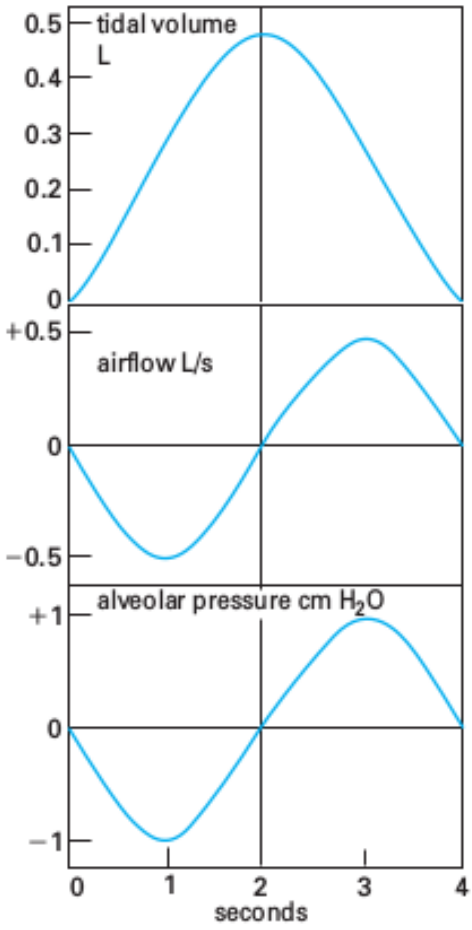

Figure 1-2.: Volume, pressure, and airflow changes during a single idealized respiratory cycle. Taken from Levitzky [60]

In the Figure **1-2**, the 4 seconds represent one breathing cycle. To know the respiration rates it is enough to see how many cycles are repeated in one minute. Some reference values for resting breathing depending on the age are shown in Table **1-1**.

Age	Breaths per minute
Birth to 6 weeks	30-60
6 months	25-40
3 years	20-30
6 years	18-25
10 years	15-20
Adults	12-20

Table 1-1.: Reference values for resting breathing

2. **Mechanical ventilation**

   Mechanical ventilation, as discussed by Gutiérrez Muñoz [41], is a therapeutic alternative that provides patients with respiratory failure the support to be able to perform the breathing process in an unnatural way. This implies that the pressure gradient previously generated naturally will now be produced through a machine known as a mechanical ventilator. This process can be both invasive and non-invasive. As stated by Castillo et al. [17], invasive ventilation requires orotracheal intubation, which involves the introduction of a tube from the upper airway into the trachea. In contrast, noninvasive ventilation is performed through face masks or nasal masks, avoiding intubation.

   Some modes of mechanical ventilation are:

   - ◇ **Volume assist-control ventilation (VCV)** is a ventilation model characterized by the control tidal volume, being delivered as a natural response to the patient's inspiratory effort. As indicated by Warner and Patel [116], this process generates a decrease in the work of breathing, thus generating adequate oxygenation.
   - ◇ **Synchronized Intermittent Mandatory Ventilation (SIMV)** is a ventilation mode with a similar configuration to VCV, but with the addition of a pre-set pressure to support spontaneous breathing.
   - ◇ **Pressure-Support Ventilation (PSV)** is a ventilation which the controlled support pressure. As explained by Warner and Patel [116], this method is the evolution of SIMV, as it focuses on increasing the patient's spontaneous inspiratory effort by controlling positive airway pressure.
   - ◇ **High frequency oscillatory ventilation (HFOV)** is a mechanical process that, as discussed by Choi et al. [22], has the particularity of working with small tidal volumes and a higher breathing frequency. It is currently a technique used especially in neonatal patients. As shown in the study by Bauer and Brücker [7], HFOV is an efficient technique for airway reopening.

Figure 1-3 show the comparative curves for airflow and pressure vs time for VCV and PSV modes.

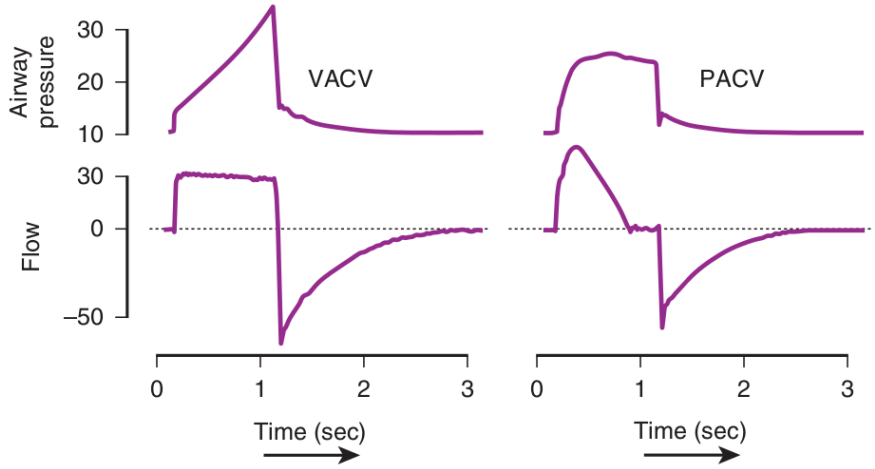

Figure 1-3.: Curves comparison between VCV (left) and PSV (right) modes. Taken from Warner and Patel [116]

1.1.3. Respiratory pathophysiology

The focus of pathophysiology is the study of diseases of living systems. As described by West [119], the respiratory system can develop four types of pathologies:

1. **Obstructive diseases:** As the name implies, they are those that generate an alteration of the surrounding flow due to obstructions. The most common cases are asthma, chronic obstructive pulmonary disease (COPD) and chronic bronchitis.

2. **Restrictive diseases:** these are characterized by affecting lung expansion, mainly due to parenchymal diseases, pulmonary fibrosis and pleural diseases.

3. **Vascular diseases:** These are those that affect in some way the normal blood flow. The most common cases are pulmonary edema, pulmonary embolism and pulmonary hypertension.

4. **Environmental and other diseases:** This type refers mainly to diseases produced from the inhalation of particles and pollutants. Cases such as bronchial carcinoma, pneumoconiosis or tuberculosis are caused by inhaled external agents.

In this research work, special attention was paid to obstructive diseases, particularly asthma and COPD, since some numerical simulation methodologies will be evaluated on airways with these conditions. The basic concepts of these two diseases are cited below:

- **Asthma** According to data from the study conducted by Lambrecht and Hammad [58], more than 300 million people around the world are affected by this pathology. As defined by West [119], asthma manifests as a narrowing of the airways. This contraction can be generated due to asthmatic antigens, some infections or even an exercise-induced case. As shown in Figure **1-4**, the decrease in the cross-sectional area of the branches is due to several aspects: on the one hand, the inner muscle of the airway wall undergoes hypertrophy, generating a contraction. On the other hand, an increase in the size of the mucous glands is evident, as well as the generation of mucus inside the branch.

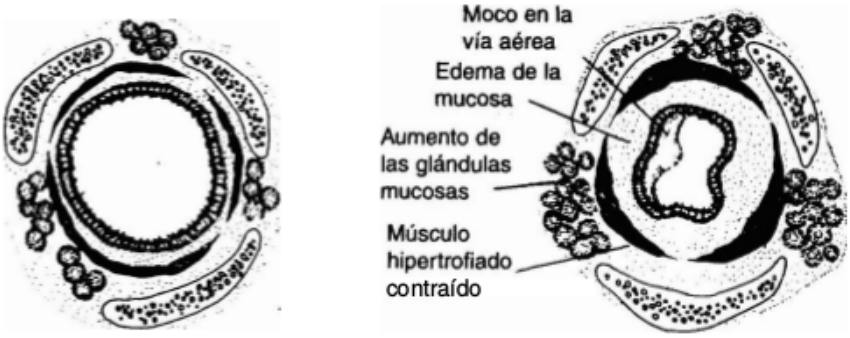

Figure 1-4.: Bronchial wall contraction for healthy (left) and asthmatic (right) airways. Taken from West [119]

- **Chronic Obstructive Pulmonary Disease (COPD)**

  Similar to asthma, the The Chronic Obstructive Pulmonary Disease (COPD) is characterized by a progressive decrease in the cross-sectional area of the airways, with the difference that this phenomenon is due to inflammation and widening of the walls. As Johari et al. [51] emphasizes, at least 12 million people worldwide have been diagnosed with COPD.

Some research efforts have focused on the physiological characterization of the airways with asthma and COPD condition. In the study carried out by Wiggs et al. [121], the dimensions of a tracheobronchial tree in an asthmatic condition were characterized. Table **1-2** shows these contracted dimensions against healthy airways for generation 0 to 16, covering the conducting zone. It can be seen how this narrowing affects only the cross section, while the lengths remain unchanged. In a subsequent study, Wiggs et al. [122] used the same model to analyze the effect of airway wall thickness on asthma and COPD conditions.

1.2. Numerical simulation of biofluids

The study of the behavior of fluids transported in the human body is a field of special interest to medicine and science. Over the years, numerical simulation has proven to be an efficient

Gen	Airways	Airway length [cm]	Relaxed diameter [cm]	Contracted diameter [cm]
0	1	12.000	1.800	1.340
1	2	4.782	1.221	0.909
2	4	1.906	0.828	0.501
3	8	0.760	0.562	0.250
4	16	1.267	0.445	0.197
5	32	1.069	0.351	0.154
6	64	0.901	0.281	0.122
7	128	0.761	0.227	0.098
8	256	0.642	0.186	0.079
9	512	0.541	0.154	0.065
10	1024	0.457	0.130	0.054
11	2048	0.385	0.110	0.045
12	4096	0.325	0.095	0.038
13	8192	0.274	0.083	0.032
14	16384	0.231	0.073	0.028
15	32768	0.195	0.065	0.024
16	65536	0.165	0.059	0.021

Table 1-2.: Dimensions of healthy (relaxed) and asthmatic (contracted) airways. Model proposed by Wiggs et al. [121]

and robust tool for the analysis of biofluid phenomena, given the possibility of solving the governing equations over highly complex geometries and physiological domains.

One of the systems most explored through computational simulation is the ***circulatory system***. The phenomena associated with blood transport present a complexity associated with the non-Newtonian nature of the fluid. Some studies, such as the one developed by Chen et al. [19], focus on analyzing the effect between the Newtonian and non-Newtonian consideration of the blood. Other investigations have focused on phenomena associated with the morphophysiology of veins and arteries, such as those developed by Perktold and Hilbert [89] and Politis et al. [91]. Likewise, numerical simulation is also applied in the study of pathologies associated with circulation, as well as devices and equipment to treat these diseases. Research on cerebral aneurysms (Berg et al. [11]), ven Hypertension with and without Thrombosis (Petkova et al. [90]) and the analysis of fluid dynamics behind blood pumps (Behbahani et al. [9]) are examples of these approaches. Joel and Anburajan [50] develops a study of the functioning of an artery with a stenosis condition and its respective treatment with a stent. His results show that, as illustrated in the Figure **1-5**, the thinning produced by the stenosis generates an increase in velocity (and thus in shear stresses), an

effect that is counteracted by the reopening generated by stent placement.

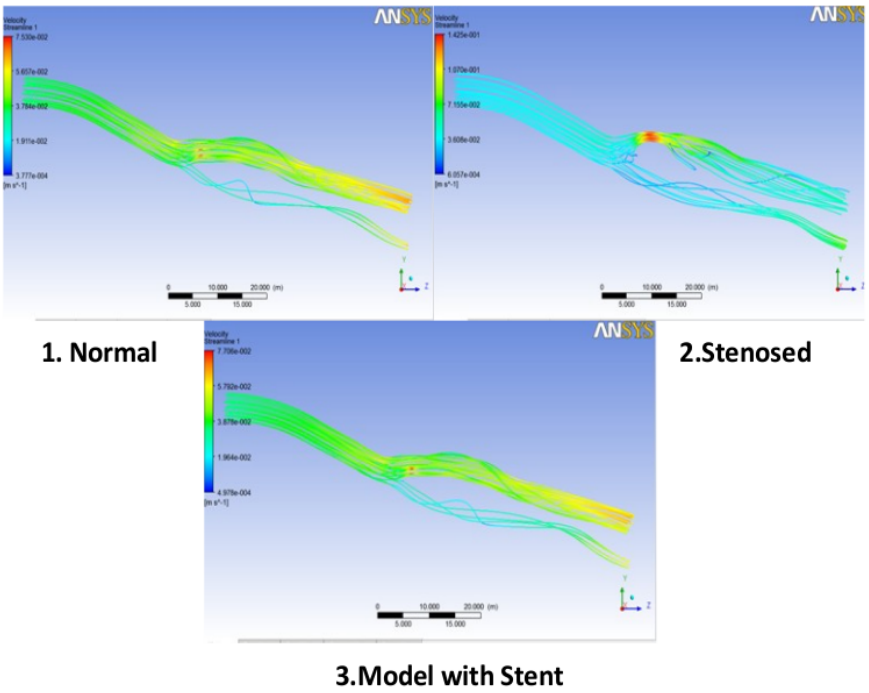

Figure 1-5.: Velocity streamlines in a Carotid Artery Treated with Stent. Taken from Joel and Anburajan [50]

The ***urinary*** and ***lymphatic systems*** are also studied by numerical simulation. As with the circulatory system, the complexity of the nature of the fluid presents a challenge for these studies. The distributions of pressure, velocity and shear stresses in the urethra are discussed in the research implemented by Niu and Chang [81]. The analysis of diseases and post-surgery is reflected in some studies, such as the one performed by Zhang et al. [126], who developed an investigation on urine flow in prostatic urethra after transurethral surgery using computational fluid dynamics techniques (CFD). The morphological basis and the velocity fields obtained with the numerical model can be seen in Figure **1-6**. A similar work in the urine flow in a stented ureter with no peristalsis were carried out by Kim et al. [55]. Current developments have demonstrated the relationship of the lymphatic system to diseases such as cancer. In fact, the study conducted by Shojaee and Niroomand-Oscuii [103] focused on the uptake and elimination of drugs through vascularized cancer tissue, based on the numerical modeling of some parameters associated with the lymph.
Along with the circulatory system, the ***respiratory system*** is one of the most frequently analyzed using numerical models. One of the main applications is based on the study of diseases and pathologies of the airways, with studies on asthma and COPD, such as those carried out by Tsega and Katiyar [111],Chowdhary et al. [23], Yang et al. [124] and Mutuku et al. [77] or the analysis of airways with stenosis conditions carried out by Malve et al. [65],

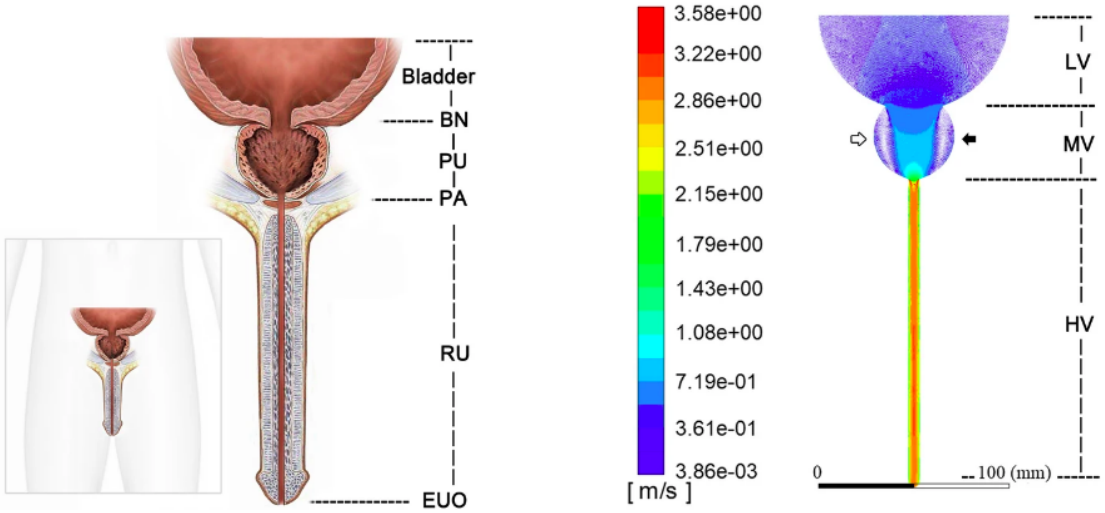

(a) Prostatic urethra anatomy (b) Velocity magnitud

Figure 1-6.: Numerical study of a prostatic urethra after transurethral surgery. Taken from Zhang et al. [126]

Brouns et al. [14] and Taherian et al. [110]. The Figure **1-7** illustrates the cross-sectional thinning effect of the stenosis, which is evidenced as an increase in the shear stresses developed in the human trachea. Another extensively studied topic is the analysis of particle transport and deposition. Some investigations, such as those carried out by Ciloglu and Karaman [25], Lal [57] and Hofmann [44], show that the highest concentration of particles aspirated through the pathways is concentrated in the carina and subsequent bifurcation points.

All numerical studies performed on human airways require computational domain. This domain is obtained from the discretization of the branched geometry. In general, two types of geometries are employed:

1. The *synthetic models* are developed as a geometrical simplification of the airways, since they describe the branches as pipes of known diameter, length and angles. One of the most complete and widely used model was performed by Weibel et al. [117]. From experimentation and statistical methods he developed a model of morphological characterization of the entire bronchial tree. This model provides information on lengths, diameters and cross-sectional areas for each of the 24 generations starting from the trachea, i.e. generation 0, and ending at the alveolar sacs, i.e. generation 23. The dimensions and distribution of the model developed by Weibel et al. [117] are shown in Figure **1-8**. The zones described above can be clearly identified, with the conduction zone comprising the first 17 generations, and the respiration and transition zones the next 6. The study performed by [61] using an advanced MRI method showed how Weibel's model prescribes, in a very accurate way, the average dimensions of a random

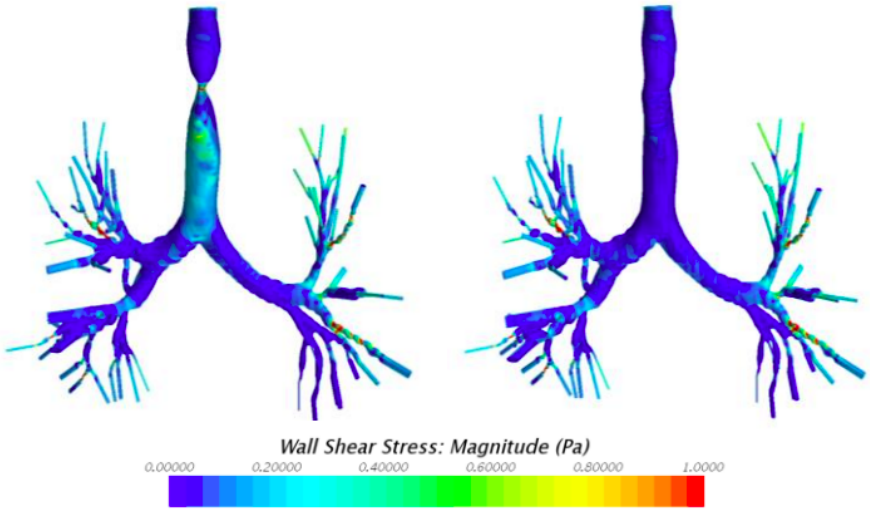

Figure 1-7.: Wall shear stress comparison in healthy and stenotic airways. Taken from Taherian et al. [110]

group of measured patients.

	Generation		Diameter, cm	Length, cm	Number	Total cross-sectional area, cm^2
Conducting zone	trachea	0	1.80	12.0	1	2.54
	bronchi	1	1.22	4.8	2	2.33
		2	0.83	1.9	4	2.13
		3	0.56	0.8	8	2.00
	bronchioles	4	0.45	1.3	16	2.48
	terminal bronchioles	5 ↓ 16	0.35 ↓ 0.06	1.07 ↓ 0.17	32 ↓ 6×10^4	3.11 ↓ 180.0
Transitional and Respiratory zones	respiratory bronchioles	17 18 19	↓ 0.05	↓ 0.10	↓ 5×10^5	↓ 10^3
	alveolar ducts	T_3 20 T_2 21 T_1 22	↓	↓	↓	↓
	alveolar sacs	T 23	0.04	0.05	8×10^6	10^4

Figure 1-8.: Weibel's airways model. Taken from Levitzky [60]

2. The *real patient-specific models*, which are obtained from the segmentation of medical images, coming from the computed axial tomography of a human thorax. The Figure **1-7** is an example of this type of model. A highly accurate digital model is obtained by Schmidt et al. [97] from a segmentation process known as the threshold method. This model was later used by Gemci et al. [39] to develop one of the first numerical studies using a large number of generation (more than 16), although with a high computational cost, as Gemci et al. [39] indicates.

Complexity of airways numerical simulations

As shown in Figure **1-8**, the number of branches in the human airways grows in 2^N exponential form, with N being the number of generations. This results in a total of 65536 branches at the end of the driving zone. This highlights one of the main problems of airway simulations: **dimensional complexity**. The development of synthetic models is a process that can become difficult and tedious as it progresses through the generations, even leading to clashes and interferences between branches that are impossible to avoid. In turn, this is also reflected in the real patient-specific models, since as the number of branches increases, the segmentation process becomes more complex and the result more erratic, resulting in low-quality 3D models. In addition, from the various applications described above, a second problem of complexity arises: the **multiphysics nature of many phenomena**. Flows with dispersion of particles and contaminants, deformation and movement of airway walls during inhalation and exhalation processes, are examples of problems that require the application of different techniques to be solved. One of the implications of the situations described above is the **high computational cost**, evidenced mainly by long simulation times and the need to use high-performance computing machines. In order to solve these and other problems associated with numerical airway simulations, **hybrid simulation techniques** have been developed as tools capable of solving highly complex cases, and with reduced computational costs relative to other simulation strategies.

1.2.1. Hybrid simulation techniques

Hybrid simulation techniques are developed with the aim of reaching the numerical solution of complex problems, based on methodologies that simplify the computational execution. For biofluidic phenomena, hybrid strategies usually focus on three main techniques: *Reduced Dimensional Models*, *Temporal coupling techniques* and *coupled algorithms*. A brief description of these techniques is given below.

- **Reduced Dimensional Models**

  In the analysis of branched systems, the techniques associated with the management of spatial scales are presented as an ideal tool for the simplification and generalization of

the system under study. Within the field of biofluids, the coupling of 3D to 0D models have been extensively studied, where:

- ◇ *0D models* are those based on basic principles and analogies, such as electrical analogies, impedance, mechanical analogies, and others.
- ◇ *1D models* are linear or nonlinear models represented through the coupling of differential equations. For example, the equations derived from the representation of any system as a spring-damper mechanism.
- ◇ *2D models* involve the solution of the governing equations over a domain in a two dimensional space.
- ◇ *3D models*, similar to 2D models, involve solving the governing equations over a domain in a tridimensional space.

One of the most employed coupled algorithms for blood simulations was develop by Olufsen [82]. Considering the small arteries like a tree structure, a pressure boundary condition based on a 0d impedance model was implemented in his study. The novelty of this boundary condition is that it allows taking into account the effects associated with the wall mechanics, since it involves the elastic properties of the wall. By applying this condition to 2D and 3D models, an effective dimensional simplification is obtained that allows a more accurate assessment of blood flow. This model has been extended to a large number of applications and studies such as performed by Olufsen et al. [83], Steele et al. [107] and Colebank et al. [26]. As with this impedance approach, there are other models developed that attempt to look for spatial reduction in blood flow simulations. The mathematical model implemented by Blanco et al. [13] for pulsatile flows is based on integrating the axial component of the momentum equation, a 1D model that modifies the Womersley velocity profiles at each simulation step.

In a similar manner to the study of blood flow, the analysis of the airflow within the human airways has implemented the use of dimensional reduction methodologies. In early studies of pressure drops across the respiratory system developed by Pedley (Pedley et al. [86], Pedley et al. [88], Pedley et al. [87]), experiments and validations on airway models were developed. The results allowed to characterize the behavior of air resistance and pressure through the branches as a as 0d model derived from a Hagen-Poiseuille flow resistance. A complete description of the respiratory system based on 1D models is developed by Bates [6]. starting with a simple linear model that describes system pressures and fluid resistance through a differential equation. A more complete model can be seen in Figure **1-9**. In this model, the nonlinearity of the mechanical properties of the lung is taken into account.

From the incorporation of electromechanical analogies, Bates [6] extends the capability of the model by considering mechanical properties such as elastance and compliance. A second orden differential equations was obtained. This model have the ability to

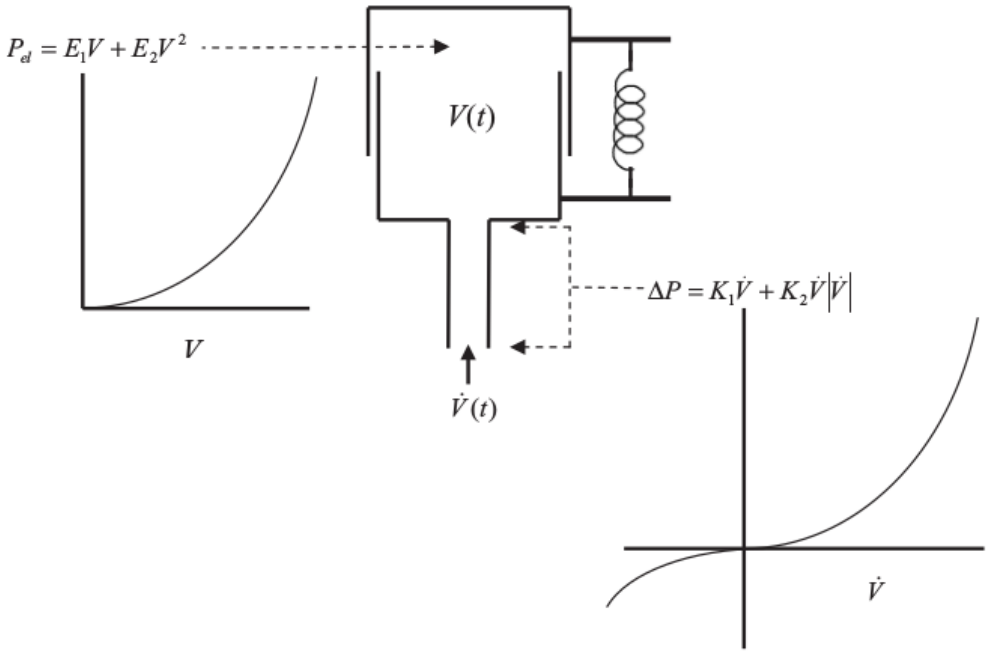

Figure 1-9.: Nonlinear single-compartment model of the lung. Taken from Bates [6]

represent in a more complete way the flows in airways, retaining the resistive and capacitive inputs derived from the system. The compliance for a single pipe, as discussed by Olufsen [82], can be described as a relation between the radius, elastance and wall thickness. This analogy shows how the mechanical properties of the wall influence the distensibility during the act of breathing. Thus, it is possible to analyze the effect of pressure on the walls of the airways and lungs in the respiratory system during the breathing process.

A large number of studies have adopted the impedance model in blood flows developed by Olufsen [82] to interpret lung behavior. In fact, some investigations such as those carried out by Ismail et al. [48],Roth et al. [93], Roth et al. [94] and Yoshihara et al. [125] present very complete models of the respiratory system, adopting 0d, 1D and 3D models, as the model shown in Figure **1-10**

This methodology consists of the development of the governing equations in a 3D model for the first generations of a bronchial tree. For the boundary conditions, a series of 1D models are applied based on the simplifications described by Bates [6] , and defining parameters such as resistance from 0d models as discussed by Pedley et al. [86]. In addition, to extend the model beyond the driving zone, Ismail et al. [48] characterizes the behavior of the acinar zone from 1D models that represent the alveoli as an interconnected mechanical spring-damper system.

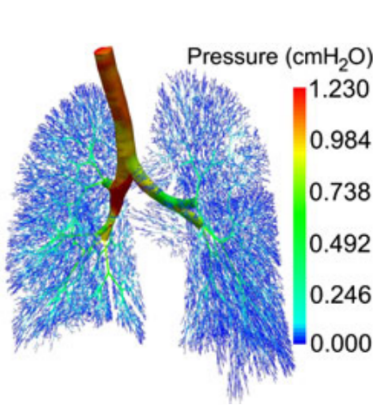

(a) 3d to 0d Representation

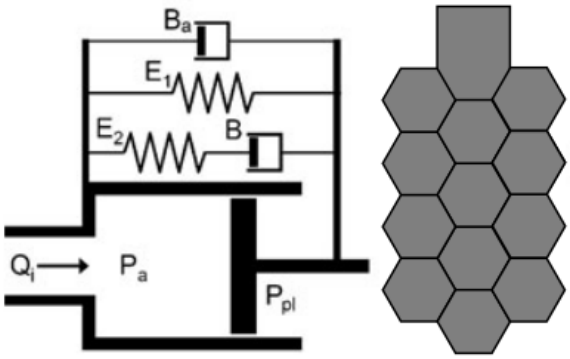

(b) Electromechanical analogy of an alveolar duct

Figure 1-10.: Parts of the hybrid airway model. Taken from Ismail et al. [48]

These study illustrates the capability of coupled models, using 3d to 0d reduced dimensional models, to analyze the system at different scales.

➪ Temporal coupling techniques

There are physical phenomena that occur at different time scales, i.e., while one part of the phenomenon is taking place at a time T, another part of it is occurring at a different time t. As described by Lockerby et al. [64], in the numerical simulation of these phenomena it is possible to perform time scale separations: macro processes are analyzed with a time step ΔT and micro processes with a Δt scale. In fact, Lockerby et al. [64] develops a series of possible coupling algorithms. In this algorithms some fields are calculated on the macro time scale and sent as input to the micro time scale, which calculates another field and sends the information back to the macro. Biological flows are phenomena that present these scale variations. While some phenomena such as the transport of blood is developed on the macro scale, phenomena such as the movement of platelets are developed on small time scales. For this case, Zhang et al. [127] develops a multiple time stepping algorithm which uses a nanostructural integrator to couple these phenomena that happen in nano seconds (platelets) and in micro seconds (fluid blood). Along the same lines, the phenomena developed in the airways also present variability in time scales. The transport of airflow in the upper airways takes a different time scale than the transport in the acinar zone. The multiscale airway analysis implemented by Fan et al. [31] shows a complete development of spatial and temporal scales variations. For temporal scale, the continuous micro solution-intermittent coupling (CI) method developed by Lockerby et al. [64] was employed. In this method, as seen in the Figure **1-11**, a separation of the scales is given using a ΔT time step for the macro space, and a smaller Δt time step for the micro space.

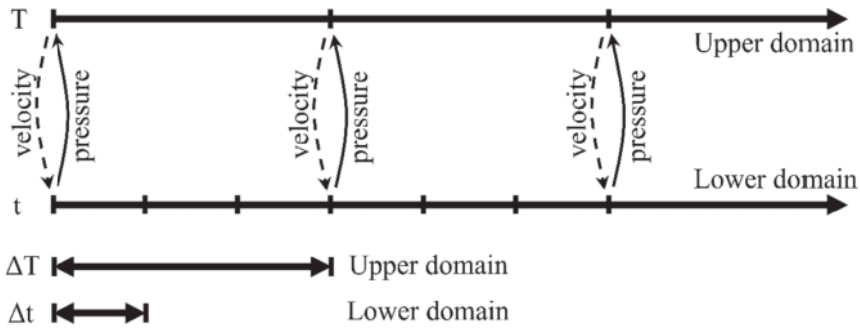

Figure 1-11.: Continuous micro solution-intermittent coupling (CI) method. Taken from Fan et al. [31]

The time steps are related by an integer value η, being Δt a scaled value $\eta \Delta T$. The velocity is calculated in macro space and sends this information to micro space, where the pressure is calculated and returned to macro space.

➪ **Coupled algorithms**

One of the most widely used hybrid simulation methods is the combination of algorithms for the solution of a multiphysics problem. This methodologies represents the possibility of solving problems associated with complex fluid phenomena involving different scales, fluid phases, etc. Techniques such as the discrete element method (DEM) and Smoothed-particle hydrodynamics (SPH) are combined with CFD for the analysis of particulate fluids. These methods can be described as

- ◇ *Discrete element method (DEM)*, as described by Blais et al. [12], is a technique that focuses on analyzing the behavior of particles from a Lagrangian conception, specifically granular material and fine powders.
- ◇ *Smoothed-particle hydrodynamics (SPH)* is a method based directly on the particle. As defined by Monaghan [75], the method consists of replacing the fluid medium by particles, in order to arrive at an approximation of the solution of the governing equations. As stated by Monaghan [74], the main characteristic of this technique is that it does not require a computational grid.

Phenomena such as fluidized granular systems (Jajcevic et al. [49], Fries et al. [37]), analysis of the lubrication process (Campos et al. [16], Paggi et al. [85]) and even in biomedical applications such as particle transport through blood (Vasquez Giuliano et al. [113], Nair et al. [78],Shahriari and Garcia [100]) can be analized from the application of these techniques. As expected, at the level of airway simulations these methods represent a powerful tool, given the number of particle transport phenomena

that occur in the breathing process, either by dispersion of pollutants, drug delivery and so on. The research work carried out by Chen et al. [21], Feng and Kleinstreuer [32] and WANG [115] shows how the transport and deposition of particles in the airways can be studied by interrelating CFD techniques to solve the continuous phase, i.e. fluid motion, with DEM for the dispersed phase, solving not only the phases independently, but also showing the effect of the interaction between phases. Figure **1-12** shows how the particle dispersion occurs when crossing the points of bifurcation of the tracks at different time instants (results obtained by Chen et al. [21] by DEM and CFD coupling).

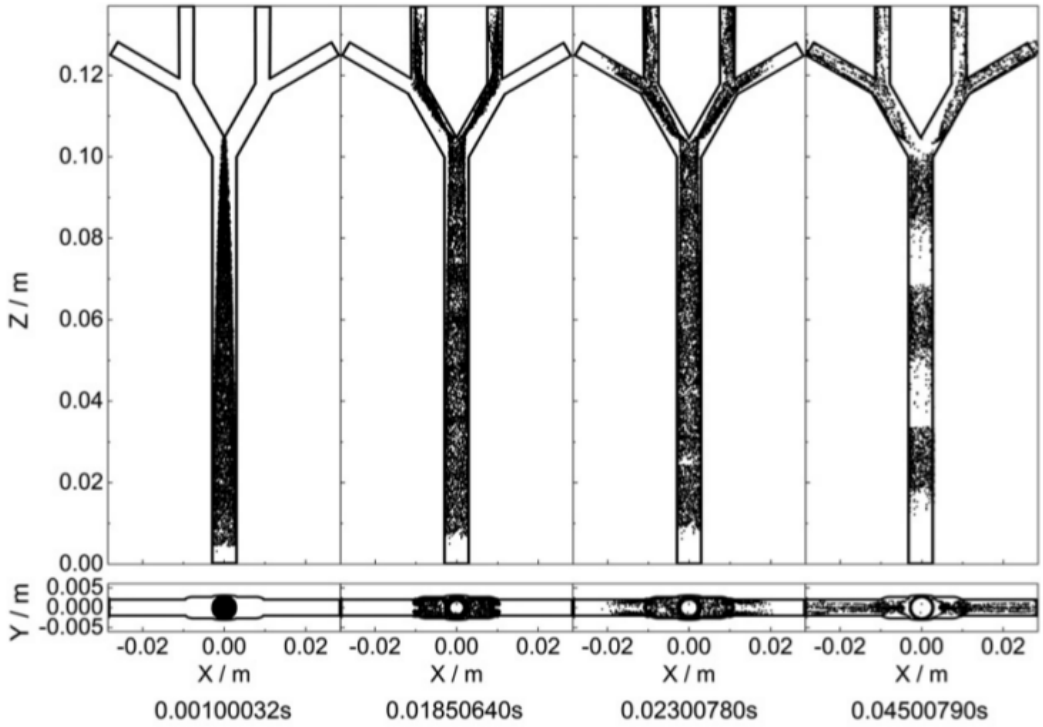

Figure 1-12.: Particle dispersation in airways single model. Taken from Chen et al. [21]

As well as particle and pollutant dispersion studies, , another matter of interest focuses on the study and development of respiratory inhalers. As discussed in the research carried out by Ruzycki et al. [95], the importance of the application of CFD techniques for the design of drug inhalation devices has been extending over time, with a particular focus on these coupled methodologies that allow the study of these multiphysics phenomena. An example of this is the research carried out by Ponzini et al. [92], in which he studied the development of dry powder inhalers from a coupled CFD-DEM algorithm. As can be seen in the Figure **1-13**, the fields associated with the fluid were developed on one side (CFD), and the results were subsequently coupled to analyze their influence on the particulate medium (DEM).

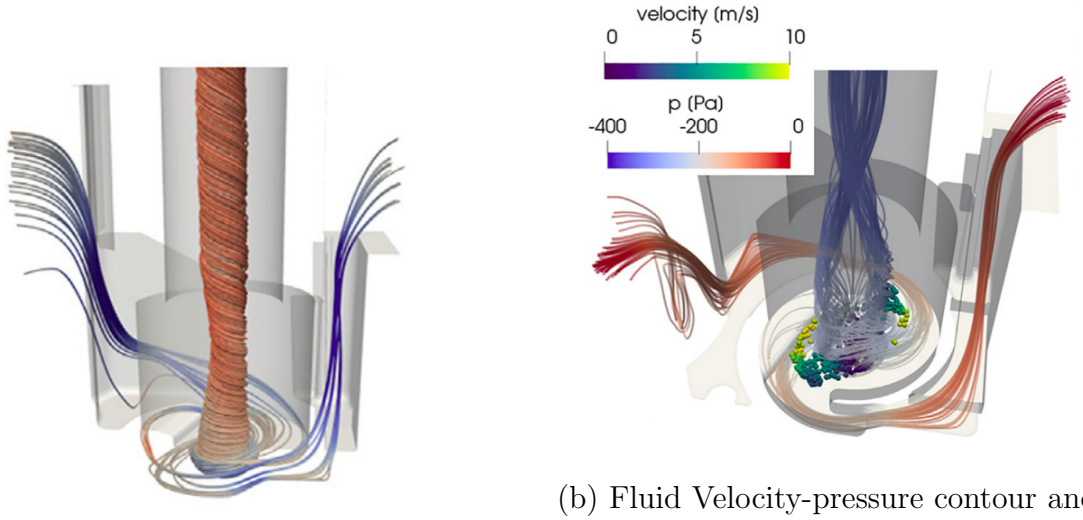

(a) Velocity streamlines for CFD simulation

(b) Fluid Velocity-pressure contour and particle

Figure 1-13.: CFD vs Hybrid CFD+DEM simulation. Taken from Ponzini et al. [92]

Within the investigations associated with airways, particular attention has been focused on the influence of the wall mechanics behaviour on the flow. The airway wall, as shown in the review work by Kamm [52], is a complex network of tissues, mucous membranes and layers with different biological properties. As discussed in the comparative work carried out by Green [40], the consideration of the mechanical properties of the wall, particularly its elasticity, has an impact on the flow development, especially in the accumulation of wall shear stresses which increase considerably if a stiff wall is considered. In fact, the investigation carried out by Xia et al. [123] illustrates that, as shown in Figure **1-14**, the shear stresses at the bifurcation decrease by up to five times when wall deformation is considered.

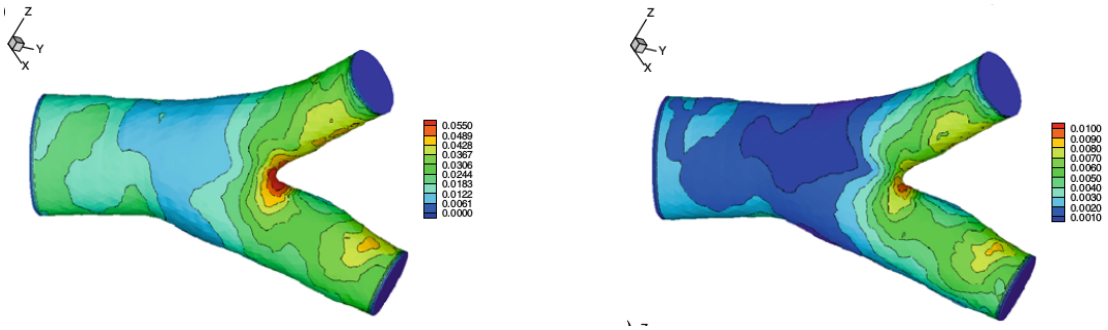

(a) Rigid Wall

(b) Flexible Wall

Figure 1-14.: Comparison between rigid and flexible walls. Taken from Xia et al. [123]

Fluid-structure interaction techniques are applied in order to understand these fluid and mechanical coupled behaviors. Many studies such as those conducted by Shukla

et al. [104], Mehra [71] and [18] show coupling approaches between CFD tools for the analysis of the flow development and a complement with finite element analysis (FEM) for the mechanical interaction. As discused by Sidhaye et al. [105] and Dailey et al. [28], the low levels of the deformation of the epithelial cells are associated with a decreases of the wall shear stresses on the wall, which demonstrates the importance of going into deformation analysis for mechanobiological purposes.

2. Airways fluids dynamics

2.1. Mathematical model

2.1.1. Governing fluid equations

The physical behavior of any fluid can be described from the Navier-Stokes equations:

$$\frac{\partial \rho}{\partial t} + \nabla \cdot (\rho \vec{\mathrm{v}}) = 0 \tag{2-1}$$

$$\rho \frac{\partial \vec{\mathrm{v}}}{\partial t} + \rho(\vec{\mathrm{v}} \cdot \nabla)\vec{\mathrm{v}} = -\nabla p + \rho \vec{g} + \nabla \cdot \tau_{ij} \tag{2-2}$$

$$\rho \frac{\partial E}{\partial t} + \rho \nabla \cdot (\vec{\mathrm{v}} E) = \nabla \cdot (k \nabla T) + \rho \vec{g} + \nabla \cdot (\bar{\bar{\sigma}} \cdot \vec{\mathrm{v}}) + \dot{W}_f + \dot{q_H} \tag{2-3}$$

Equations 2-1, 2-2 and 2-3 include conservation of mass, momentum and energy, respectively. The application of these equations depends on the type and conditions of the flow to be analyzed.

Under normal breathing conditions the working fluid is air. The air is a Newtonian fluid since the shear stress is related to the rate of shearing strain by the linear expression

$$\tau = \mu \dot{\gamma} \tag{2-4}$$

where τ is the shear stress, $\dot{\gamma}$ is the rate of shearing strain and μ the constant absolute viscosity. The kinematic and absolute viscosity are related by the equation

$$\nu = \frac{\mu}{\rho} \tag{2-5}$$

where ν is the kinematic viscosity and ρ the density. For the breathing regimes described above, the flow rates achieved are low. Under this condition the fluid density will remain constant, so it can be considered as incompressible flow. Also, temperature changes are not significant, so the flow is considered isothermal.

Knowing the conditions and particularities of the flow, we proceed to simplify the governing equations. From Eq. 2-1, i.e. conservation of mass, the density of the fluid is constant, so that the divergence of the velocity is zero:

$$\nabla \cdot \vec{\mathrm{v}} = 0 \tag{2-6}$$

where $\vec{v}$ is the the velocity vector field.
For conservation of momentum, Eq. 2-1, the stress tensor τ can be obtained from Eq. 2-4 (Newtonian flow). Furthermore, taking into account the zero velocity divergence and that the effect of gravity is not considered, the following expression is obtained:

$$\rho\frac{\partial\vec{v}}{\partial t} + \rho(\vec{v}\cdot\nabla)\vec{v} = -\nabla p + \mu\nabla^2\vec{v} \tag{2-7}$$

where $\vec{v}$ is the velocity vector field and p the pressure.
Due to the consideration of isothermal flow, the equation for energy conservation is neglected.

2.1.2. Dimensionless parameters

There are two dimensionless parameters which allow to determine and characterize the dynamics of air flowing through the airways: The Reynolds number and the Womersley Number, which are detailed below.

Reynolds number (Re)
As described by Fine [33], the Reynolds number (Re) is a dimensionless parameter that relates inertial forces to viscous forces. This number establishes the flow regime, which can be laminar, transitional or turbulent and can be described mathematically as

$$Re = \frac{\rho\, U_{ave}\, D}{\mu} \tag{2-8}$$

Where ρ is the fluid density, U_{ave} the mean velocity, D the characteristic length and μ the dynamic viscosity. In the case of circular cross-section pipes it has been established a that laminar flow occurs up to Re=2000, transitional regime between Re=2000 and Re=4000 and turbulent regime higher than Re=4000. The regime of human respiration under normal conditions, as discussed by Liu et al. [63], ranges from 0,27 - 2,16 l/s. This imply a Re number variation between 200 to 2600. Due to the morphology of the upper airways, the flow lines tend to become disordered and turbulent. However, as Fine [33] indicates, as the flow travels through the trachea and bronchi, the flow transitions from transitional to laminar, even reaching a stokes flow in the alveolar region.

Womersley number (Wo)
On the other hand, the Womersley Number Wo is a dimensionless parameter that, as Fine [33] explains, relates the transient forces to the viscous forces. Mathematically it is expressed as

$$Wo = \frac{D}{2}\sqrt{\frac{\omega}{\nu}} \tag{2-9}$$

Where ω is the frequency and ν the kinematic viscosity. This parameter is of special importance in pulsating flows since it allows to characterize the dynamics of the flow depending

on its oscillation frequency. As discussed by Gaddam and Santhanakrishnan [38], the normal breathing rate for an adult person ranges from 10 to 15 breaths per minute. For these ranges Wo numbers are obtained from between 2.41 to 2.95. As indicated by Bauer and Brücker [8], during mechanical ventilation this parameter can vary from 3 (in common mechanical ventilation as VACV) to 15 (in uncommon mechanical ventilation as HFOV).

2.2. Numerical methods

As indicated by Oro [84], the numerical simulations using CFD techniques have the structure shwon in Figure **2-1**.

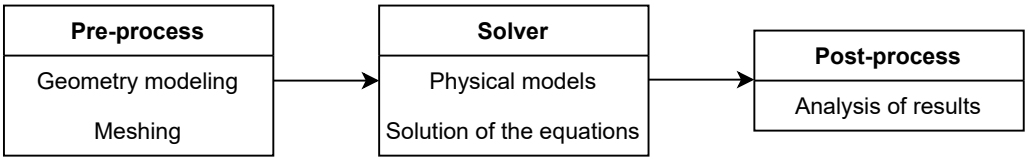

Figure 2-1.: CFD structure process

Each of the steps in the numerical simulation framework applied in this thesis work is specified below.

2.2.1. Pre-processing

The preprocessing within the numerical simulation involves the preparation and adaptation of the computational domain, from the geometry conception to the mesh generation process. For the numerical study of airways in the conduction zone (i.e. from generation 0 to 16 in the weibel model), two types of geometries are usually applied: *synthetic models* and *real patient-specific models*.
The definition and preparation of each of the geometries implemented in this work (whether synthetic or real patient-specific) are described in each respective chapter.
In order to solve the governing equations using a numerical method, it is necessary to generate a computational mesh. These meshes can be of structured type (which present a specific and ordered coordinate system) and unstructured (they are constituted through not necessarily ordered directions).
In the development of this research work, unstructured meshes are used for all numerical simulations, due to the level of difficulty that would imply developing these geometries (especially those obtained from medical image segmentation) using structured meshes. For this purpose, the native unstructured mesher *snappyHexMesh*, implemented through the open source **OpenFOAM**, were selected. The number of cells used are specified in each

particular simulation case. This cell quantity is based on a mesh independence criterion, which ensures that the computational domain will not have a direct effect on the numerical results obtained.

2.2.2. Solver

The process of numerical solution of the physical phenomenon is summarized in the solution of the governing equations. The finite volume method (FVM) was selected and applied in the development of this work. Considering a control volume VC and a specific variable ϕ. As described by Oro [84], it is possible to express the time variation of ϕ through VC from a conservation principle

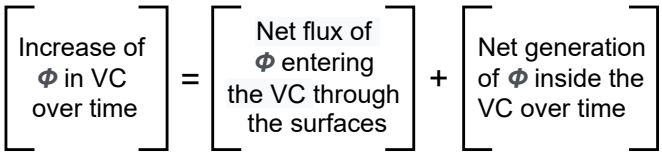

This general equation of conservation can be represented in terms of divergences (i.e., in conservative form) as

$$\frac{\partial(\rho\phi)}{\partial t} + \nabla \cdot (\rho\vec{v}\phi) = \nabla \cdot (\Gamma\nabla\phi) + S_\phi \tag{2-10}$$

Each of the terms in Eq. 2-10 describes:

- ◇ The temporal component (first term), i.e. the accumulation or decrease of ϕ in the VC over time.
- ◇ The convective component (second term), which represents the transport of the variable through the flow velocity.
- ◇ The diffusive component (third Term), which corresponds to the transport phenomena occurring at the molecular level
- ◇ The source (last term), to take into account sources of generation or destruction of the transported variable.

The finite volume method is developed from the integration of Eq. 2-10 on a three-dimensional control volume V:

$$\int_V \frac{\partial(\rho\phi)}{\partial t}\, dV + \int_V \nabla \cdot (\rho\vec{v}\phi)\, dV = \int_V \nabla \cdot (\Gamma\nabla\phi)\, dV + \int_V S_\phi\, dV \tag{2-11}$$

Applying the Gauss theorem of divergence in Eq. 2-11 A we will have:

$$\frac{\partial}{\partial t}\int_V \rho\phi \; dV + \int_S (\rho\vec{v}\phi)\cdot d\vec{A} = \int_S (\Gamma\nabla\phi)\cdot d\vec{A} + \int_V S_\phi \; dV \tag{2-12}$$

If we consider non-steady-state phenomena, i.e., with time variations, the expression of Eq. 2-12 requires integration with respect to t:

$$\int_{\Delta t}\frac{\partial}{\partial t}\left(\int_V \rho\phi \; dV\right) dt + \int_{\Delta t}\int_S (\rho\vec{v}\phi)\cdot d\vec{A} \; dt = \int_{\Delta t}\int_S (\Gamma\nabla\phi)\cdot d\vec{A} \; dt + \int_{\Delta t}\int_V S_\phi \; dV \; dt \tag{2-13}$$

The FVM applies the conservation law in integral form (i.e., the development shown in equations 2-12 and 2-13) on each of the physical cells that are developed from the discretization of the computational domain (already briefly explained in the preprocessing item). This procedure leads to a matrix system that describes the physical phenomenon. In order to analysis the temporal progress, the following schemes are implemented for time discretization:

- **Explicit:** flows and source terms are evaluated from the previous time step information. It has the advantage that the resulting matrix system is solved in a simple way, without the need to calculate the inverse of the matrix, reducing the computational cost. However, this algorithm usually presents numerical stability problems.

- **Implicit:** flows and source terms are evaluated from the current step information. It has the disadvantage that the resulting matrix system requires the calculation of the inverse of the matrix, increasing the computational cost with respect to the explicit scheme. However, the numerical stability of this scheme is unconditional.

- **Crank-Nicholson:** flows and source terms are evaluated from past and current information combined with a factor of 1/2. This method, like the implicit method, is unconditionally stable.

For the application of the FVM the open source software **OpenFOAM (OF)** was selected. This software offers a number of the so-called solvers, which are developed with the necessary conditions to solve the different physical phenomena available. Taking into account the behavior of the phenomenon being analyzed as well as the governing equations described in the previous item, a solver for transient, incompressible and isothermal flow is required. The OF library offers the following solvers for this type of flows:

- *icoFoam*: it is essentially designed for laminar flows using the PISO algorithm for the Pressure-velocity coupling

- *pimpleFoam*: it is a large time-step transient solver that allows the study of both laminar and turbulent flows, using a coupling between the PISO and SIMPLE algorithms.

As indicated by Behrens [10], for the calculation and solution of pressure and velocity OF provides a number of linear solvers, such as *Geometric agglomerated algebraic multigrid solver (GAMG)*, *Diagonal incomplete LU preconditioned BiCG solver (BICCG)*, and the *smoothSolver*, among others, *GAMG* being one of the most widely used. This algorithm starts with the computation of a fast solution using coarse meshes, and takes these results as a starting point for the computation of finer meshes.

Preferred numerical configuration
Unless otherwise indicated, the unsteady, incompressible, laminar solver flow icoFoam was selected. Pressure-velocity coupling was accomplished by using the PISO algorithm. Temporal integration was performed by using a *backward* scheme and the spatial discretization is solved using second-order interpolation schemes for the gradient and divergence terms. The *Geometric Agglomerated Algebraic Multigrid Solver (GAMG)* was used to solve the Poisson-pressure equations, whereas the velocity field was obtained using the *smoothSolver* scheme available in OF.

2.2.3. Post-processing

The post-processing of the numerical simulation consists of reporting and analysis of the results obtained. Within airway fluid dynamics, the basic focus of study is on the behavior of velocity, pressure, secondary flows and wall shear stresses. Throughout this document, some particular terms were used to indicate a specific zone or points were the results were measured. These terms are illustrated in Figure **2-2**.
The anatomical planes define the body sections through the three main axes: **coronal plane** (delimits the body in frontal and posterior zones), **sagittal plane** (delimits in right and left zones) and **transverse plane** (delimits in proximal and distal zones). Branches have a relatively cylindrical geometry (particularly in synthetic models), therefore it is possible to establish an axial axis, which describes the trajectory of each branch, i.e. its length and direction. Some fields such as secondary flow patterns are taken in cross sections. As indicated in the Figure **2-2**, these will be mainly measured at 20 % and 50 % of the branch length. The red dots indicate bifurcation points, which have particular attention given their impact on properties such as wall shear stresses.
Another review point is the inner branch walls (the yellow line in the Figure), taken on the coronal plane, which goes from the bifurcation point to the crossing point of the axial axis lines of the branches. The variations of the wall shear stresses are the main results analyzed on this section.
Taking into account the zones described above, two types of results reporting are used in this work:

1. Curve plots: these figures present the behavior of variables over some length or time. They were made using the open access software Gnuplot.

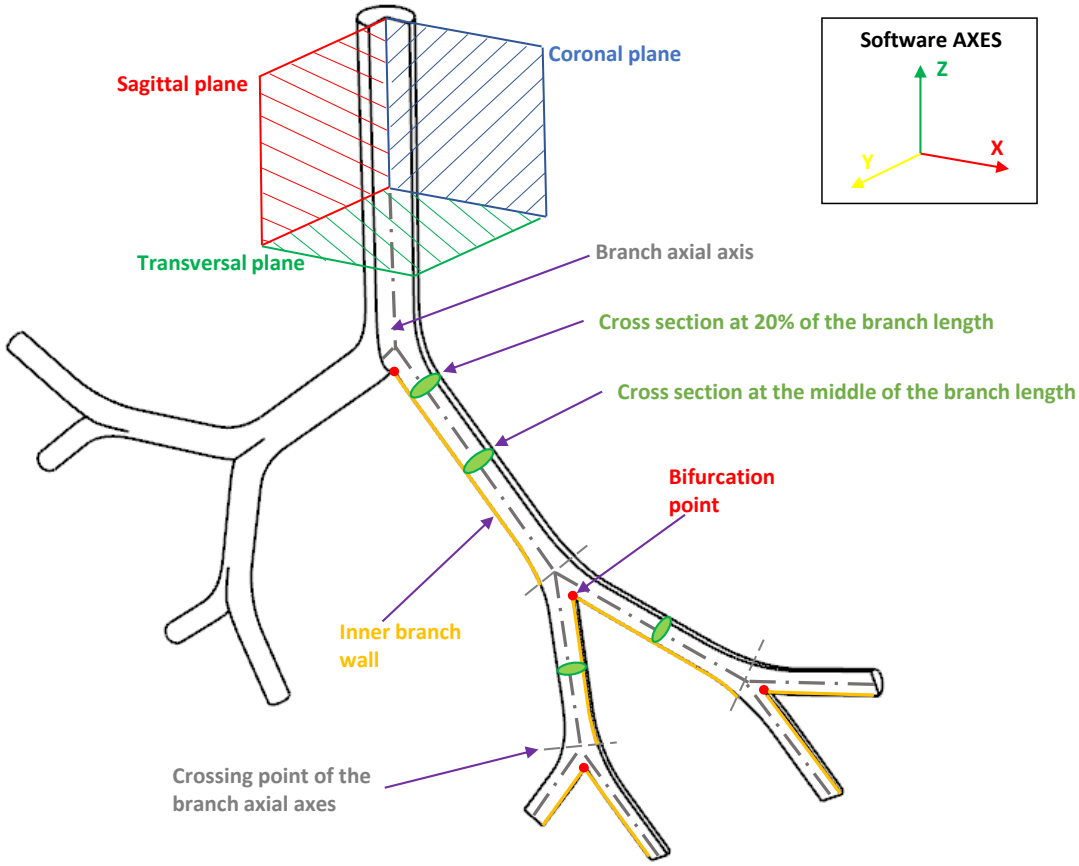

Figure 2-2.: Indicative scheme of the zones and points where the results are reported

2. Distribution plots: These figures present the behavior of the variables over the computational domain. They were performed using the open access software Paraview.

3. Spatial complexity reduction

As described in previous chapters, in numerical studies of the human airways, two types of geometrical models are usually used: real specific patient models and synthetic geometries. Patient-specific models are obtained from the segmentation of medical images from computed tomography (CT) scans. On the other hand, Synthetic models describe airways as pipes of known cross-section and length. The most commonly used models are those developed by Weibel et al. [117] and by Horsfield et al. [46]. Synthetic models are considered as a geometrical simplification of the real airways, as they reduce the complexity intrinsic to the morphology of the branches. The consideration of smooth walls, without rings or perturbations, as well as branches without cross-sectional changes, facilitate both the modeling of the geometry and the respective discretization and solutions of the equations through the numerical model. In this chapter, a comparison study between the effects of using real patient-specific models vs. the simplification obtained with synthetic airway models is developed. In addition, an analysis of the effects of varying some morphological parameters (such as bifurcation angle and carina rounding radius) is performed.

3.1. Real vs Synthetic airways models

In order to compare the effect of using synthetic vs. real models on flow development, a series of CFD numerical simulations were carried out for a synthetic geometry based on the model described by Weibel et al. [117] and a real patient-specific geometry obtained from a CT scan. These simulations cover two Re numbers within the laminar zone.

3.1.1. Specific-patient airways model

A real specific airways model was segmented and processed from of a computed axial tomography scan (TC) belonging to a healthy 40-year-old male patient. The procedure is detailed as follows:

- **STEP 1.** The 3D model reconstruction was developing using the open source *3D Slicer*. A segmentation process was carried out using an extension for airways analysis implemented by Nardelli et al. [79]. The three morphological human planes (sagittal, coronal and transversal) in DICOM images format were required to develop this process, as shown in Figure **3-1** (a).

- **STEP 2.** A cutting process was performed using the commercial software *Rhinoceros 5.0*, as shown in Figure **3-1** (b). Hereby, the geometry was trimmed to encompass a total of five generations from the trachea, passing to main and secondary bronchus. During this process a straight cut was also made in the trachea to had a flat inlet.

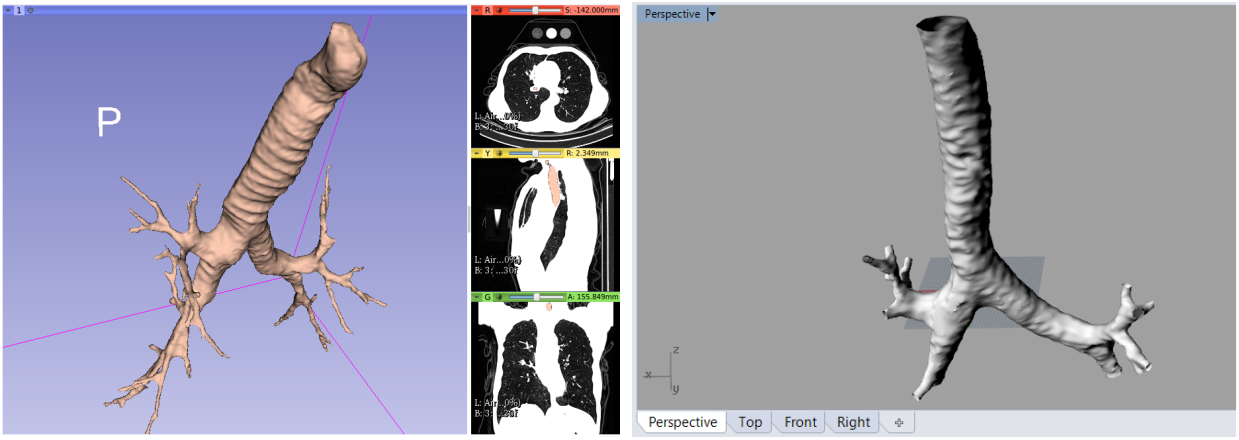

(a) Step 1. *3d Slicer* (b) Step 2. *Rhinoceros 5.0*

Figure 3-1.: Step 1 and 2 in the specific-patient airways model generation

- **STEP 3.** Using the open source *Blender*, we proceed to close the open surfaces, i.e. all the cuts made in STEP 2 (as illustrated in the Figure **3-2** (c)). In addition, an artificially length was added to the latest generation to avoid problems associated with the development of the flow and the outlet boundary conditions.

- **STEP 4.** Finally, as shown in the Figure **3-2** (d), a process of smoothing and closing of open surfaces was performed using the open source *MeshLab*. In this step the final check of the geometry was performed. With the Laplacian smoothing process the surface quality was improved in areas where there are many irregularities. At the same time, a final check of open surfaces allowed us to confirm that there were no openings and empty spaces. These procedures are fundamental to avoid future problems in the generation of the computational domain/meshes.

3.1.2. Synthetic human airways models

The synthetic geometry cover the first five generations of the model described by Weibel et al. [117]. As can be seen in Figure **3-3** (a), these generation represent the trachea, main bronchus and bronchioles. TThe model was *in plane*, i.e., all the geometry was contained within the coronal plane. Subcarinal angle was taken as 120^o, being one of the highest values reported in studies such as those carried out by Khade et al. [54] and Christou et al. [24]. With this angle, we ensure the modeling of several generations before reaching the inevitable clash between branches generated in the *in plane* models. The measurements of each generation

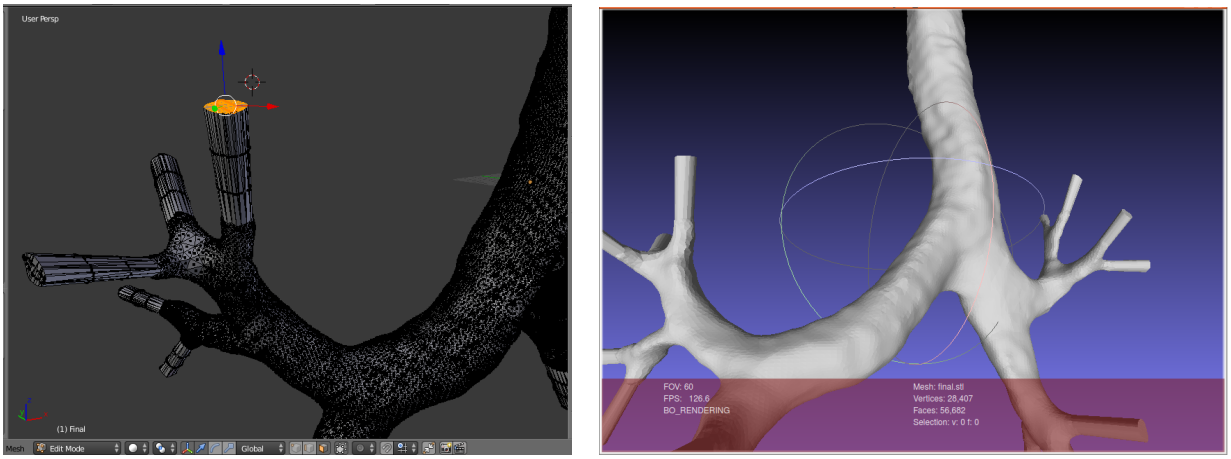

(a) Step 3. *Blender* (b) Step 4. *MeshLab*

Figure 3-2.: Step 3 and 4 in the specific-patient airways model generation

can be seen in Table **3-1**, being D, L and BA the branch diameter, length and bifurcation angle, respectively. The length of the last generation was adjusted to 5 times the diameter.

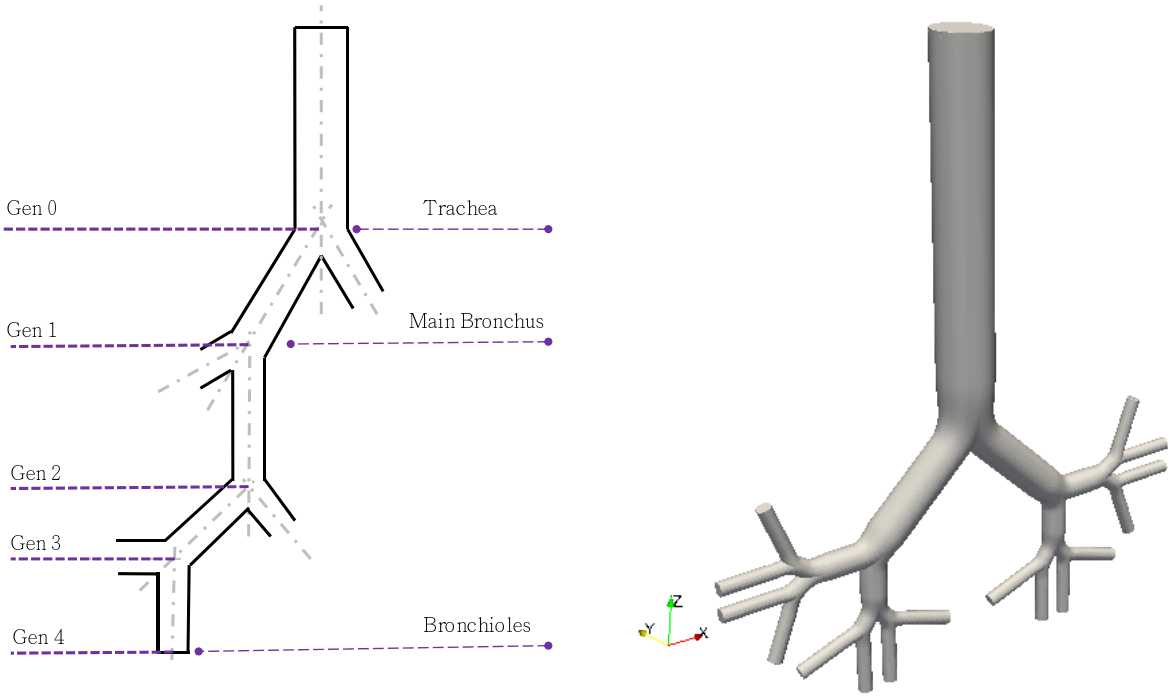

(a) Weibel's model generations (b) 3D Synthetic model

Figure 3-3.: Models comparison

GENERATION	D (mm)	L (mm)	BA (^{o})
0	18	120	0
1	12.2	47.6	120
2	8.3	19	70
3	5.6	7.6	50
4	4.5	22.5	70

Table 3-1.: 5 Generation Model parameters

3.1.3. Numerical method

For this study, the working fluid is air. The governing equations are described in Eqs. 2-6 and 2-7. For the simulation with the synthetic model, preferred numerical configuration described in section 2.2.2 was selected. For the case of the simulation with the real patient-specific model, the same configuration was chosen, with the only difference that the *pimpleFoam* solver was applied. The average number of tetrahedral cells was 3e6 for synthetic model and 4e6 for real model. For this comparative study, for both geometries only inhalation human process was analyzed. An uniform velocity profile at the inlet (i.e. trachea) was adopted, covering Re 500 and Re 2000. At the outlets an uniform pressure boundary condition was implemented. No-slip boundary condition for the wall was applied.

3.1.4. Comparative numerical results between real and synthetic models

The comparative results between the use of synthetic and real patient-specific airway models are shown below. The main emphasis was placed on the pressure and shear stress distributions on the wall, as well as on the velocity streamlines. It is important to highlight two aspects of these results:

- In all graphs, to improve the visual comparison, the color scales for the real vias were adjusted to the maximum and minimum values of the synthetic vias. Thus, when the visual check is performed, the colors represent the same intervals.

- In Table **3-2** relative errors are presented as percentages. In all cases, such error was calculated as

$$e\ [\,\%] = \frac{|V_{synt} - V_{real}|}{V_{synt}}\ \text{x}\ 100 \tag{3-1}$$

  where V_{synt} is the value obtained from the synthetic model and V_{real} is the value obtained from the real specific patient model.

Figure 3-4 illustrates the streamlines velocity for both cases at Re 500. Given the geometrical symmetry of the synthetic model and the setting of the boundary conditions, the streamlines are distributed in a symmetrical way. For the real case, the lines present a less uniform behavior influenced by the disparity in the dimensions of each of the branches. The same effect is denoted for Re 2000. It is important to note that the maximum velocity is found in the branches of the last generations for both cases. A comparison of the maximum velocity values for both RE numbers can be seen in Table 3-2. The relative error (calculated with respect to the velocity of the synthetic model) shows that in spite of the geometrical differences, the velocity values are close to each other, presenting percentages no greater than 5 for both models of this study.

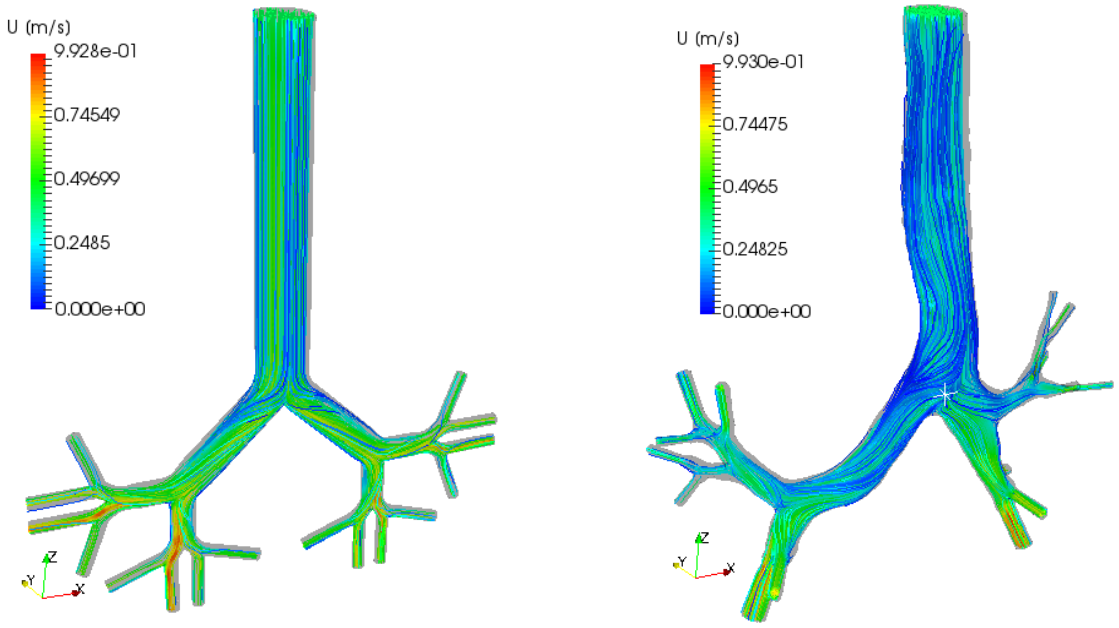

(a) Synthetic Geometry (b) Real patient-specific Geometry

Figure 3-4.: Velocity streamlines for Re=500

Comparison of wall pressure distributions for Re 2000 is shown in Figure 3-5. It is clear how for both cases a pressure maximum is located at the carina. The value of this maximum for both Re 500 and Re 2000 is given in the Table 3-2, with a total of 15 % and 25 % percentage error. The differences in branch dimensions, cross-sectional changes and asymmetry between the synthetic model and the real model have an impact on the increase in pressure drop. However, the distribution of pressures tends to be similar in the generations for both models, with values ranging from 4 $[Pa]$ to 6 $[Pa]$ for the main bronchi and oscillating values around 6 $[Pa]$ for the trachea.

Figure 3-6 presents the WSS comparison. As discussed in the study of bifurcation angle and carina rounding, the maximum WSS values are located near the bifurcation points. The synthetic model considers the joints without any smoothing, i.e., as straight joints. Therefo-

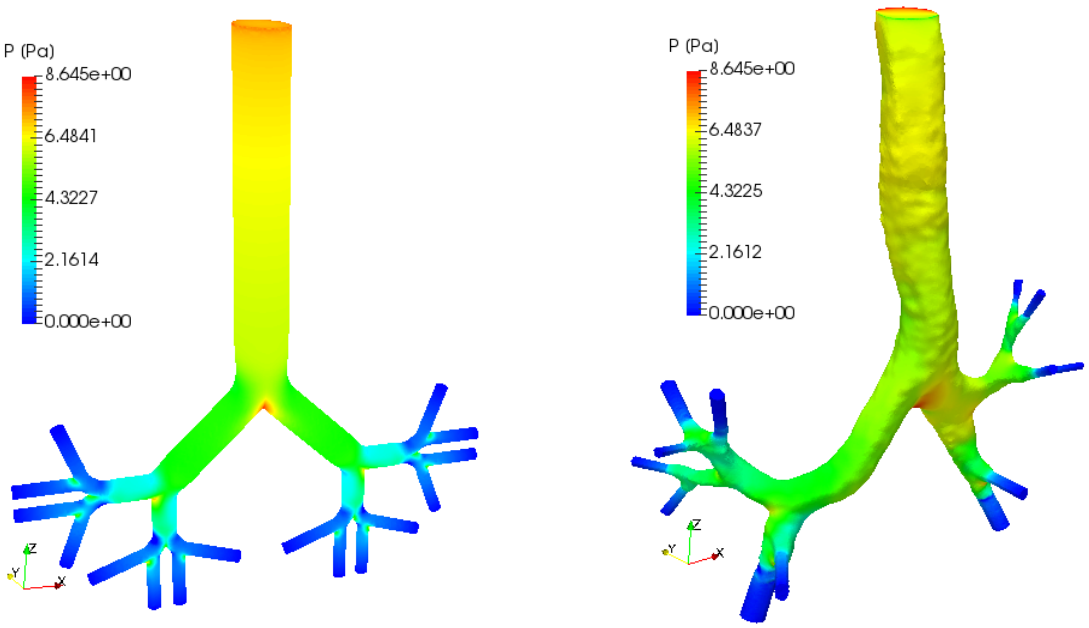

(a) Synthetic Geometry (b) Real patient-specific Geometry

Figure 3-5.: Wall pressure distribution for Re=2000

re, the synthetic geometry has larger WSS zones than the real model. It is enough to see the real carina to notice the smoothing differences. However, by analyzing the maximum values (see Table **3-2**), it can be seen how the largest WSS is generated in the real geometry. As illustrated in the **3-7** , this maximum is located in a surface perturbation. The investigation on airway walls mechanics performed by Kamm [52] shows how these walls are highly rough and vary depending on properties derived from the component layers. Thus, these perturbations may be inherent to the patient's airways or may be residues and failures of the segmentation process.

	Re 500			**Re 2000**		
	U max. $[m/s]$	**P max.** $[Pa]$	**WSS max.** $[Pa]$	**U max.** $[m/s]$	**P max.** $[Pa]$	**WSS max.** $[Pa]$
Synthetic Model	0.993	1.083	0.092	3.575	8.645	0.554
Pacient-specific Model	1.034	1.241	0.130	3.403	10.830	0.726
Relative error	4 %	14.5 %	41 %	4.8 %	25 %	31 %

Table 3-2.: Comparison of maximum values

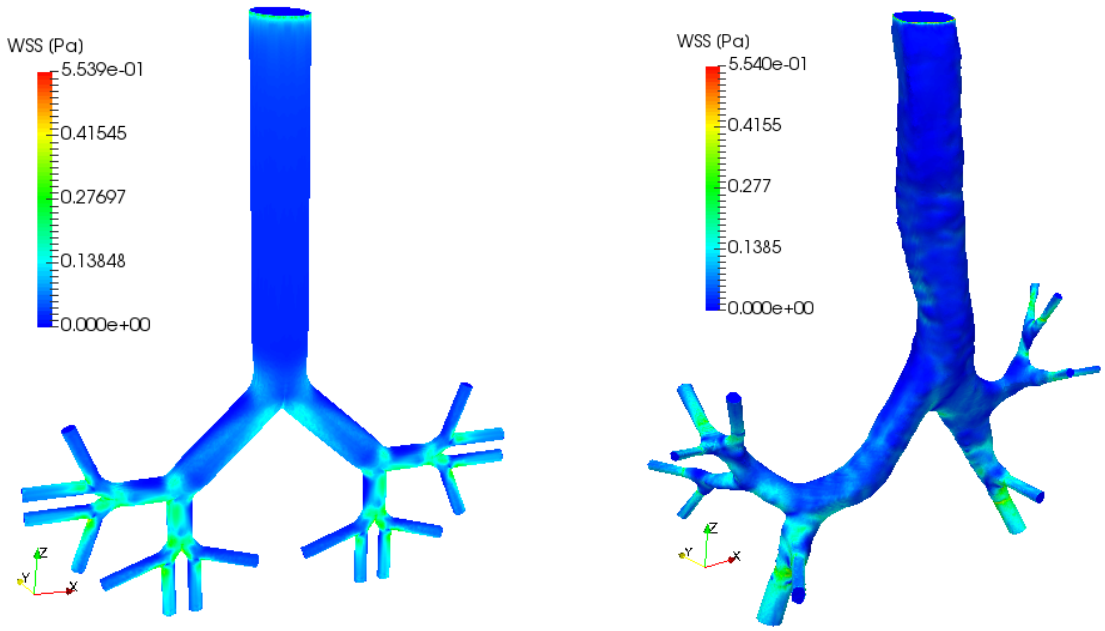

(a) Synthetic Geometry (b) Real patient-specific Geometry

Figure 3-6.: Wall shear stresses for Re=2000

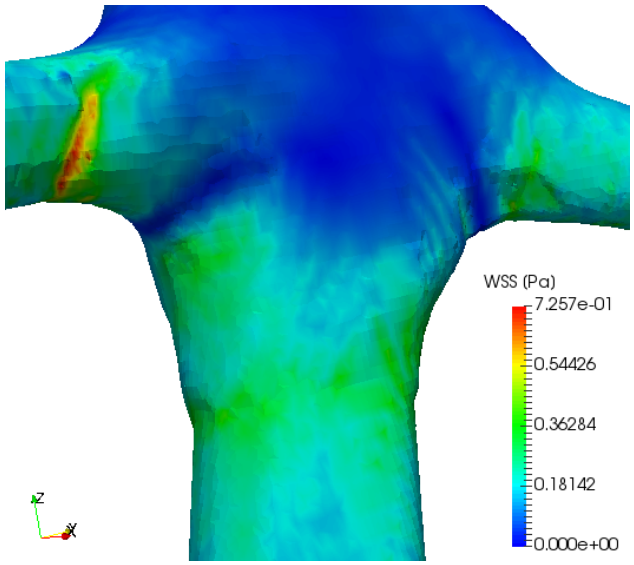

Figure 3-7.: Location of Maximun WSS for real model. Re 2000

3.2. Influence of morphological parameters on airway flow

3.2.1. Effect of branch bifurcation angle

Bifurcation Angle (BA) is a parameter closely related to the morphology of the lungs. Its numerical value depends on a number of factors such as thorax width (Haskin and Goodman [42]), gender and age (Alavi et al. [2]), as well as on the specific techniques and methodologies employed to measure it (Khade et al. [54]), being the most commonly used X-Ray, Computed Tomography and In vitro measurements in human corpses. Different angle measures are reported in literature. Haskin and Goodman [42] obtained a range of variation of the subcarinal angle between 55^o a 65^o, the work performed by Khade et al. [54] produced a range between 50^o to 130^o, and Christou et al. [24] obtained $65{,}04^o$ to $122{,}01^o$ for men and $69{,}46^o$ to $113{,}94^o$ for women. Moreover, the study carried out by Sahni et al. [96] in human fetuses showed values for this parameter ranging between 42^o a 75^o. Some research has linked this angle with some physical pathologies such as the slope or displacement of bronchus produced by pericardial fluid accumulation (Chen et al. [20]) and left atrial enlargement, influenced by the widening of the bifurcation angle (Lin et al. [62]; Murray et al. [76]).
Aiming to explore the effect of variations of the bifurcation angle (BA) of lower human airways on the respiratory processes, numerical simulations of airflow during inhalation and exhalation were performed using a synthetic bifurcation models. Geometries for the airways models were parameterized based on a set of different BA's. A range of Reynolds numbers (Re) relevant to the human breathing process were selected to analyzed the airflow behaviour.

- ◇ **Geometry**

  For the purposes of the this study, a computational synthetic airways model, including the first three generations of the human morphology, was developed using the parameters prescribed by Weibel et al. [117]. Those generations represent the trachea, main bronchus and secondary bronchus. In order to simplify the reading results, the notation for airways described by Christou et al. [24] was adopted. The geometric parameters are illustrated in Figure **3-8**, and the values specified in Table **3-3**. To avoid problems linked to the development of the flow near the outlets, the length of the last generation branches was extended to be at least five times the related outlet diameter.

AIRWAY	D (mm)	L (mm)
TRA	18	120
LMB / RMB	12	47.6
LUB / RUB / LLB / RIB	8.3	41.5

Table 3-3.: Weibel's model parameters in the first three generations

For the evaluation of the effect of the bifurcation angle (BA), six values were selected from within the range obtained experimentally by Haskin and Goodman [42] of phy-

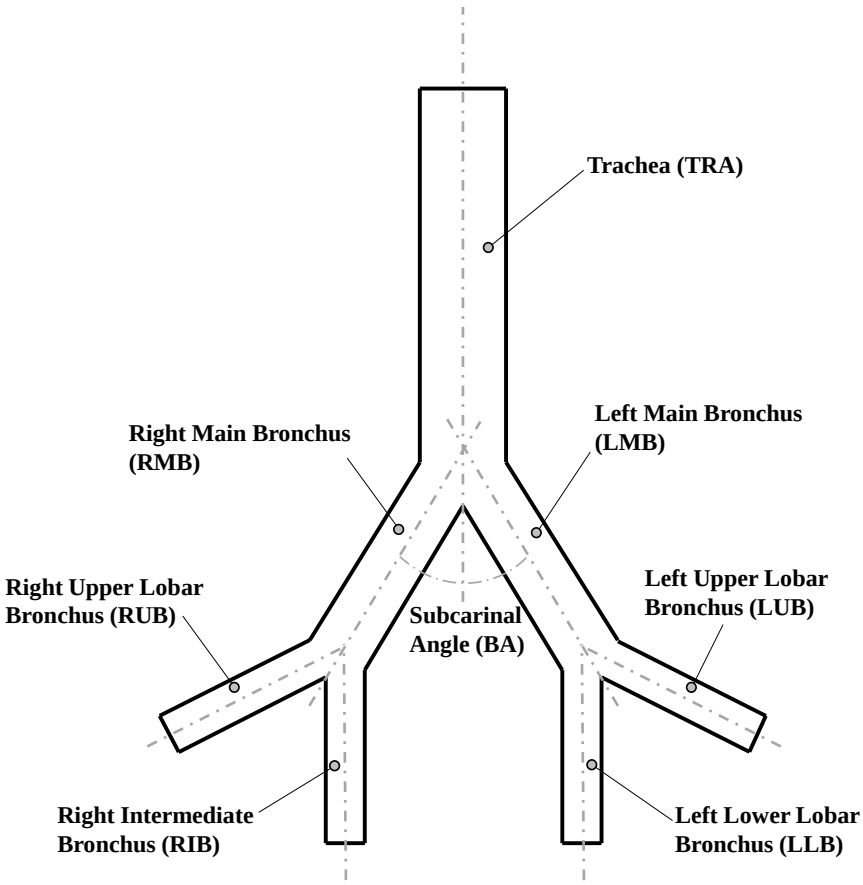

Figure 3-8.: Aiways tree with the notation described by Christou et al. [24]

siological relevant subcarinal angle values. The set of selected angles was prescribed for all generations in each model. In order to visualize further trends, an additional value for the BA of 70° was also explored, according to the mean angles with minimal resistance, as discussed by Horsfield and Cumming [45]. These values are shown in Table **3-4**.

◇ **Numerical Model**

For this study, the working fluid is air. The governing equations are described in Eqs. 2-6 and 2-7. The preferred numerical configuration described in section 2.2.2 was selected. The average number of tetrahedral cells was 1.5e6.

◇ **Boundary conditions**

As mentioned previously, the two main breathing processes were numerically simulated, i.e. exhalation and inhalation. For the simulations of the inhalation process, a uniform pressure boundary condition at the outlets was prescribed. As indicated by Bauer and Brücker [8], this consideration enables flow to adjust to different pressure gradients

AGE [YEARS]	MEAN ANGLE [BA °]
21 - 30	64.2
31 - 40	58.9
41 - 50	61.9
51 - 60	63.1
61 - +	55.9
All ages	60.8
Extra	70

Table 3-4.: Subcarinal angles obtained by Haskin and Goodman [42]

through the different airways generations. Yang et al. [124] shows that the inlet velocity profile (in inhalation) considerably affects the development of flow within the airway model, specially the mass flow distribution in the branches. In this study a symmetrical parabolic velocity profile at the inlet (i.e. trachea) was adopted. Human breathing rates oscillate between 0,2 L/s and 2,5 L/s (Martonen et al. [68]; Liu et al. [63]), equivalent to a range of Re numbers between 200 and 2800. Accordingly, a set of different Reynolds numbers between 500 and 2000 were selected for these studies.

The exhalation process simulations were setup using a uniform pressure condition at the outlet (trachea in this case) and, in order to ensure that the flow is fully developed before reaching the joint bifurcation, a parabolic velocity profile was prescribed at the inlets (secondary bronchus). This profile was defined to be symmetrical respect to the axial axis of the branches, and its maximum value is equal to the maximum velocity obtained in the outlets in each of the inhalation cases. A Dirichlet no-slip boundary condition was applied to the velocity field in all cases simulated.

◇ **Results**

Although a number of previous numerical experiments have shown that the presence of bifurcations in the human airways in fact alter the flow velocity profiles, the precise effect of the angle of such bifurcations has been somehow overlooked. As it will be shown in this work, one of the more important effects of varying the bifurcation angle (BA) is the skewing of the flow velocity profiles towards inner walls. To this end, mean velocity curves against branch diameter (D) were built, using a normalized length d/D.

Mean velocity profiles on the coronal plane for different angles are shown for $Re = 500$ and $Re = 2000$ in Figure **3-9**. It seems that there exist a displacement trend of the peak of velocity profiles towards the inner walls of the branches, as has been previously reported and described in other numerical and experimental investigations (Calay et al. [15]; Van Ertbruggen et al. [112]; Liu et al. [63]; Schroter and Sudlow [98]; Zhao and Lieber [128]). The BA has a strong influence on the profile deformation. By examining

the profiles measured at the middle of each ramification (LMB, LUB and LLB), a narrowing of the velocity profile can be appreciated, as well as a shifting of the peak from the outer to the inner walls. This relocation is in line with the peak displacement trend, a phenomenon that seems to be more pronounced for larger angles.

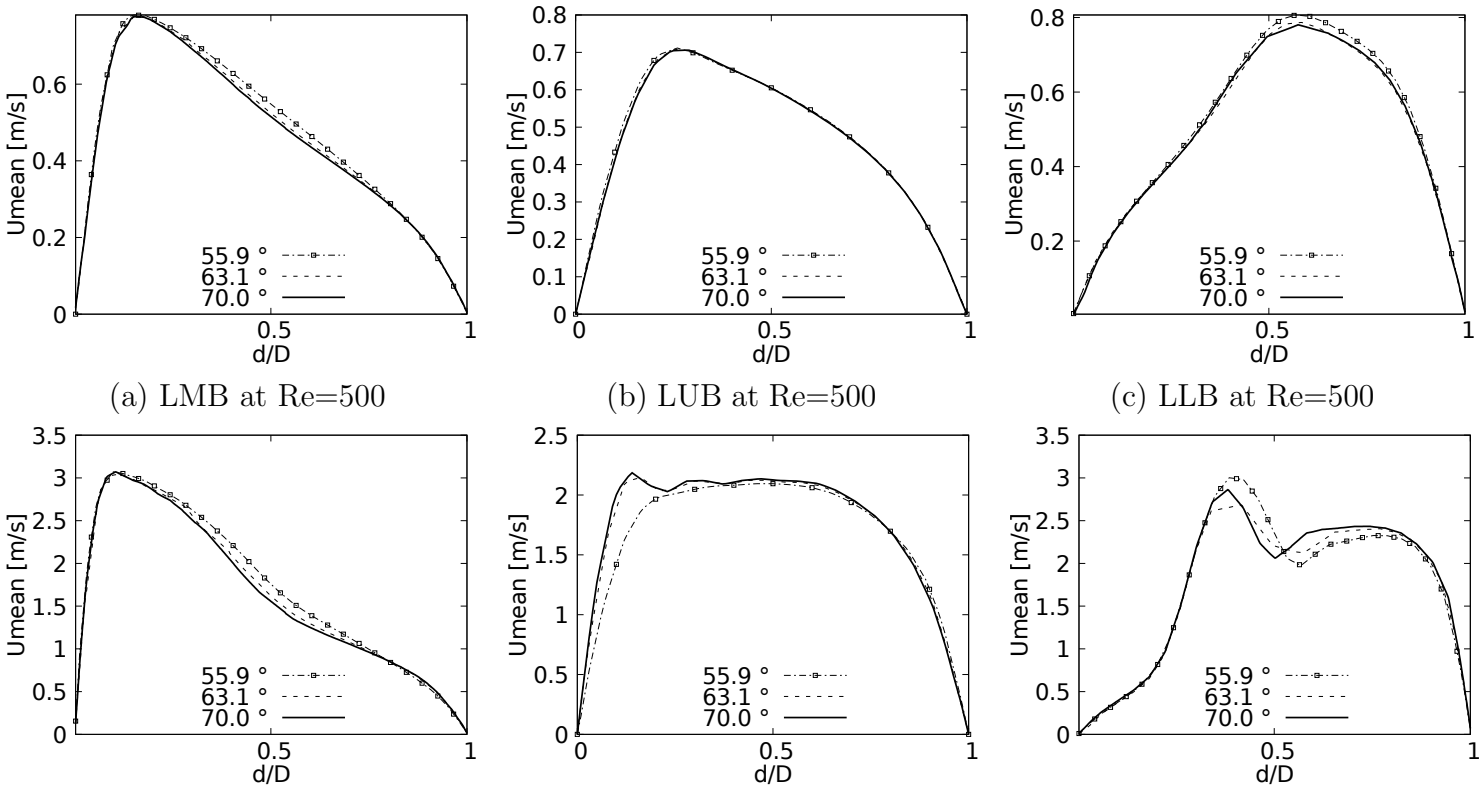

(a) LMB at Re=500 (b) LUB at Re=500 (c) LLB at Re=500

(d) LMB at Re=2000 (e) LUB at Re=2000 (f) LLB at Re=2000

Figure 3-9.: Velocity profiles on coronal plane

On the other hand, the velocity profiles taken on the sagittal plane are symmetric across the axial axis. This kind of behaviour has been described in various numerical and experimental works as these carreid out by Pedley et al. [88]; Liu et al. [63]; Schroter and Sudlow [98]. Results for different angles at Re=500 and Re=2000 are shown in Figure **3-10**. The characteristic "M"shape is clearly visible. This phenomenon was described by Schroter and Sudlow [98] and it illustrates how flow velocity increases near walls and decreases across the axial axis. The larger the value of the BA, the stronger is the effect mentioned above.

Results for the exhalation process show how the velocity profiles are symmetrical both in coronal and sagittal planes, as (Schroter and Sudlow [98]; Corieri [27]) has already shown in their studies. As seen in Figure **3-11**, velocity profiles taken in the middle of the trachea shown an acceleration in both sagittal and coronal plane, and a particular peak in the centre of the branch, considerably more pronounced at Figure **3-11** (d).

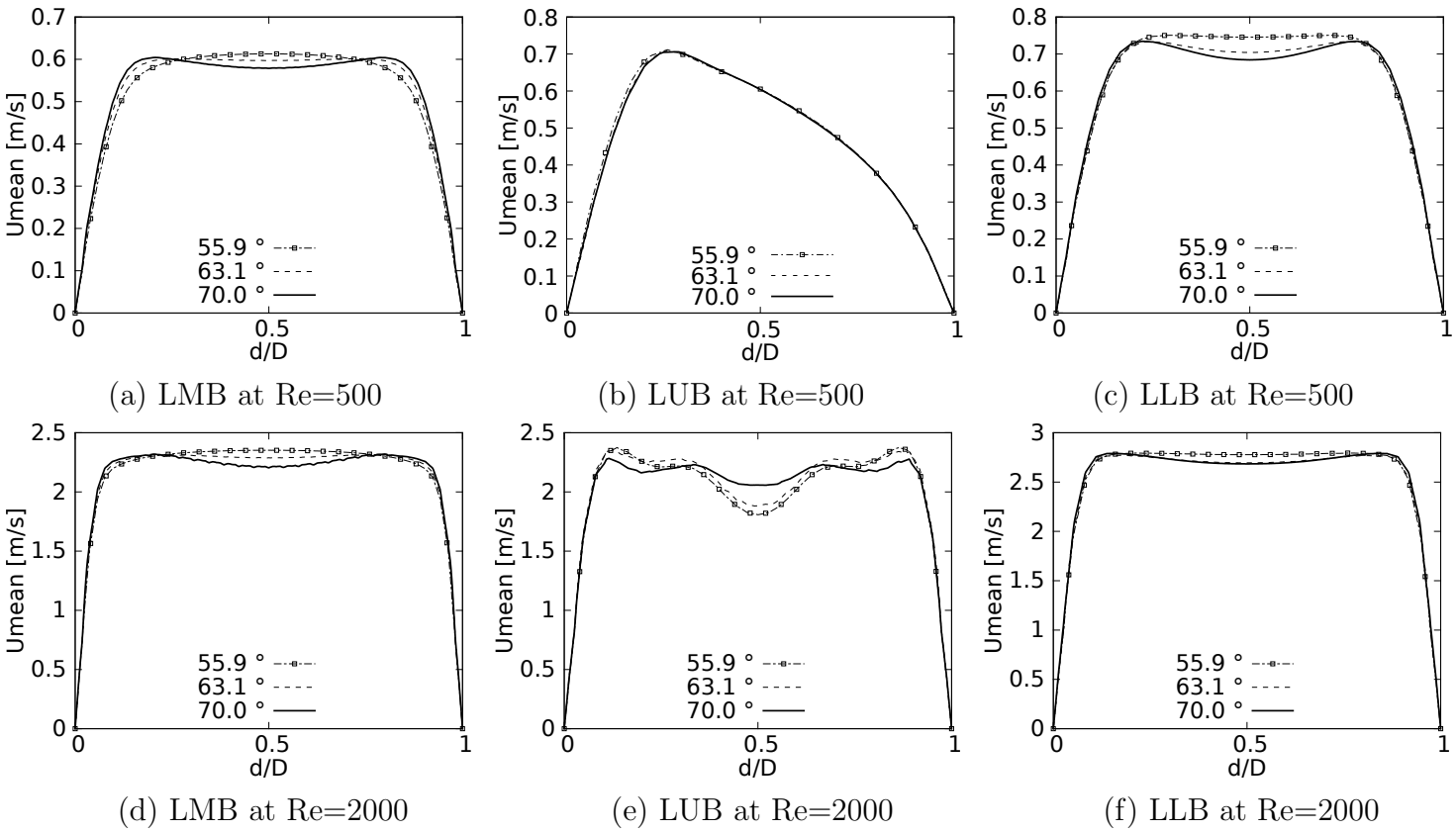

(a) LMB at Re=500 (b) LUB at Re=500 (c) LLB at Re=500

(d) LMB at Re=2000 (e) LUB at Re=2000 (f) LLB at Re=2000

Figure 3-10.: Velocity profiles on sagittal plane

These effects are stronger for smaller BA values, for which an M-shaped behaviour is obtained again.

The secondary flow patterns in inhalation stage for angle 55.9Â° are shown in Figure **3-12**, Figure **3-13** and Figure **3-14**. In the range of bifurcation angles studied, no clearly noticeable pattern was observed. However, in many cases a particular relationship between the vortical structures and the velocity and vorticity profiles are noticeable.

It can be seen in Figure **3-12**, as the flow is transported within the LMB, two vortices (also Known as dean vortex, Dean [30]) and two saddle points (sinks) are identifiable through the secondary flow. These vortical structures are symmetrical respect to the coronal plane. This distribution has been observed experimentally by Dean [30]; Schroter and Sudlow [98]; Fresconi and Prasad [36], and analyzed in detail by Snyder and Olson [106]. As the inlet velocity increases, this structures undergo a relocation moving away towards the outer wall of the airway, as shown in Figure **3-12** (b) for Re 2000.

Interposing the velocity and vorticity profiles (hereinafter called "V-W profile") in a non-dimensional axis, taken in coronal plane, it is possible to observe how the velocity peak coincides with the point of least vorticity, therefore consistent with the location

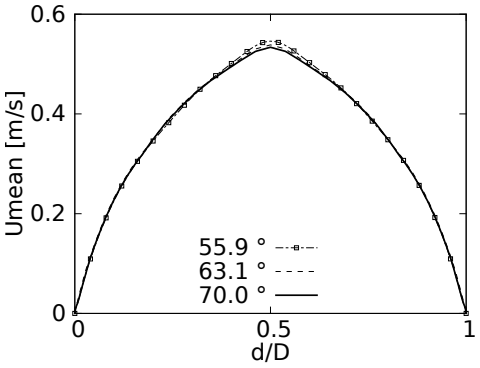

(a) Re=500 on coronal plane

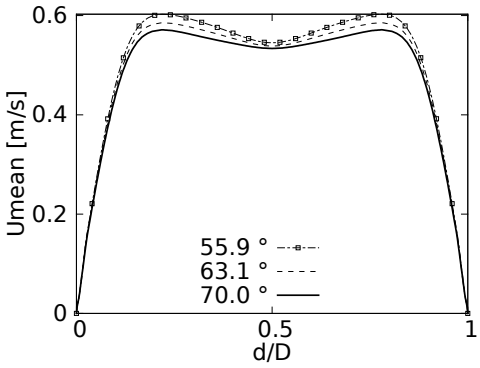

(b) Re=500 on sagittal plane

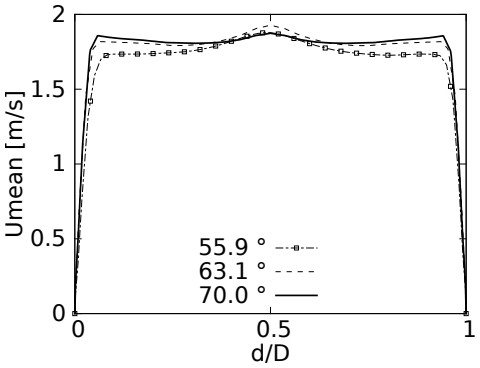

(b) Re=2000 on coronal plane

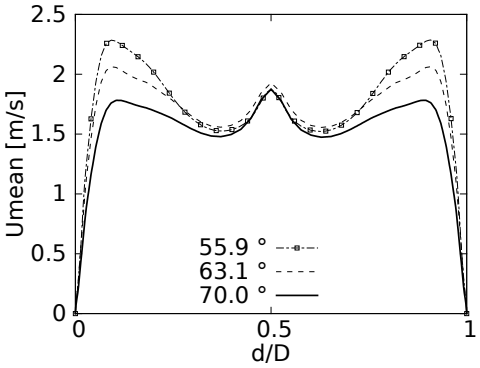

(b) Re=2000 on sagittal plane

Figure 3-11.: Velocity profiles at exhalation stage for TRA branch

of the saddle point on the secondary flow.

Secondary flow patterns in LLB can be seen in Figure **3-13**. It is possible to observed the onset of two new vortices, inducing the saddle point to move towards to the center of the airway. This behaviour is clearly defined for the numerical experiments with greater Reynolds numbers (Figure **3-13** (b) for Re 2000, for instance). In this case, the relationship between V-W profile previously identified continues to be fulfilled, even with the presence of these new structures.

Figure **3-14** shown the patterns for LUB. Two vortices appear for low velocities, and, as Re increase, new vortical structures appear towards the outer wall of the airway. Newly, V-W profile and vortical structures are related, although for greater Re a peak velocity and a minimun vorticity point are more difficult to determine, as can be seen Figure **3-14** (b).

By analysing the secondary flow patters at exhalation stage for the TRA airway, as shown in Figure **3-15** and Figure **3-16**, it can be seen how the vortical structures have a symmetrical shape in both sagittal and coronal plane (as well as the velocity profiles). For low Reynolds numbers is evidenced the presence of four vortices, which

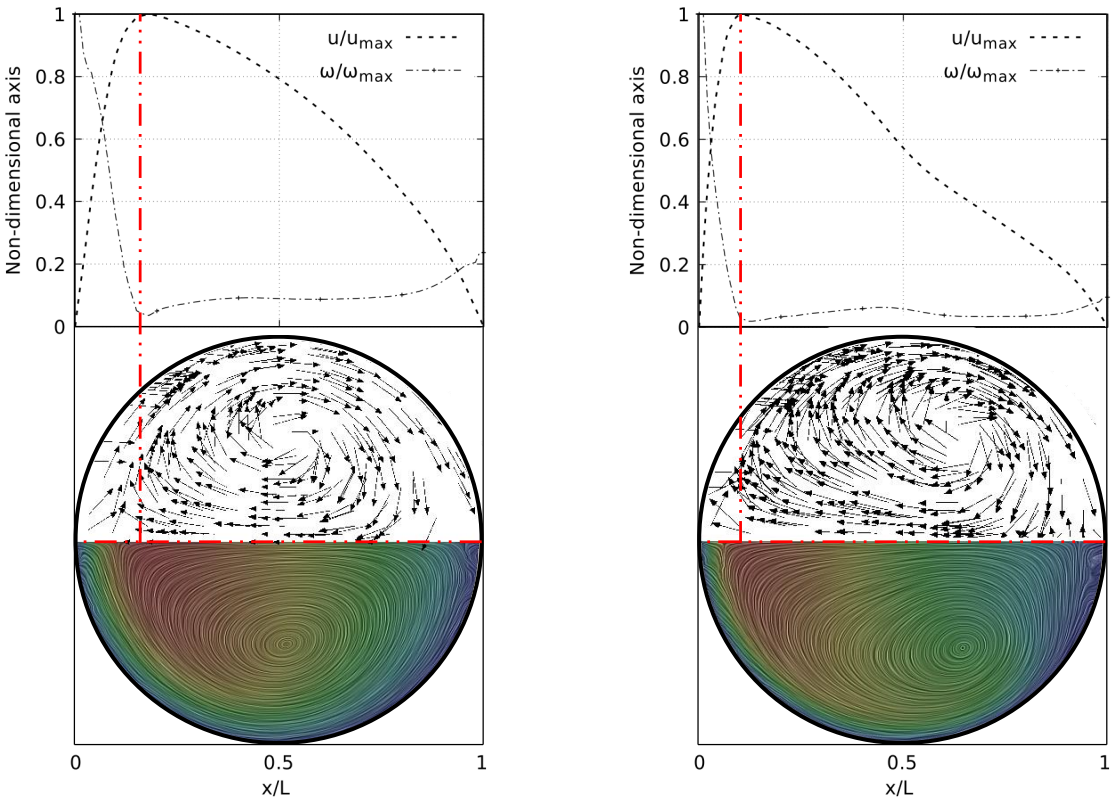

(a) Re 500 (b) Re 2000

Figure 3-12.: V-W profile (taken at coronal plane) and secondary flow patterns in LMB airway. Inhalation stage.

rotate towards the centre of the branch (reported in others investigation works as those developed by Schroter and Sudlow [98]; Fresconi and Prasad [36]). For larger Reynolds numbers the appearance of up to eight vortices is observed. As in inhalation stage, by reviewing the V-W profiles, it is possible to verify how the peaks velocity and the low vorticity points are align with the saddle points, condition valid for both the coronal plane and the sagittal plane. In fact, in the sagittal plane, Figure **3-16**, it is seen how this phenomenon occurs not only in one point, but in three coincident points.

Exploring flow patterns in the LMB airway at coronal plane, we can noticed the appearance of four totally developed vortex. The saddle point tends to the center of the airways, and it is in line with the V-W profile as Figure **3-17** shows.

Pressure drop behaviour, as explained by Pedley et al. [86], is directly influenced by changes in kinetic energy and by the dissipation of viscous energy. These phenomena are associated with the airway morphology, being affected by the geometric parameters as the flow is transported from the trachea to the alveoli. Plots of ΔP versus x/L (a normalizad length along the axial axis of the branches) are presented in Figure **3-18**, for

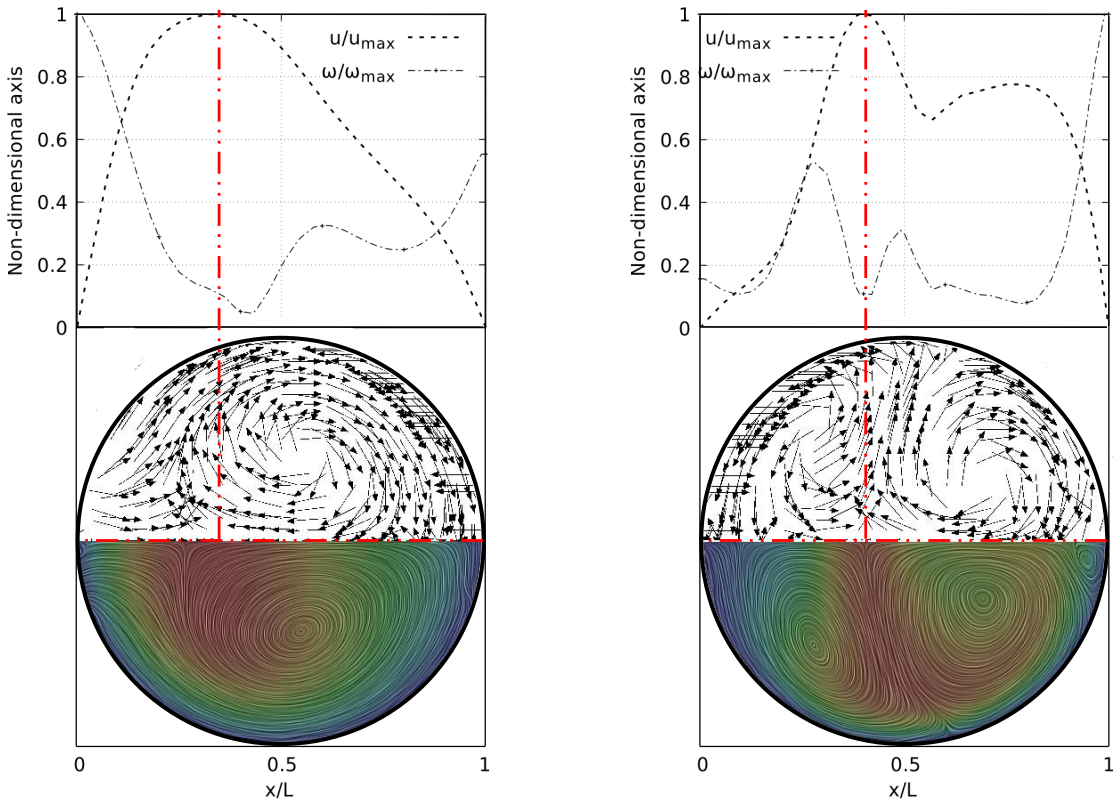

(a) Re 500 (b) Re 2000

Figure 3-13.: V-W profile (taken at coronal plane) and secondary flow patterns in LLB airway. Inhalation stage.

different Re. In all cases a local growth at the beginning of the axial line is evidenced, which is due to local increase of pressure gradients at the bifurcation. This increase is greater as the angle increases, a phenomenon observed in all generations for all the cases explored. These results are in line with the numerical study in micro-channel networks developed by Wang et al. [114], where an increase of the angle generates an increase in the pressure drop.

It is also observed that such local growth is greater for LLB path, as compared to LUB (both belonging to the second generation). This effect is thus related with the velocity profiles previously shown in Figure **3-9** (c), where it was observed that for LLB a greater acceleration of the flow is attained. In this case, decreasing the dimensionless pressure drop seems to be strongly associated with the rise of the peak of the velocity profile presented in Figure **3-9** (c). The behaviour of the pressure drop hereby described is kept as the Reynolds number increases. For instance, as shown in Figure **3-18** (d)-(e)-(f), the same trends were obtained for Re=2000, both in terms of angle and local growth.

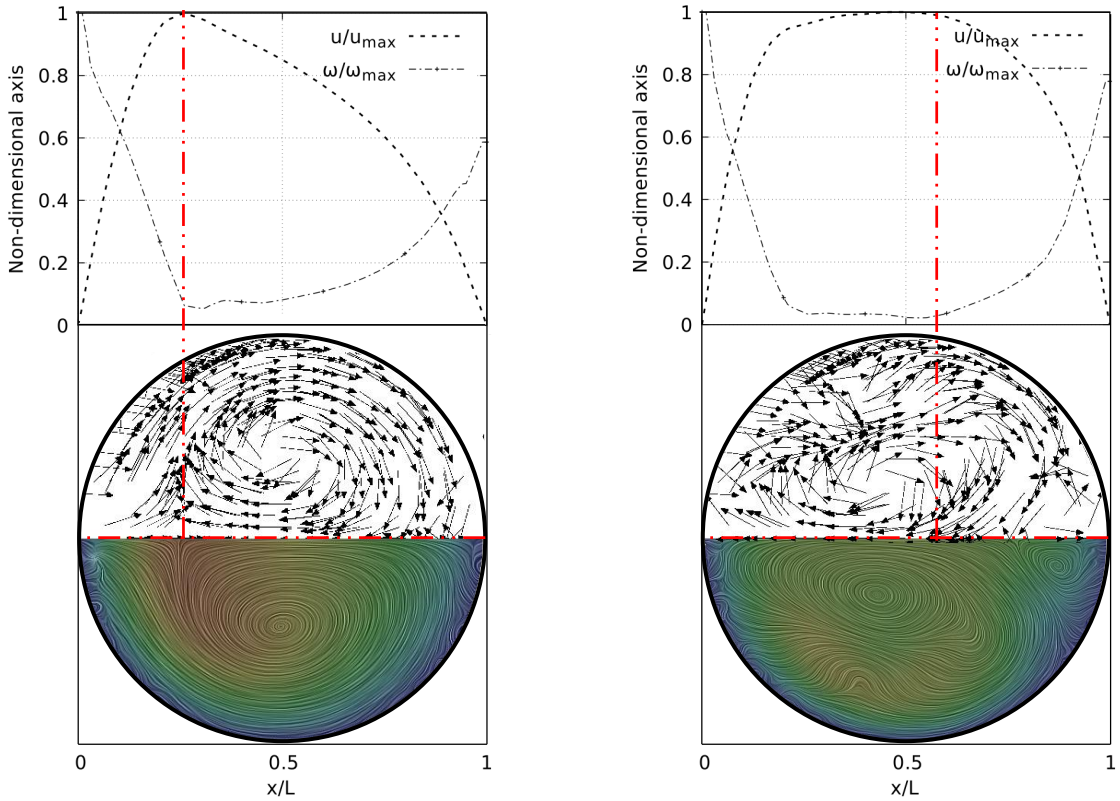

(a) Re 500 (b) Re 2000

Figure 3-14.: V-W profile (taken at coronal plane) and secondary flow patterns in LLU airway. Inhalation stage.

To analyze the pressure drop behaviour versus Reynolds number, a normalized pressure drop coefficient was computed as the ratio between the weighted mass integrals of the pressure at the inlet and the outlets for the different numerical experiments. This coefficient was computed using the following function(Liu et al. [63]):

$$Cp = \frac{P_{1,Total} - P_{3,Total}}{P_{1,Dynamic}} \tag{3-2}$$

Where $P_{1,Total}$ is the mass-weighed integral of the total pressure over the inlet section, $P_{3,Total}$ is the mass-weighted integral of the total pressure over the four outlet sections (i.e., performing an integral over each outlet and summing over each outlet) and $P_{1,dynamic}$ is the mass-weighed integral of the total pressure over the inlet section, defined as:

$$P_{1,Total} = \frac{\int_{A_1}(p + 0{,}5\rho(u^2 + v^2 + w^2))\rho\vec{V}d\vec{A_1}}{\int_{A_1}\rho\vec{V}d\vec{A_1}} \tag{3-3}$$

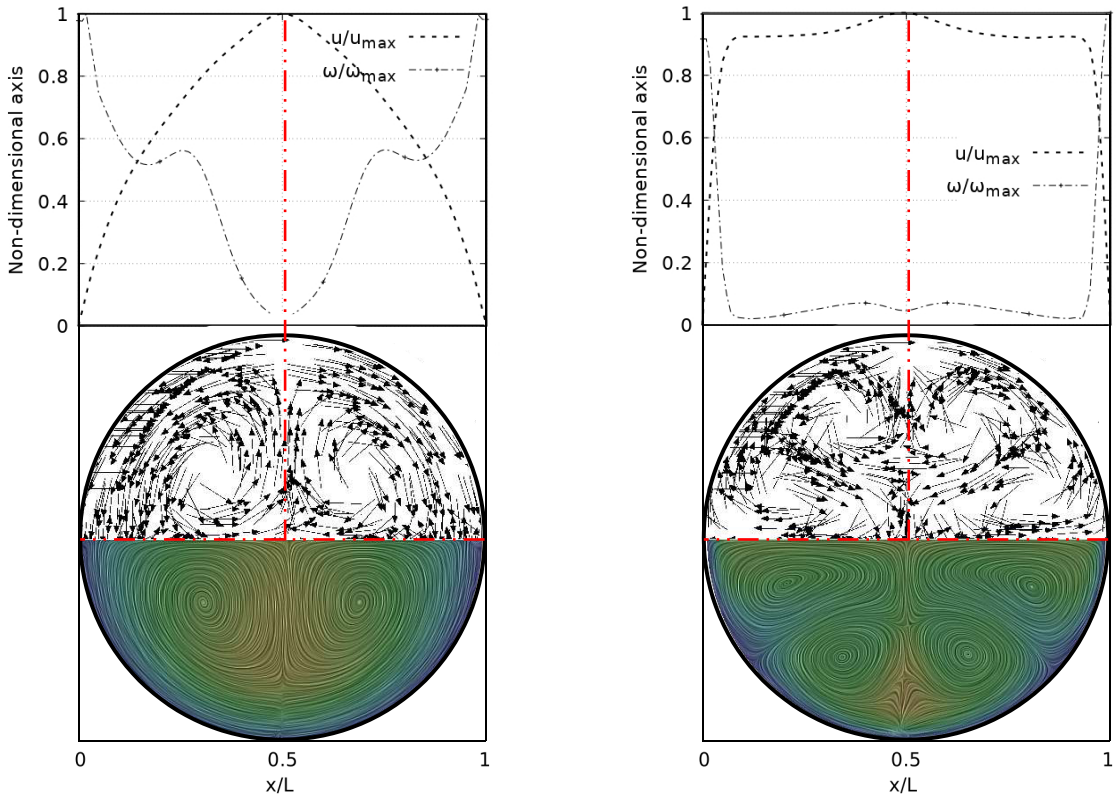

(a) Re 500 (b) Re 2000

Figure 3-15.: V-W profile (taken at coronal plane) and secondary flow patterns in TRA airway. Exhalation stage.

$$P_{3,Total} = \frac{\int_{A_3}(p + 0{,}5\rho(u^2 + v^2 + w^2))\rho\vec{V}d\vec{A_3}}{\int_{A_3}\rho\vec{V}d\vec{A_3}} \tag{3-4}$$

$$P_{1,Dynamic} = \frac{\int_{A_1} 0{,}5\rho(u^2 + v^2 + w^2)\rho\vec{V}d\vec{A_1}}{\int_{A_1}\rho\vec{V}d\vec{A_1}} \tag{3-5}$$

Here, A_1 and A_3 denotes the inlet and total outlet area, respectively, and u, v and w are the velocity components. The behaviour of this coefficient relative to the Reynolds number is shown in Figure **3-19**. Trends for only a reduced number of the angles are shown, since they capture the observed general tendency.

As expected, the pressure coefficient is higher for the greater BA, being consistent with the pressure drops across the axial lines. Moreover, this coefficient decreases as the Reynolds number increases, result in line with the formulation and curves presented by Liu et al. [63].

The pressure drop profiles in the exhalation state for Re=500 are shown in Figure **3-20**. These curves are taken in the upstream direction, i.e., from the last generation towards

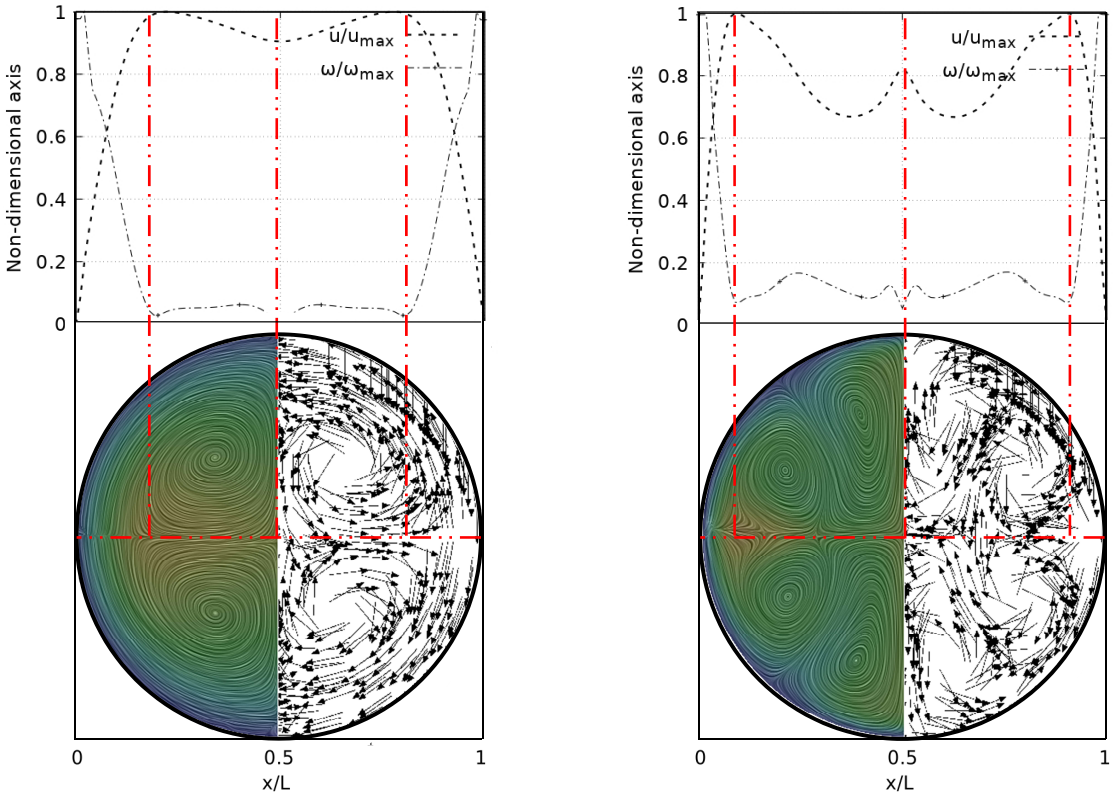

(a) Re 500 (b) Re 2000

Figure 3-16.: V-W profile (taken at saggital plane) and secondary flow patterns in TRA airway. Exhalation stage.

the trachea (where a value of 0 Pa was prescribed at the inlet). Contrary to the results obtained during inhalation, for this case no behavior defined by the bifurcation angle is observed, since the curves for the different BA cross each other with no apparent order.

Different numerical studies have shown that the maximum shear stresses, developed during inhalation and exhalation process, are located on the inner and externals wall, respectively.

In a similar manner as discussed with the pressure drop, and as it might be expected, this behaviour of the WSS is also strongly related to the specific changes of the velocity profiles reported in this paper. Particularly, the previously discussed tendency of displacement of the peak of the profiles (shown earlier in the Figure **3-9**) is always associated to the appearance of regions of maximum wall shear stress.

Wall shear stress was measured along to the inner wall (for inhalation) and in a perpendicular direction of the inner wall (for exhalation) on each of the branches. In the different plots (Figure **3-21** and Figure **3-22**), the length is presented in normalized

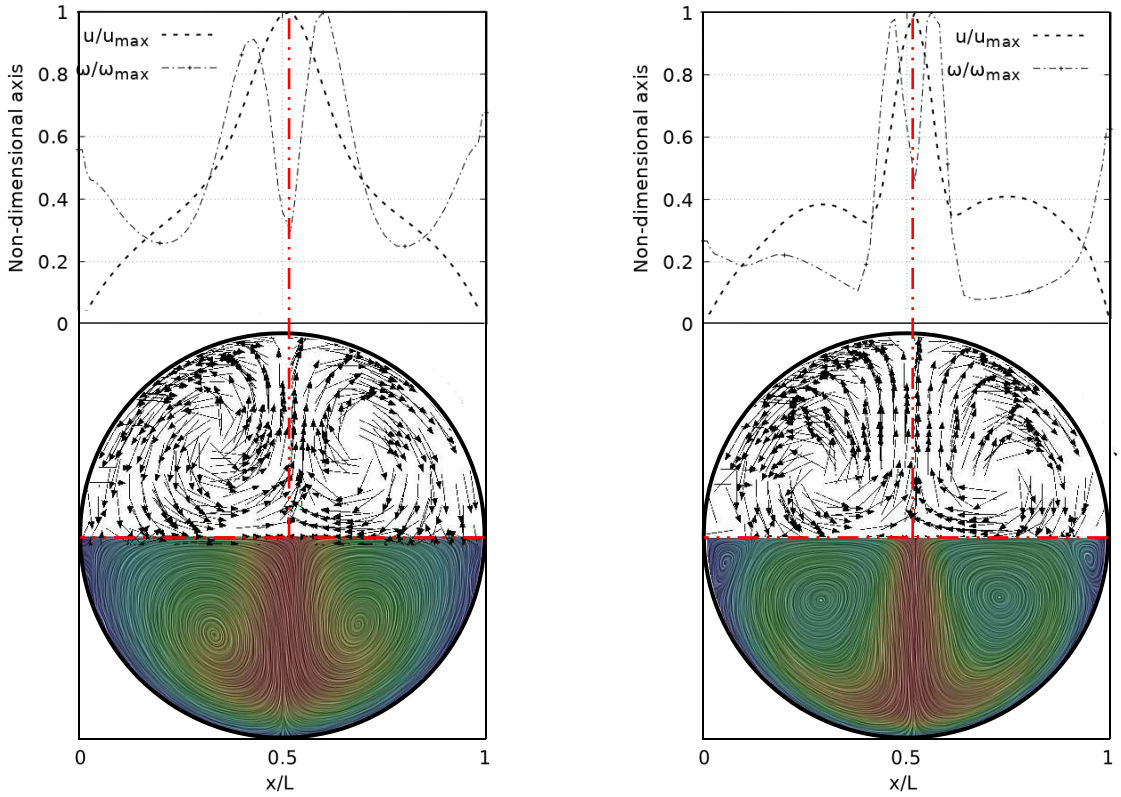

(a) Re 500 (b) Re 2000

Figure 3-17.: V-W profile (taken at coronal plane) and secondary flow patterns in LMB airway. Exhalation stage.

form (x/L, where L is the total length of the branch). In all cases, for the x-label, the value of 0 and 1 refers to the upstream and downstream, respectively. The unit of the magnitude of the WSS is [Pa].

By analysing the effect of the bifurcation angle (BA) on the wall shear stress distribution for the inhalation process, it is possible to determine that, as observed in different studies, the maximum shear stress is located towards the intersection of the bifurcation, that is in the region nearby the joints. It is further observed that for the different branches, as the BA considered is augmented, the magnitude of the maximum WSS decreases, giving as a result that, for instance, the highest figures for WSS are observed for the smallest angle, which in the present study is BA=55,9^o. Examining the WSS in each of the branches, along the local axial direction and therefore progressing through the branching line, the WSS seem to collapse reaching an average common value regardless of the BA explored. This trend, however, is sightly disrupted in LLB (Figure **3-21** (c)-(f)), where it is possible to appreciate a very subtle difference between the Mean values of wall shear stress attained for BA=63,1^o in comparison to the other BA explored. Thus, it can be established that the shear forces vary with respect to the bi-

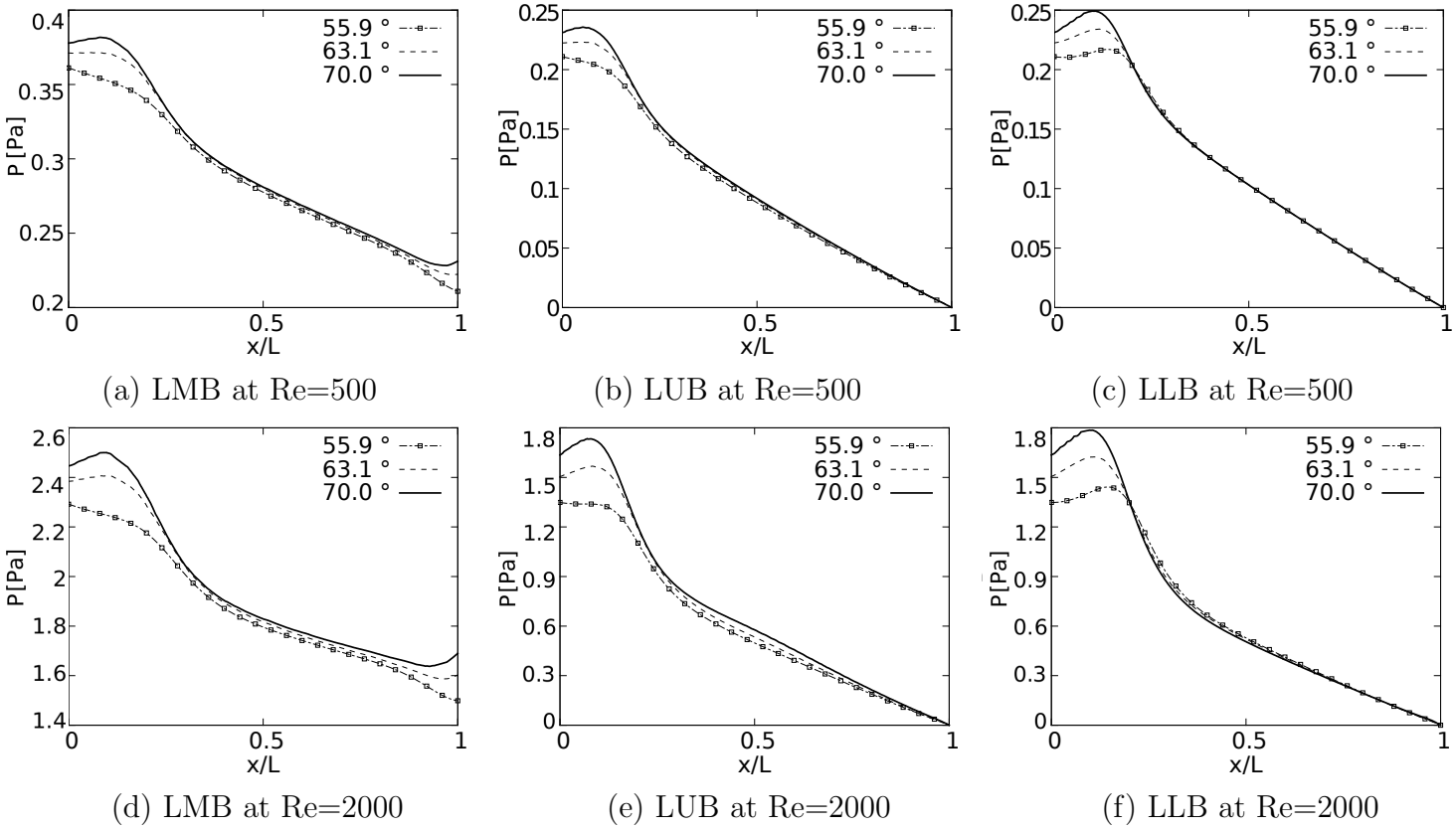

(a) LMB at Re=500 (b) LUB at Re=500 (c) LLB at Re=500

(d) LMB at Re=2000 (e) LUB at Re=2000 (f) LLB at Re=2000

Figure 3-18.: Pressure drops across the axial axes of the branches at inhalation stage

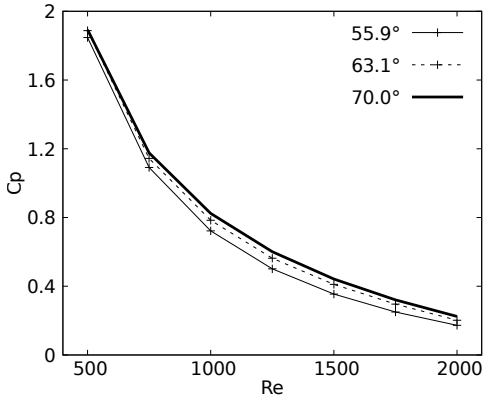

Figure 3-19.: Pressure drop coefficient (Cp) vs Reynolds number

furcation angle only in the zones or regions near the bifurcation point, but converging to an average value downstream of such a point when considering inhalation.

The results obtained for the exhalation process, and presented in Figure **3-22**, show a complete different picture for the distribution of the wall shear stresses, at least in

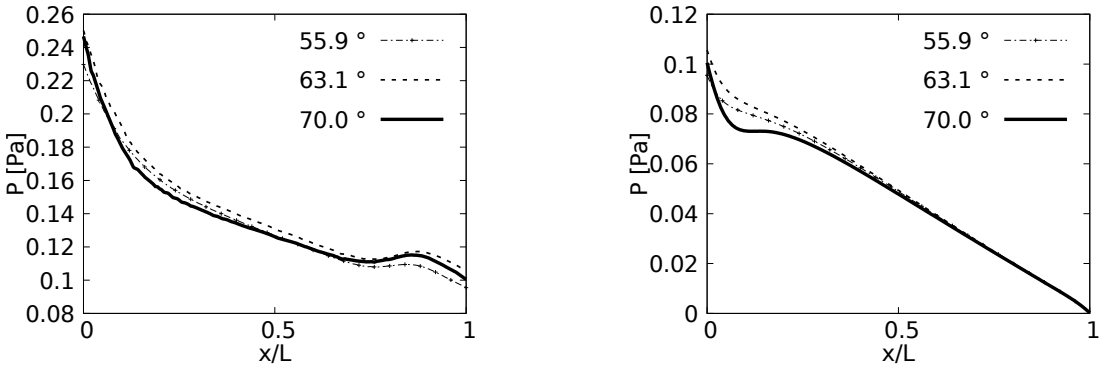

(a) LMB at Re=500 (b) TRA at Re=500

Figure 3-20.: Pressure drops across the axial axes of the branches at exhalation stage

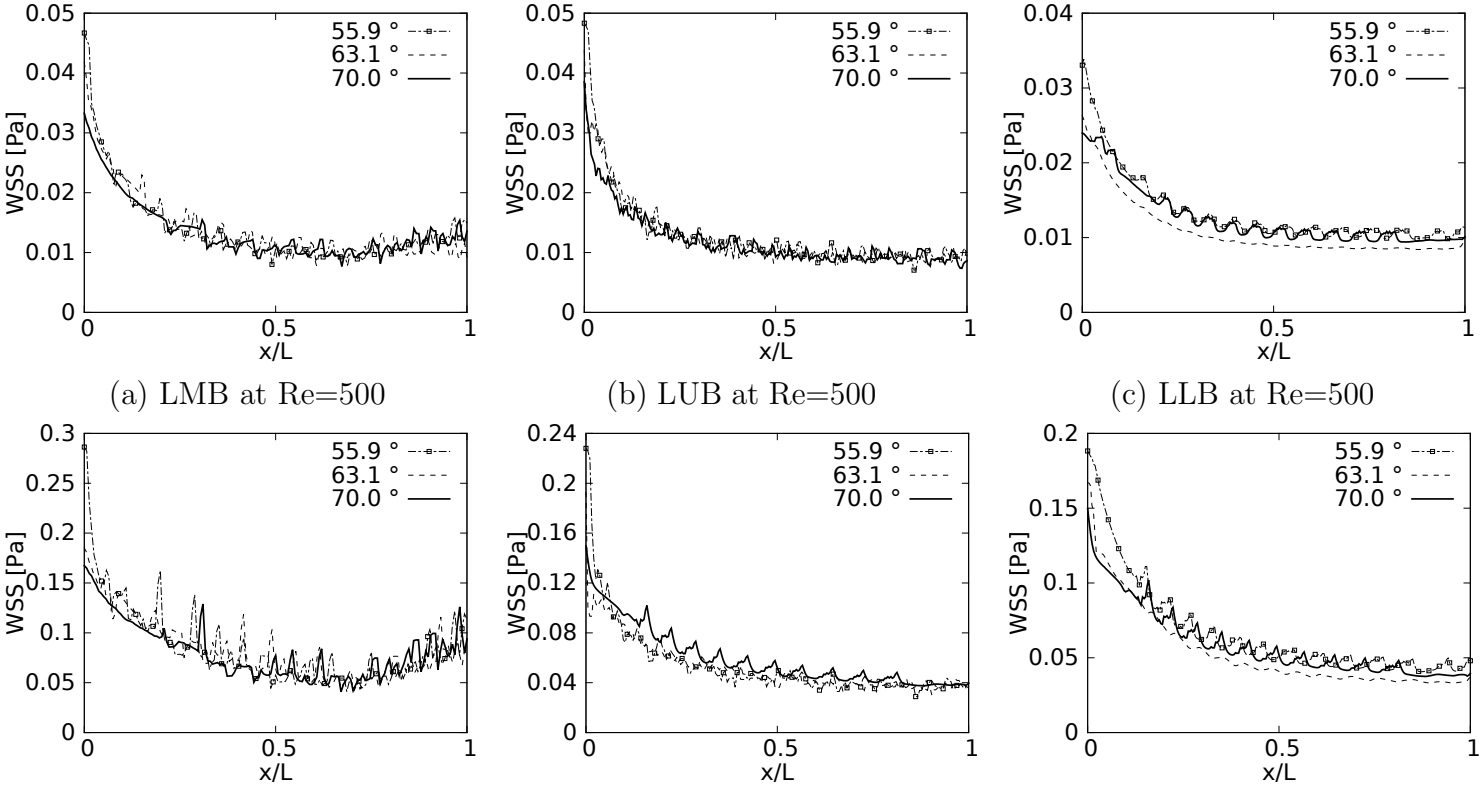

(a) LMB at Re=500 (b) LUB at Re=500 (c) LLB at Re=500

(d) LMB at Re=2000 (e) LUB at Re=2000 (f) LLB at Re=2000

Figure 3-21.: Wall Shear Stress on inner wall for inhalation

comparison with the inhalation process described just above. For instance, it is possible to observe that exhalation brings about an increase of the WSS in the first half of each branch, so the maximum values of WSS are present between $0{,}2 < x/L < 0{,}5$. In this case x/L is measured from the upstream bifurcation following the downstream direction and, as mentioned previously, using as normalising factor the length of the

respective branch L. In any case, for all the branches, there is a reduction of the WSS that seems to have a similar behaviour for the different angles considered in this work. In this exhalation process, however, a converging or collapsing trend to an average value is not clear. Noteworthy, the maximum WSS in each branch is accompanied by strong oscillations, albeit this oscillatory tendency is stronger for LMB than for the TRA. This particular effect may be related to the onset of flow instabilities and eventually some perturbations which grow in the flow direction as a result of the increment of the local flow rate and cross section area. A clear indication of this phenomena is increase of the local Reynolds number as the fluid flows downstream towards the TRA.

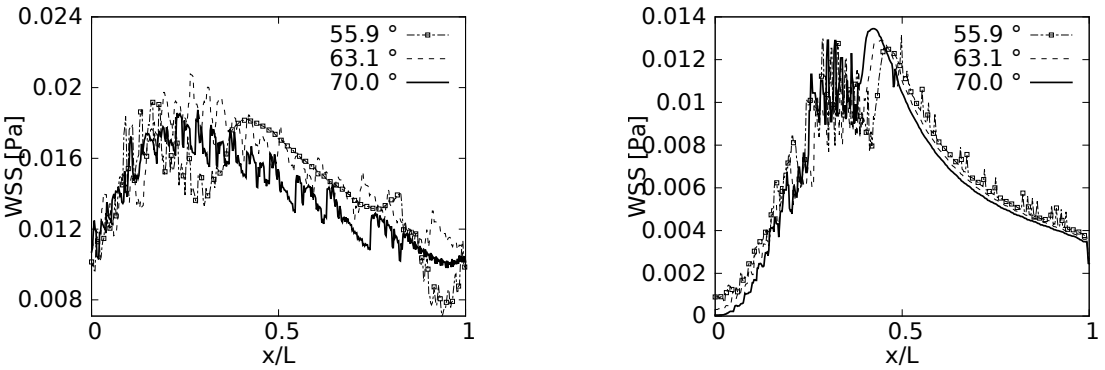

(a) LMB at Re=2000 (b) TRA at Re=2000

Figure 3-22.: Wall Shear Stress on outer wall for exhalation

3.2.2. Effect of carina rounding radius

Another relevant morphological parameter is the Carina Rounding Radius (CRR). The bifurcation point between the trachea and main bronchus are known as carina. Martonen et al. [68] specifies four geometrical configurations for this parameter: blunt, parabolic, saddle, and asymmetric. These shapes have an effects on flow acceleration, being the saddle the configuration that presents regions with the highest flow intensities and particle propagation. Some synthetic airway models do not directly consider the shape of the carina. Some research as theses carried out by Horsfield et al. [46] and Kang et al. [53] introduce a relationship between the rounding radius of the carina and the diameter of the main branch. Models as the one developed by Lee et al. [59] are based on such considerations.
In order to analyze the influence of carina rounding radius (CRR) of lower human airways on the respiratory processes, numerical simulations of airflow during inhalation were performed using a synthetic bifurcation model. Geometries for the airways models were parameterized based on a set of several CRR's. A range of two Reynolds numbers (Re) relevant to the human breathing process were selected to analyzed the airflow behaviour.

- ◇ **Geometry**

For the study of the carina rounding radius (CRR), a synthetic airways model based on the bifurcation geometry proposed by Lee et al. [59] was selected. Parameters and values for the implementation of this model can be observed in Figure **3-23** and Table **3-5**. Those generations represent the trachea and the main bronchus. As in the BA study, for this geometry the length of the last generation branches was extended to be at least five times the related outlet diameter. The parameters R_d and α describe the curvature of the bifurcation. A dimensionless version of CRR is define as

$$r_c = \frac{CRR}{\frac{D_t}{2}} \tag{3-6}$$

where r_c is the dimensionless rounding radius and D_t the trachea diameter. Generally the value of r_c does not exceed 0.2 (Horsfield et al. [46], Kang et al. [53]). For this research, the values of $r_c = 0$, $r_c = 0{,}07$ and $r_c = 0{,}14$ were selected.

Branch	**D (mm)**	**Len. (mm)**	α (^{o})	**Rd (mm)**
TRA	16	80	35	81.5
LMB / RMB	14	70		

Table 3-5.: Model Parameters values

◇ **Numerical Model**

For this study, the working fluid is air. The governing equations are described in Eqs. 2-6 and 2-7. The preferred numerical configuration described in section 2.2.2 was selected. The average number of tetrahedral cells was 1.5e6. In order to most reliably capture the phenomena near the bifurcation point, a finer refinement zone around the junction, as shown in the Figure **3-24**, was performed.

◇ **Boundary conditions**

For the evaluation of the effect of the CRR only inhalation breathing process was numerically simulated. An uniform pressure boundary condition at the outlets was prescribed . A parabolic velocity profile at the trachea inlet was adopted, covering a set of two Reynolds numbers of 500 and 2000. A Dirichlet no-slip boundary condition was applied.

◇ **Results**

As well as the bifurcation angle, the effect of the CRR on velocity profiles has not been extensively studied. In the investigation of Martonen et al. [68] on carina shapes is possible to observed how a skewed profile influence the flow intensities, as the particle propagation across the branch. Figure **3-25** and **3-26** shows the velocity profiles taken on coronal plane taken at different branch lengths.

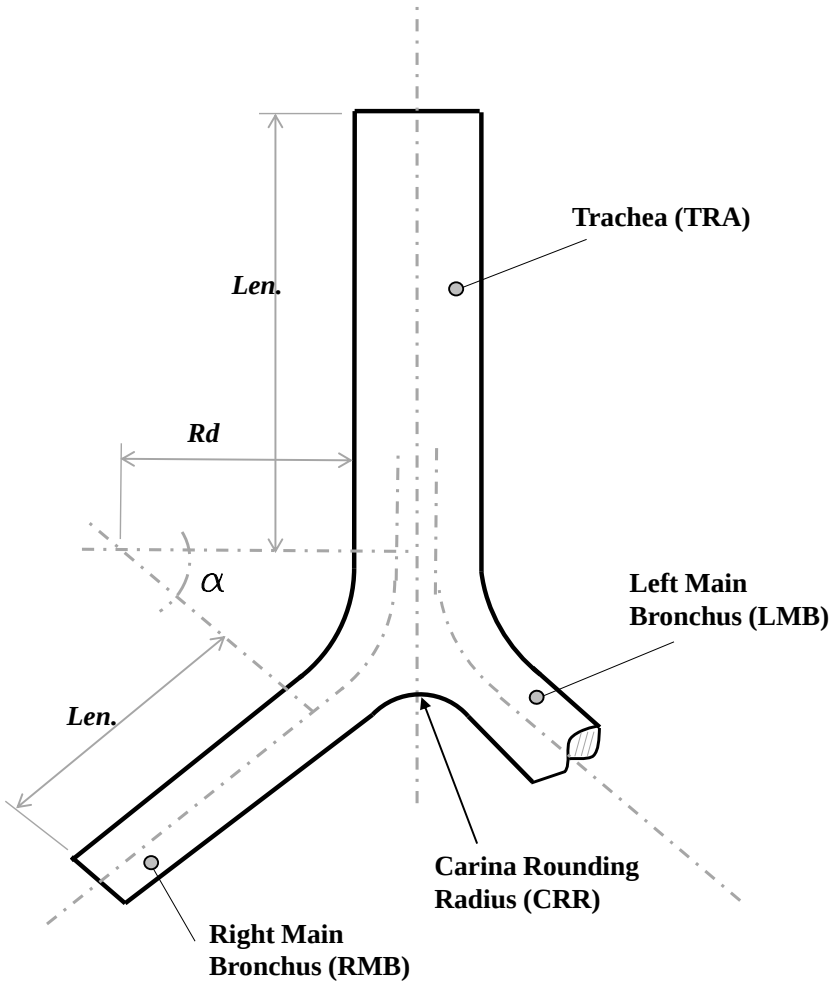

Figure 3-23.: Bifurcation model geometry

It can be seen how the smoothing of the bifurcation joint have a slight effect on the peak velocity profile, influence the narrowing of the shape toward to the inner wall, being more noticeable as the CRR grows. It should be noted that these effects are more visible near the carina (Figure **3-25**), and they fade as one advances through the branch (Figure **3-26**).

For velocity profiles on sagittal plane a particular behaviour is more noticeable. An increment in the CRR result in a greater accelerating of the fluid, as is shown in Figure **3-27** and **3-28**, getting a greater peak profile for $r_c = 0{,}14$. As the fluid moves through the airway, the characteristic M shape is again evidenced, and it can be seen how the particular decelerating in the center of the axis keep the tendency, being more pronounced for larger CRR's.

Vorticity profiles (nondimensional ω/ω_{max}) are taken across a line on coronal plane,

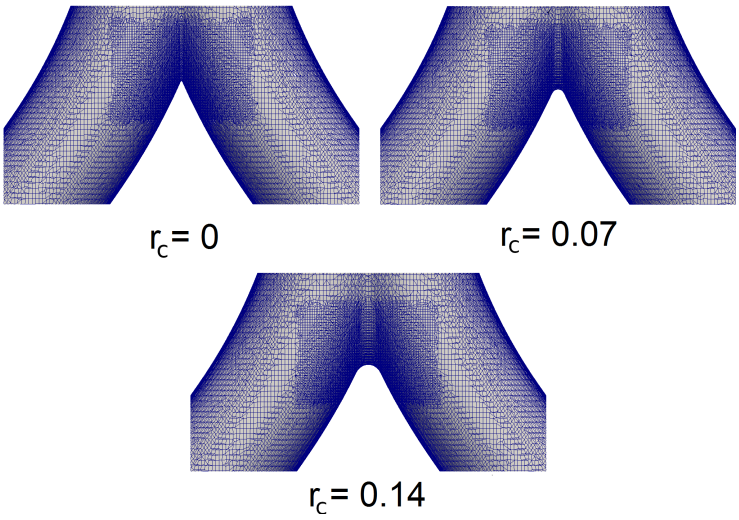

Figure 3-24.: Refinement near the carina

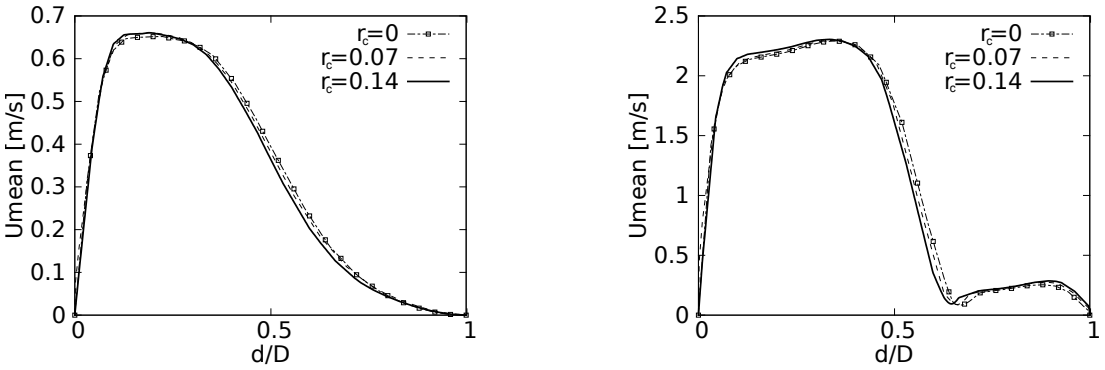

(a) Re=500 (b) Re=2000

Figure 3-25.: Velocity profiles on coronal plane. Taken at 20 % of the LMB length

as shown in Figure **3-29**. To appreciate the effect of the CRR, these measure are taken near to the carina. It can be seen how the maximum intensity is developed in the inner wall, and also the existence of a peak near to the center axis, peak that is more pronounced for greater rounding radius. This trend continues for Re 2000. This behavior disappears as you move along the branch, so that the curves at 50 % branch length are not displayed.

As with the vortical structures seen through the secondary flow patterns, no effects derived from the CRR variation were observed. However, as can be seen in Figure **3-30**, it is possible to corroborate that, as in the BA studies, dean vortices (Dean [30]) and two saddle points are identifiable, preserving the relationship between the location of these vortical structures with the velocity and vorticity profiles. These sections were

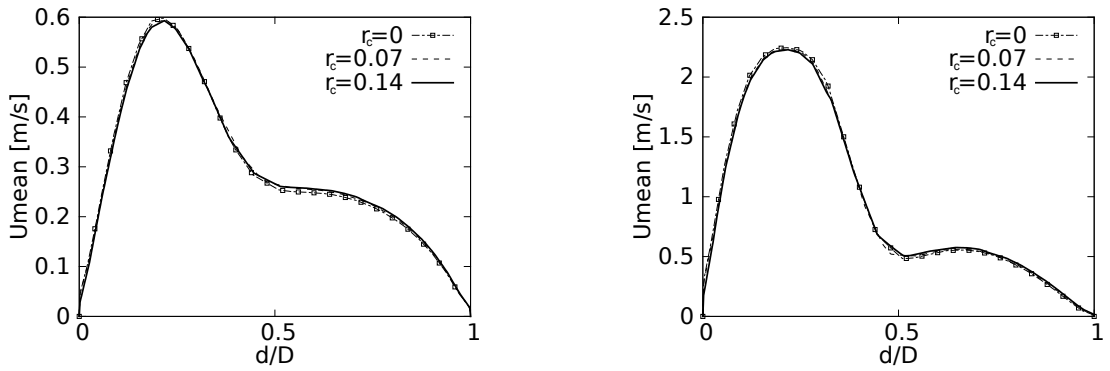

(a) Re=500 (b) Re=2000

Figure 3-26.: Velocity profiles on coronal plane. Taken at 50 % of the LMB length

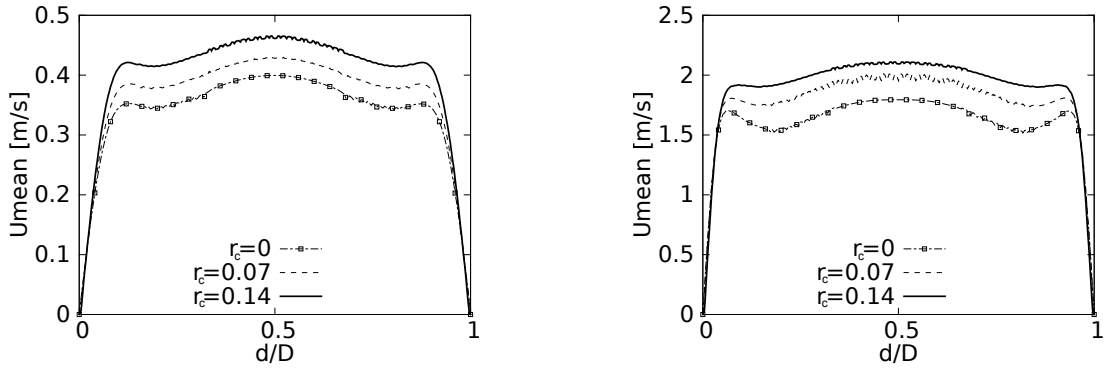

(a) Re=500 (b) Re=2000

Figure 3-27.: Velocity profiles on sagittal plane. Taken at 20 % of the LMB length

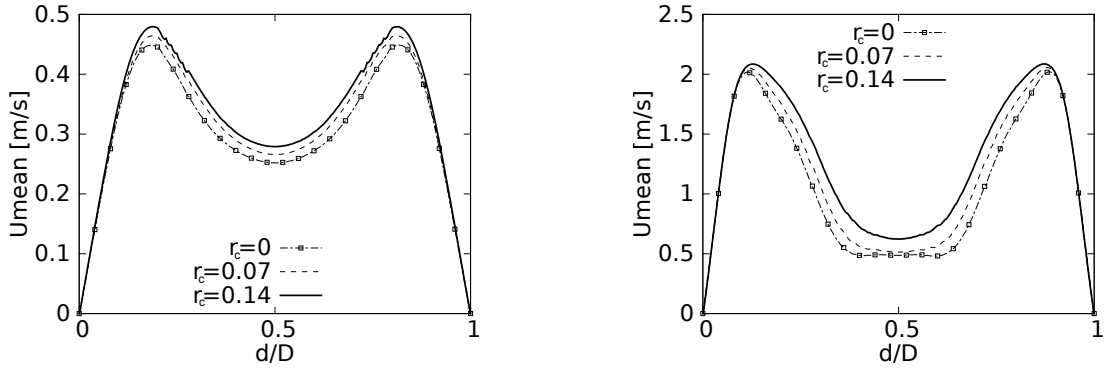

(a) Re=500 (b) Re=2000

Figure 3-28.: Velocity profiles on sagittal plane. Taken at 50 % of the LMB length

taken at 20 % of the branch length (Figure **3-30** (a)) and 50 % of the branch length (Figure **3-30** (b)), in the geometry corresponding to $r_c = 0$ at Re=2000.

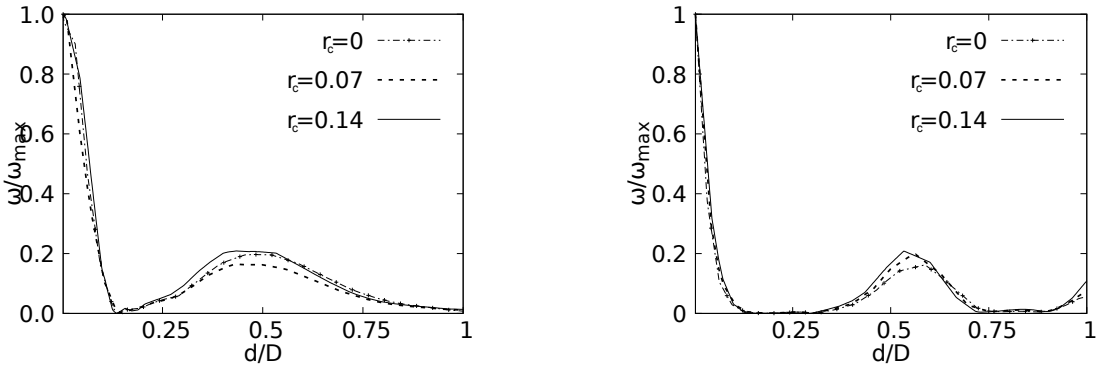

(a) Re=500 (b) Re=2000

Figure 3-29.: Vorticity profile on coronal plane. Taken at 20 % of the LMB length

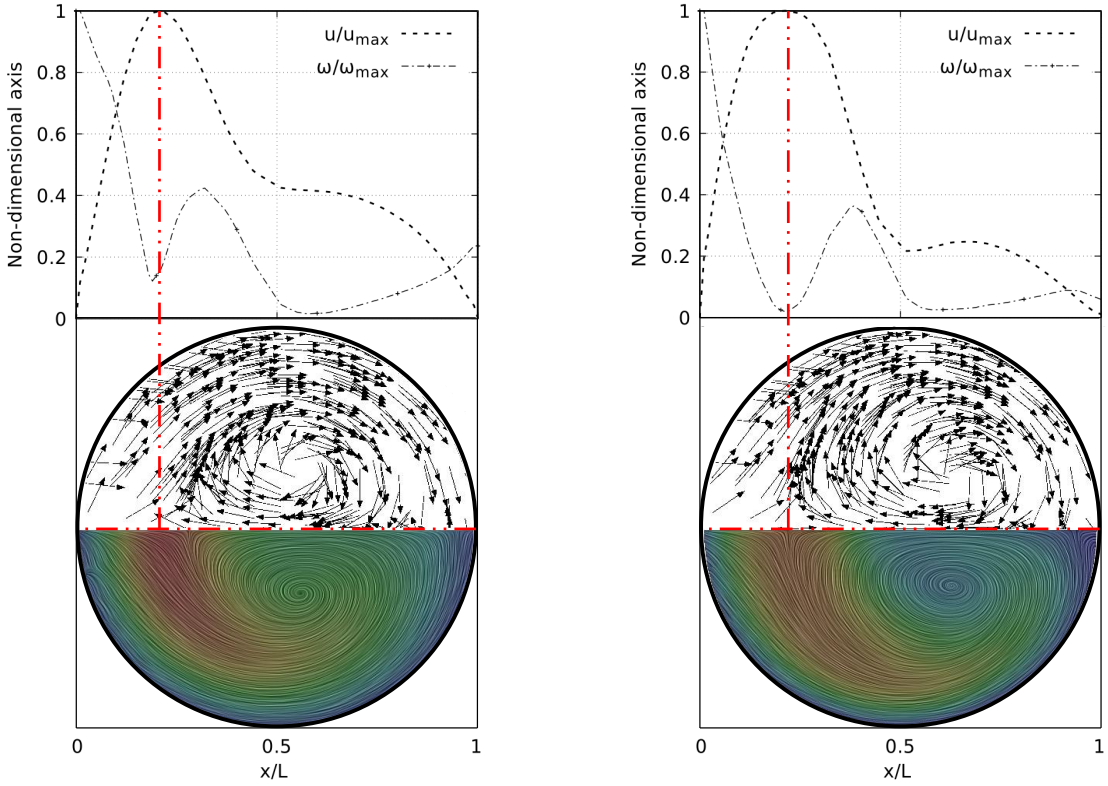

(a) 20 % of the branch length (b) 50 % of the branch length

Figure 3-30.: V-W profile (taken at coronal plane) and secondary flow patterns in LMB airway.

The pressure drops ΔP, measured on the internal wall line, are shown in Figure **3-31**. These show only 20 % of the length (normalized with respect to the total length of the branch, x/L), since no particular effect is identified beyond this point. For both Re 500 (Figure **3-31** (a)) and Re 2000 (Figure **3-31** (b)) it can be seen that both the

maximum pressure value and the drop ΔP are higher for the larger CRRs.

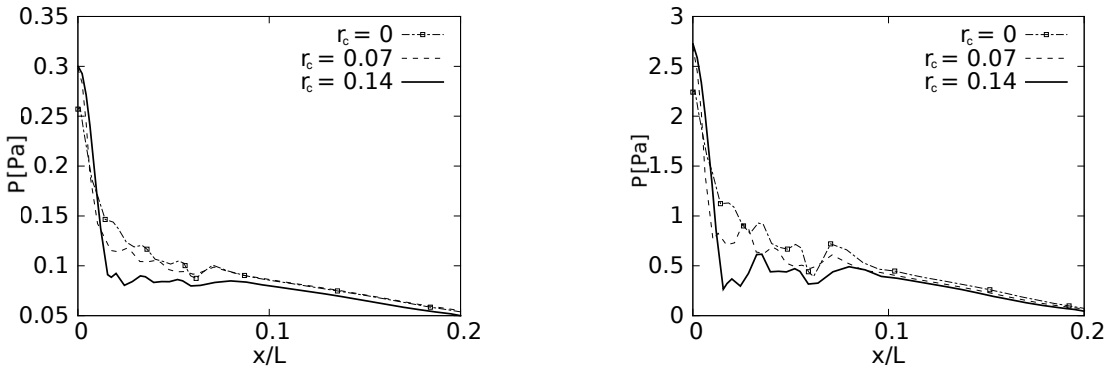

(a) Re=500 (b) Re=2000

Figure 3-31.: Pressure drop through the branch inner wall

The Wall shear stresses, measured in the inner wall, has also a strong effect related to the branch joint smoothing. As shown in Figure **3-32**, for a straight joint, i.e. $r_c = 0$, the maximum WSS will be located exactly in the intersection point, acting as a stress concentrator. As the joint is softened by increasing the CRR, this location of the maximum value is moving away downstream the airway wall and, as well as the pressure behavior, curves converge to the same value to each other. In this case, this convergence trend occurs at approximately 50 % of the branch length.

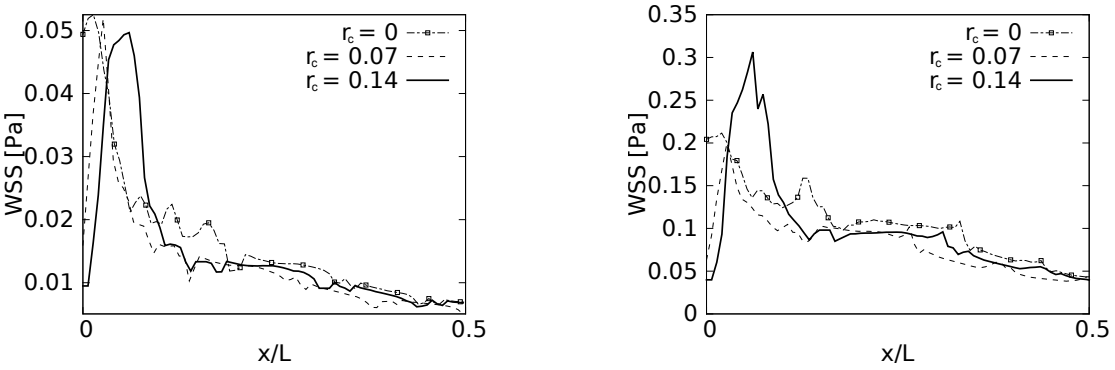

(a) Re=500 (b) Re=2000

Figure 3-32.: Wall Shear Stress on inner wall for inhalation

4. Reduced dimensional methodology based on homothety airway ratios

A fractal is an entity with a structure that repeats itself at various scales. Mandelbrot [66] was the one who introduced this concept, showing how these structures are found in nature itself. In the research on scaling laws in biology, West et al. [118] shows how different biological systems, including the circulatory system and the airways, can be described as fractal networks of branching tubes. For the characterization as fractals, West et al. [118] states that the radius and length dimensions of a generation k must correspond to a fraction of the exactly previous generation $k-1$. Thus, the length l_k of a branch is defined as $l_k = \alpha\, l_{k-1}$, where α is the length scaling factor. In the same way, the radius r_k is determined from $r_k = \beta\, r_{k-1}$, with β being the radius scaling factor. Prior to fractal development, a ratio of radii in ideal branched vessels was first developed by Rudolf Hess and later supplemented by Cecil Murray. This is known as the Hess-Murray's law. As detailed by Sciubba [99], this law dictates that for the minimization of the work of the biological system, the optimal value r_k/r_{k-1} is 0.7937. As indicated by West et al. [118], this 'work minimization' refers to decreasing viscous dissipation, thus finding the optimal structure (in terms of volume and resistance). Mauroy et al. [70] expands this idea of the optimal tree by including ***homothety ratios***, under the consideration that the ideal bronchial tree is a homothetic geometry, i.e., a succession of similar structures scaled by a homothety ratio h. Under this concept, it is possible to define the resistance and volume (and therefore the pressure drop) of all the generations of a homothetic bronchial tree, as the sum of the resistances and volumes of each generation multiplied by its respective homothety ratio. As demonstrated by Mauroy et al. [70], if the homothety ratio is considered to be constant for all generations, the minimization of the dissipated energy leads to an optimal value of $h = (1/2)^{1/3} = 0{,}7937$, i.e., the same value as determined by Hess-Murray's law.

In this chapter, a dimensional reduction methodology is described, implemented and validated, based on the fractal consideration of the airways tree and on the homothety ratios described by Mauroy et al. [70].

4.1. Algorithm development and validation

4.1.1. Mathematical development and Sensitivity analysis

The pressure drop in a pipe can be described by the *Hagen-Poiseuille* equation. Consider the first generation in a airways tree, composed only of a single parent branch. Applying a branch analogy to a circular cross-section pipe, the pressure drop can be calculated as:

$$\Delta P_0 \;=\; \frac{8\ \mu\ L_0}{\pi\ r_0^4}\ Q_0 \tag{4-1}$$

Where ΔP_0 is the pressure drop, μ the kinematic viscosity, L_0 the parent branch length, r_0 the parent branch radius and Q_0 the inlet volumetric flow. Let us now consider a symmetric tree with two generations, with daughter branch length L_1 and radius r_1. A homothety factor for the length, α_1, is defined as L_1/L_0. Similarly, we obtain a homothety ratio for the radius, α_2, given by r_1/r_0. For a symmetrical bifurcation, the initial volumetric flow is equally distributed through the branches. However, to give a generalized form of the flow distribution, we also define a homothety ratio for volumetric flow, α_3, defined by Q_1/Q_0. From the definitions described above, we can express the pressure drop for a branch of the second generation as

$$\Delta P_1 \;=\; \frac{8\ \mu\ L_1}{\pi\ r_1^4}\ Q_1 \;=\; \frac{8\ \mu\ (\alpha_1\ L_0)}{\pi\ (\alpha_2\ r_0)^4}\ (\alpha_3\ Q_0) \tag{4-2}$$

Assuming the homothety ratios are constant for all generations, the pressure drop for a branch belonging to the third generation will be given by

$$\Delta P_2 \;=\; \frac{8\ \mu\ L_2}{\pi\ r_2^4}\ Q_2 \;=\; \frac{8\ \mu\ (\alpha_1^2\ L_0)}{\pi\ (\alpha_2^2\ r_0)^4}\ (\alpha_3^2\ Q_0) \tag{4-3}$$

Thus, it is possible to generalize the pressure drop for a generation "n" as

$$\Delta P_n \;=\; \frac{8\ \mu\ L_n}{\pi\ r_n^4}\ Q_n \;=\; \frac{8\ \mu\ (\alpha_1^n\ L_0)}{\pi\ \alpha_2^{4n}\ r_0^4}\ (\alpha_3^n\ Q_0) \tag{4-4}$$

Therefore, to calculate the total pressure drop of a finite number of generations, we proceed to add the respective drops of each generation

$$\Delta P_T = \frac{8\ \mu\ L_0}{\pi\ r_0^4} Q_0 + \frac{8\ \mu\ (\alpha_1\ L_0)}{\pi\ (\alpha_2\ r_0)^4} (\alpha_3\ Q_0) + \ \ldots\ + \frac{8\ \mu\ (\alpha_1^n\ L_0)}{\pi\ \alpha_2^{4n}\ r_0^4} (\alpha_3^n\ Q_0) \tag{4-5}$$

$$\Delta P_T \;=\; \frac{8\ \mu\ L_0}{\pi\ r_0^4}\ Q_0\ \left(1\ +\ \sum_{p=1}^{N} \frac{\alpha_1^p\ \alpha_3^p}{\alpha_2^{4p}}\right) \tag{4-6}$$

Solving the convergent series, for a number N of finite generations, we obtain the mathematical expression for the total pressure drop

$$\Delta P_T = \frac{8\ \mu\ L_0}{\pi\ r_0^4}\ Q_0\ \left(1\ -\ \frac{\alpha_1\alpha_3\alpha_2^{-4N}(\alpha_2^{4N}-\alpha_1^N\alpha_3^N)}{\alpha_1\alpha_3-\alpha_2^4}\right) \tag{4-7}$$

The expression in Eq. 4-7 will be referred to hereafter as the ***Homothety model***. In the analysis of lung morphology, Weibel et al. [117] described a length-diameter relationship (L/D), which after generation 3 tends to a value of 3.26. Moreover, the investigation carried out by Mauroy et al. [70] in healthy and stenotic human trachea apply this ratio with a value of 3. Let us defined a factor beta as $\beta = L/D$. Applying this definition to 4-1 we will have

$$\Delta P_0 = \frac{8\ \mu\ L_0/D_0}{\pi\ r_0^4}\ Q_0 = \frac{16\ \mu\ \beta}{\pi\ r_0^3}\ Q_0 \tag{4-8}$$

Taking the assumption that β is constant, it is possible to defined the total pressure drop as

$$\Delta P_T = \frac{16\ \mu\ \beta}{\pi\ r_0^3}\ Q_0\ \left(1\ +\ \sum_{p=1}^{N}\frac{\alpha_3^p}{\alpha_2^{3p}}\right) \tag{4-9}$$

Solving the convergent series, for a number N of finite generations, we obtain the mathematical expression for a second model as

$$\Delta P_T = \frac{16\ \mu\ \beta}{\pi\ r_0^3}\ Q_0\ \left(1\ +\ \frac{\alpha_2^{-3N}\alpha_3(\alpha_2^{3N}-\alpha_3^N)}{\alpha_2^3-\alpha_3}\right) \tag{4-10}$$

The expression in Eq. 4-10 will be referred to hereafter as the ***Beta model***. It is worth noting that Eq. 4-10 can also be obtained directly from the homothety model by forcing α_1 to be exactly equal to α_2. In fact, it is possible to define a conversion factor β^* between the two models simply as $\beta^* = (\alpha_1/\alpha_2) * \beta$.

It should be noted that these proposed models were developed only for the conduction zone in human airways, i.e. from generation 0 to generation 16 in Weibel's terminology. As explained by West [120], diffusion and gas exchange phenomena occur within the transition zone and the respiration zone (generation 17 and up), phenomena that are not considered on these models. In addition, the fractal consideration for the homothety factors definition is relevant only up to generation 16 (Mauroy et al. [70]).

Sensitivity analysis of homothety ratios

One of the main considerations in these mathematical models described previously is that the homothety and beta ratios are constant, i.e. they do not vary with the change of generation. In fact, it is this consideration that makes it possible to arrive at the final expressions of equations 4-7 and 4-10. However, a sensitivity study was developed with the intention to analyze the effect of variability of these ratios on the final pressure drop calculation. As stated above, a value of $h = 0{,}7937$ for the homothety ratios (both radius and length) represents the optimum value in terms of volume and pressure drop for a symmetrical structure. As Mauroy et al. [70] indicates, lower values of h imply high pressure drops that can cause overstress, and higher values of h lead to unnecessarily high volumes.

For the sensitivity study, the *homothety model* and the *Beta model* were evaluated with the values shown in Table 4-1. The variation interval established for the α_1 and α_2 was $\mp$0,1. As specified by Mauroy et al. [70], real lungs tend to a homothety ratio of 0.85. Therefore, this interval effectively covers these values. For β, the mean value is the 3.25 (Weibel et al. [117]) and the respective interval was defined as $\mp$1.

Data	**Units**	**Homothety Model**	**Beta Model**	**Variation intervals**
L_0	$[m]$	5.85e-2	5.85e-2	-
r_0	$[m]$	9e-3	9e-3	-
Q_0	$[m^3/s]$	1e-3	1e-3	-
α_1	$[-]$	0.79	0.79	[0.69 - 0.89]
α_2	$[-]$	0.79	0.79	[0.69 - 0.89]
α_3	$[-]$	0.5	0.5	-
β	$[-]$	3.25	3.25	[2.25 - 4.25]
μ	$[m^2/s]$	1.8204e-5	1.8204e-5	-

Table 4-1.: Model parameters for sensitivity analysis

The total pressure drop was calculated with each model a total of 10000 times, using a function to obtain random numbers within the respective intervals, to subsequently obtain the standard deviation. In Figure 4-1, the solid line shows the pressure drop obtained with constant reference values, both for the *homothety model* (a) and for the *beta model* (b), and the error bars represent the standard deviation values for each generation. These results show that the randomness of the homothety and beta ratios do not have a considerable impact on the calculation of the final pressure. With the *beta model*, slightly higher deviations are obtained, but in none of the cases the deviation in the calculations exceeds 12 %. Therefore, the consideration of non-variant coefficients is founded and functional.

4.1.2. CFD Numerical Validation

In order to validate the mathematical models described above, a set of different CFD simulations were carried out. The objective was to compare the pressure drop calculated by CFD simulations against that predicted by *Homothety model* and *Beta model*.

- **Geometries**

  Three symmetrical airway geometries were developed, each covering from generation 0 (trachea) to generation 4 (bronchioles), similar to the synthetic model used in the comparison study between airways models (see Figure 3-3 (a)). The first geometry was designed to validate the *homothety model*. The diameter and length dimensions of generation 0 come from Weibel et al. [117]. The ratios $\alpha_1 = \alpha_2 = 0{,}8$ and $\alpha_3 = 0{,}5$ were

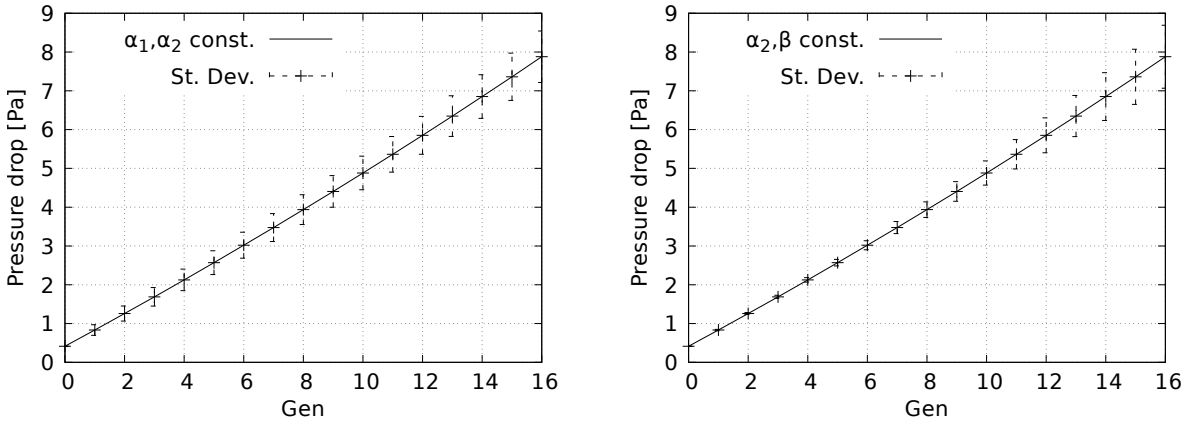

(a) Homothety Model (b) Beta Model

Figure 4-1.: Standard deviation for 0 to 16 generation tree using aleatory homothety and beta factors

chosen. The other two geometries were for analyzing the *beta model*. These geometries have the same diameter as the first model, and ratios values of $\alpha_2 = 0{,}8$ and $\alpha_3 = 0{,}5$. The difference lies in the beta factor, with $\beta = 6$ for one and $\beta = 3{,}25$ for the other. These values allow us to analyze the effect of the slenderness of the branches. All geometries are *in plane*, and the subcarinal angle was taken as 120^o, being one of the highest values reported in studies such as those carried out by Khade et al. [54] and Christou et al. [24].

A summary of the dimensions for all models can be found in Table **4-2**.

	Homothety Model		**Beta Model**			
	Geometry 1		**Geometry 2**		**Geometry 3**	
GEN	D [mm]	L [mm]	D [mm]	L [mm]	D [mm]	L [mm]
0	18	120	18	108	18	58.5
1	14.4	96	14.4	86.4	14.4	46.8
2	11.5	76.8	11.5	69	11.5	37.4
3	9.2	61.4	9.2	55.2	9.2	29.9
4	7.4	49.2	7.4	44.4	7.4	23.9

Table 4-2.: Model parameters for CFD validation

◇ **Numerical Model**

For this study, the working fluid is air. The governing equations are described in Eqs. 2-6 and 2-7. The preferred numerical configuration described in section 2.2.2 was selected. The average number of tetrahedral cells was 5e6.

◇ **Boundary condition**

For this validation study, only inhalation human process was analyzed. A symmetrical parabolic velocity profile at the inlet (i.e. trachea) was adopted. Two Re numbers were selected: 500 and 2000. At the outlets an uniform pressure boundary condition was implemented. No-slip boundary condition for the wall was applied.

◇ **Homothety and Beta models setup**

To carry out the comparative study, the *homothety model* and *beta model* were configured with the parameters observed in Table **4-3**. These values coincide with those used to develop the CFD geometries. In the Flow rate row there are two values, one for each Re number.

		Homothety Model	**Beta Model**	
	Units	**Geometry 1**	**Geometry 2**	**Geometry 3**
L_0	$[m]$	120e-3	-	-
r_0	$[m]$	9e-3	9e-3	9e-3
Q_0	$[m^3/s]$	9.57e-5 | 4.18e-4	9.57e-5 | 4.18e-4	9.57e-5 | 4.18e-4
α_1	[-]	0.8	-	-
α_2	[-]	0.8	0.8	0.8
α_3	[-]	0.5	0.5	0.5
β	[-]	-	6	3.25
μ	$[m^2/s]$	1.8204e-5	1.8204e-5	1.8204e-5
N	[-]	5	5	5

Table 4-3.: Parameters for *Homothety* and *Beta* models

◇ **Results**

Results comparison for the pressure drops obtained by the CFD model vs the calculated are shown in Figure **4-2** for *homothety model*, Figure **4-3** for *beta model* with $\beta = 6$ and Figure **4-4** for *beta model* with $\beta = 3{,}25$. The curves were taken across the axial axis of each branch.

As can be seen in all comparisons, each bifurcation point generates a pressure peak. As expected, these peaks decrease as one progresses through the airway generations. It is precisely these zones of high pressure gradients that affect the prediction made from the models proposed in this research, i.e., models based on the Hagen-Poiseuille equation.

The pressure drop curves calculated with our *homothety model* and *beta model*, i.e. the dashed lines in Figures **4-2**, **4-3**, and **4-4**, correctly match the curves obtained from the

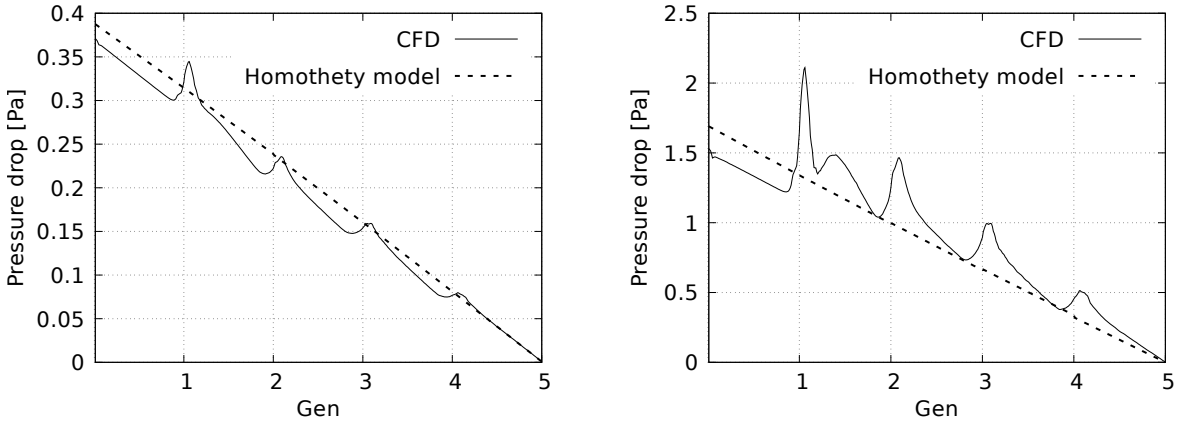

(a) Re = 500 (b) Re = 2000

Figure 4-2.: Pressure drop comparison for *Homothety model*

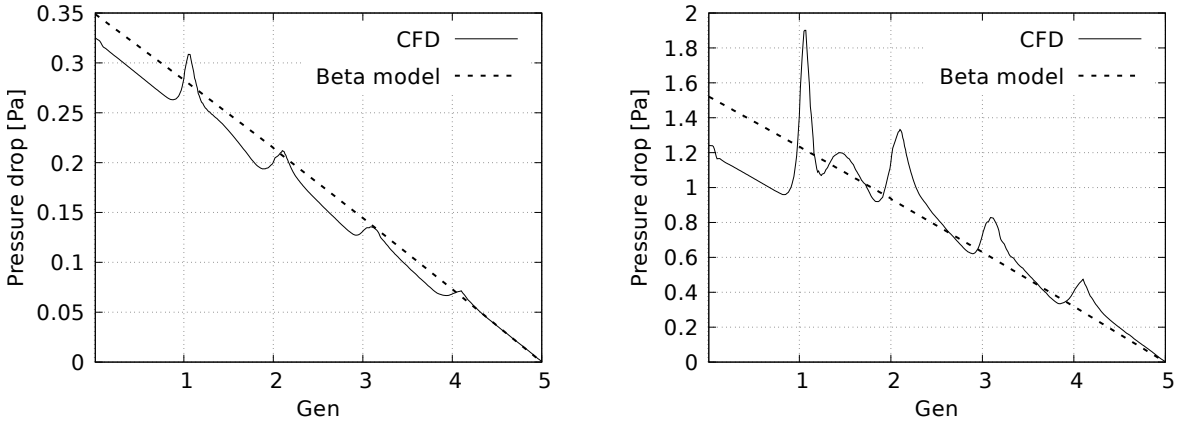

(a) Re = 500 (b) Re = 2000

Figure 4-3.: Pressure drop comparison for *Beta model* with $\beta = 6$

CFD simulation. Although the pressure peaks are not predicted, the stabilization of the pressure towards a linear drop, evidenced after each peak, is very well approximated by the models. As is well known, the Hagen-Poiseuille equations are applicable for flows in pipes of constant cross section, with a length that allows the flow to develop, and for regimes within the laminar zone. Indeed, for the cases with Re 500, the results of the pressure calculated against those obtained by CFD were more accurate than those obtained for Re 2000, since at this Reynolds number there are pressure peaks of greater magnitude at each bifurcation. Also, as the branches are less slender, the pressure calculation is less accurate. For $\beta = 6$ good approximations with both Re were obtained. For $\beta = 3{,}25$ there is a good fit with Re 500, but for the case of Re 2000 the calculated drops were not accurate in the first generations, as illustrated in Figure 4-4 (b). However, after a few generations, the calculated value tends to the values obtained

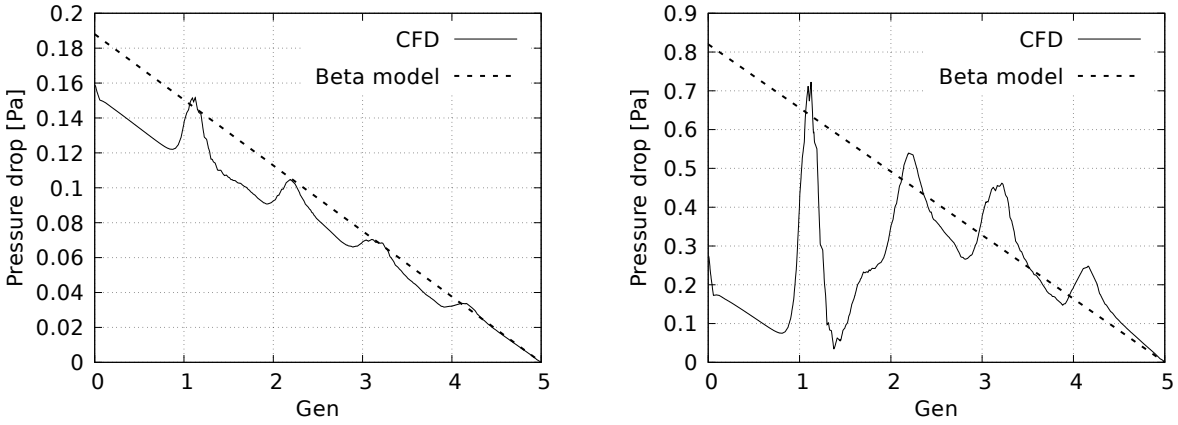

(a) Re = 500 (b) Re = 2000

Figure 4-4.: Pressure drop comparison for *Beta model* with $\beta = 3{,}25$

from CFD.

4.1.3. Algorithm implementation as a OpenFOAM boundary condition

Some investigations such as those developed by Olufsen [82], Ismail et al. [48], De Backer et al. [29] and Yoshihara et al. [125] show how from mathematical models, equations of state and analogies to other systems (electrical, pneumatic, etc.) some boundary conditions can be developed. Considering that the models proposed in this research can calculate the pressure of a tree of N generations, it is possible to develop a pressure boundary condition. A hybrid simulation methodology were explored based on a dimensional reduction (3D to 0d). For this methodology, two pressure boundary conditions, *pressureHomothetyAirwaysModel* and *pressureBetaAirwaysModel*, were implemented and validated using the open source OpenFOAM. The respective *class definition* .C and *Header* .H (the required files for compilation in this open source) are attached in A.1 (*homothety model*) and A.2 (*Beta model*). With the aim of simplify the writing, the contraction ***OF-BC*** to refer to the programmed boundary is applied hereafter.

i **OF-BC workflow**

Figure **4-5** shows the workflow of the boundary condition. This diagram applies to both models, since the difference between them lies only in the input data and in the math to calculate the *P factor*, which simply refers to Equations 4-7 and 4-10 without the viscosity and flow rate terms, since these are set in subsequent steps.

The described algorithm has a routine to calculate the patch area (Patch Area calculation), and from this result, calculate the radius. The advantage of this step within the algorithm is that regardless of the geometry of the patch, it calculates a characteristic

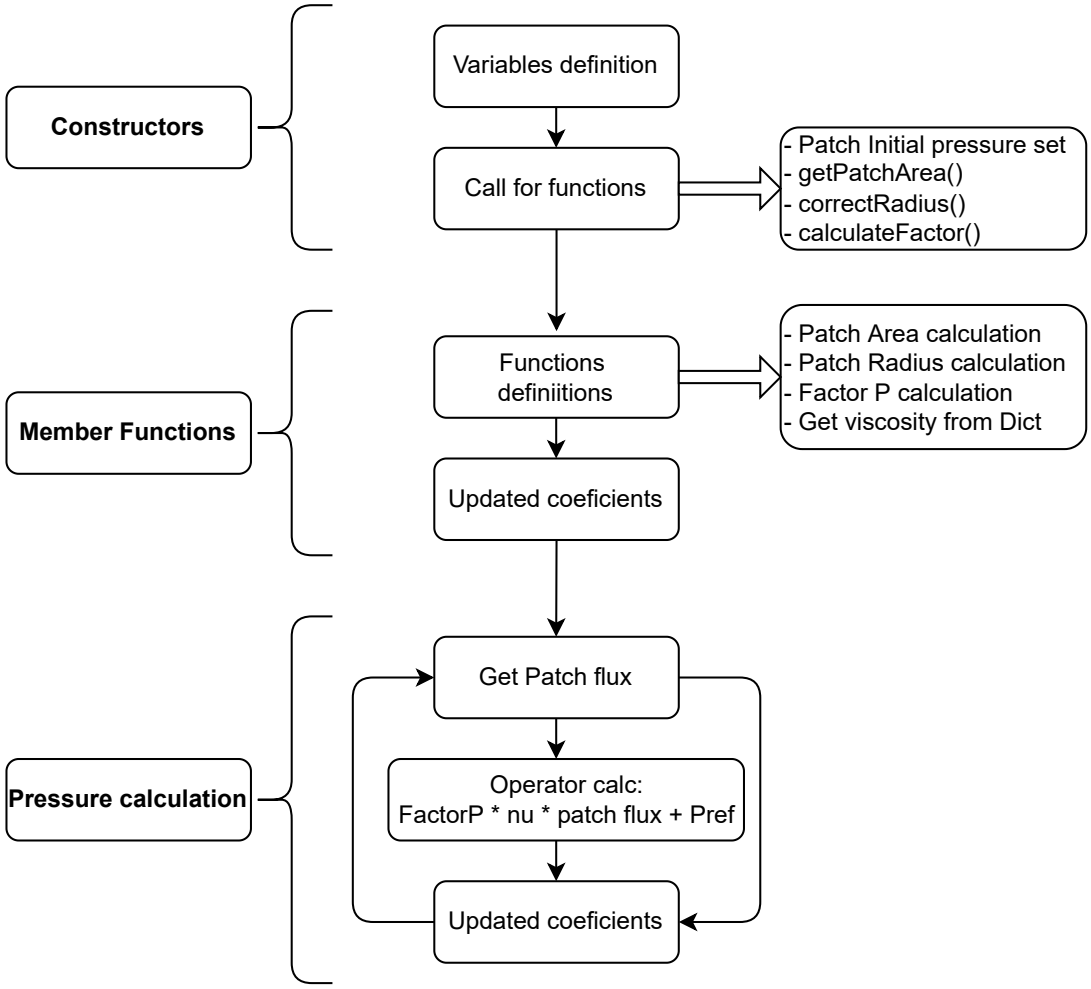

Figure 4-5.: OF-BC workflow

radius, ideal for real patient-specific airways, where the geometry of the outlets is not a perfect circumference.

ii **OF-BC Dictionary**

The OF-BC specification must be developed within the P dictionary in the initial conditions folder. The definition of the parameters for each model is as follows:

- *Homothety model* input variables:

```
Patch Name
    {
        type            pressureHomothetyAirwaysModel;
        U               U;
```

```
        phi             phi;
        rho             none;
        L0              0.1;
        alpha1          0.8;
        alpha2          0.8;
        alpha3          0.5;
        N               15;
        pRef            uniform 0;
    }
```

- *Beta model* input variables:

```
Patch Name
    {
        type            pressureBetaAirwaysModel;
        U               U;
        phi             phi;
        rho             none;
        beta            6;
        alpha2          0.8;
        alpha3          0.5;
        N               15;
        pRef            uniform 0;
    }
```

iii OF-BC numerical validation

Geometries 1 and 2 (see Table 4-2) were selected for the CFD validation, with the difference that for this case only the first two generations were modeled (trachea and main bronchi), as shown in Figure 4-6. The three missing generations were approximated by the OF-BC.

The simulation setup was basically the same as the CFD Numerical validation section, with the only two differences:

- Geometries were reduced from 5 to 2 generations involving a change in the cells number from 5e6 to 1.5e6.
- Pressure condition at outlets were changed from fixedValue to the respective OF-BC.

Both *pressureHomothetyAirwaysModel* and *pressureBetaAirwaysModel* were set up with the values given in Table 4-3, except for the number of generations N, which for this case is 3.

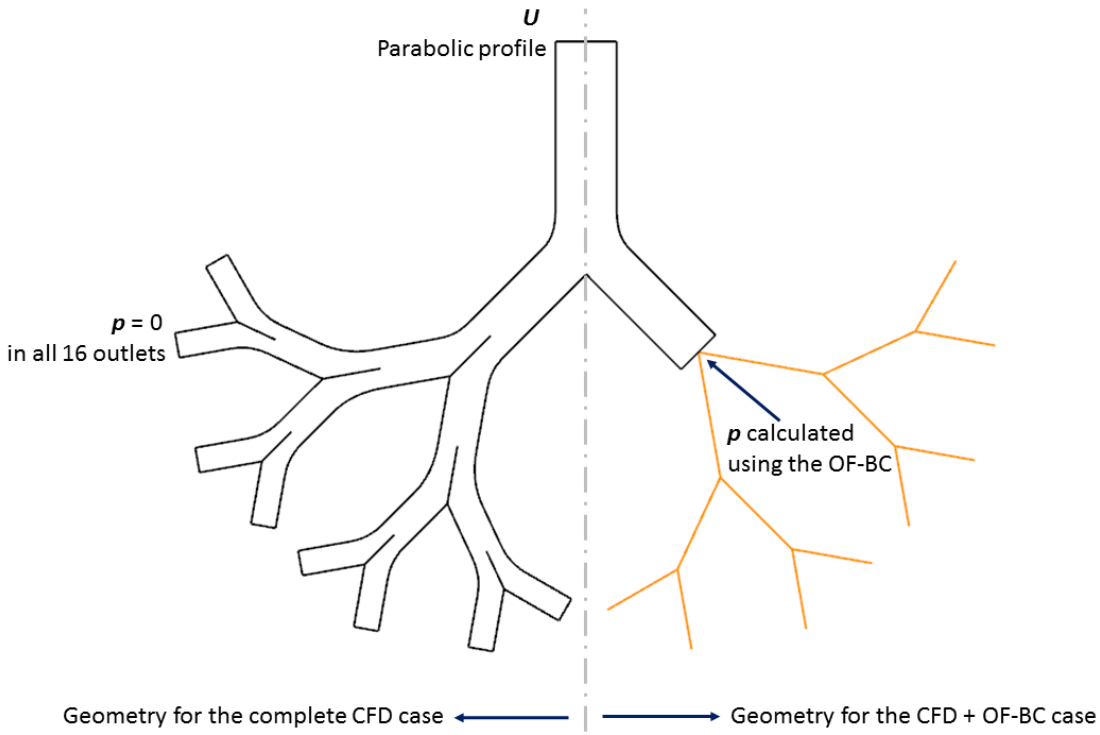

Figure 4-6.: Models used in CFD validation

The results for the pressure drops ΔP versus generation number can be seen in Figure **4-7** and Figure **4-8**. Again these curves were taken along the axial axis from the start of the geometry to the end of generation 1. These graphics show the numerical results for the complete CFD model (continuous line), the pressure calculation obtained from Equations 4-7 and 4-10 (dashed line), and finally, the curve obtained with the hybrid simulation combining CFD plus the OF-BC (faded line).

As expected, the dashed and faded lines almost intersect at the end of generation 1 (right border in the 6 graphs), indicating that the OF-BC is correctly calculating the pressure values that Equations 4-7 and 4-10 predicted. The values are not exactly the same due to the mathematical model is evaluating an exact value of radius, meanwhile the OF-BC is using an approximate calculated value, as explained above. To evaluate the accuracy of the results, a relative error was calculated as

$$e\,[\%] = \frac{|V_{CFD} - V_{HYB}|}{V_{CFD}} \text{ x } 100 \tag{4-11}$$

where V_{CFD} is the value obtained from the complete CFD simulation and V_{HYB} is the result obtained from the hybrid simulation (CFD + OF−BC). From the OF-BC application, higher pressure values were obtained compared to the results of the

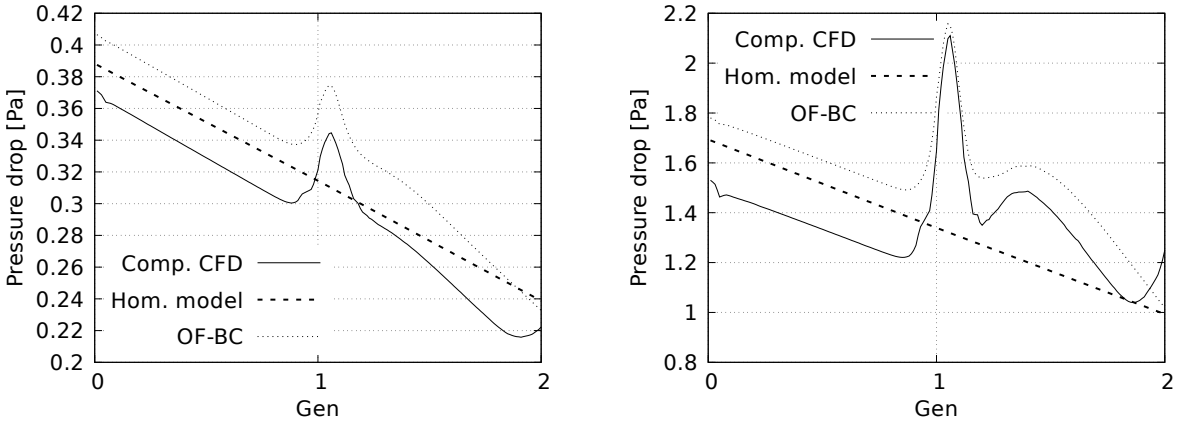

(a) Re = 500 (b) Re = 2000

Figure 4-7.: Pressure drop comparison for *Homothety model*

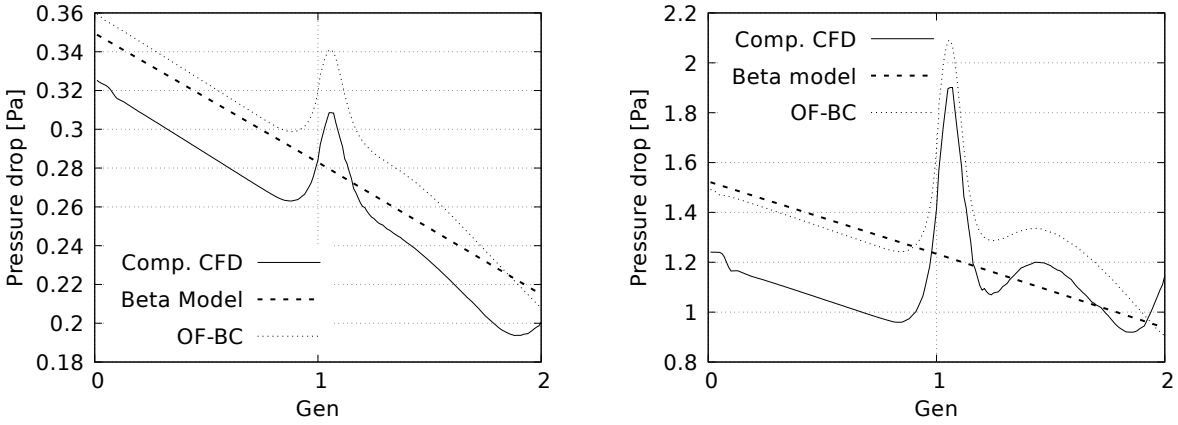

(a) Re = 500 (b) Re = 2000

Figure 4-8.: Pressure drop comparison for *Beta model* with $\beta = 6$

complete CFD simulation. While in the complete CFD simulation the pressure in generation 1 ends up influenced by the pressure gradients, in the hybrid simulation this value is precisely the one calculated with the homotetic or beta model. However, these differences are not excessive. For the *homothety model* (Figure **4-7**) and the *beta model* with $\beta = 6$ (Figure **4-8**), the errors do not exceed 11 % for Re 500 and 19 % for Re 2000.

Velocity profiles are shown in Figure **4-9** and Figure **4-10**, these were taken in the middle of the branch belong to a generation 1, on the coronal plane.

As has already been analyzed in other studies (Liu et al. [63], Martonen et al. [69], Zhao and Lieber [128]), when the flow passes through the bifurcation, a deformation tendency of the velocity profiles is generated towards the internal face, an effect that,

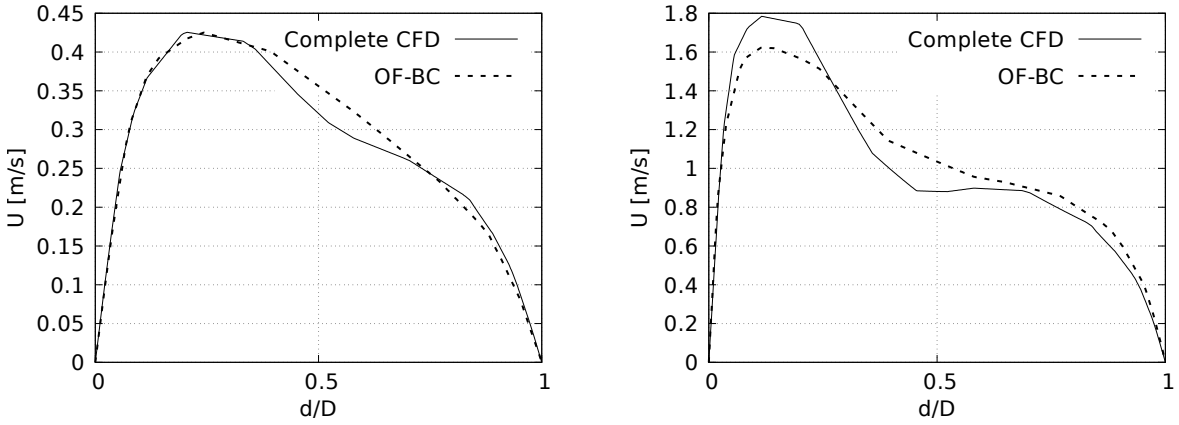

(a) Re = 500 (b) Re = 2000

Figure 4-9.: Velocity profile comparison for *Homothety model*

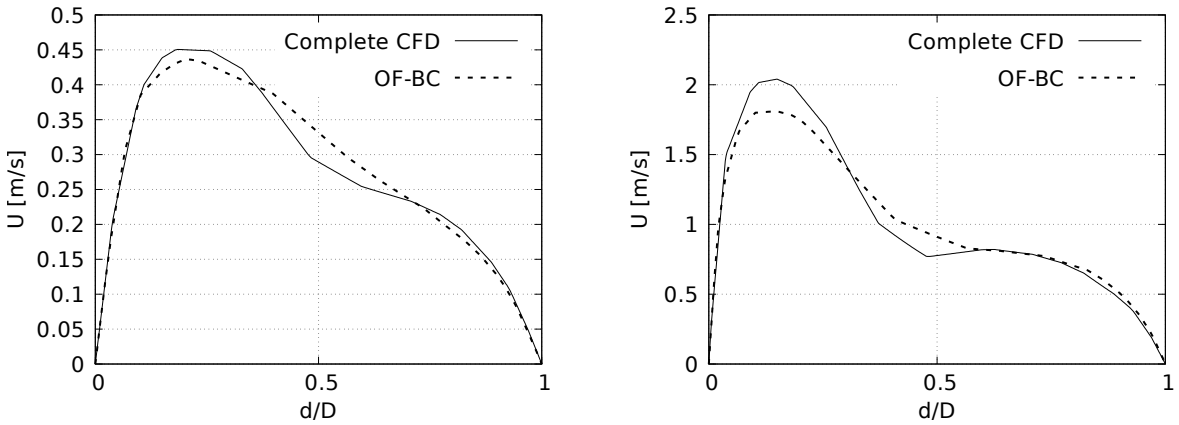

(a) Re = 500 (b) Re = 2000

Figure 4-10.: Velocity profile comparison for *Beta model*

as can be seen in Figure **4-9** (b) and Figure **4-10** (b), is stronger for larger Reynolds numbers.

Both the full CFD simulation and OF-BC capture this phenomenon, with the difference that the OF-BC calculates a lower velocity value. However, as with the pressure curves, there is not a remarkable difference between the peak values. In this case, there is an underestimation of the velocity, with relative errors around 11 % for the larger Re numbers (Figure **4-9** (b) and Figure **4-10** (b)), and 4 % for the smaller ones (Figure **4-9** (a) and Figure **4-10** (a)).

Studies such as those carried out by Xia et al. [123] show how the maximum shear stresses (WSS) are located near to the bifurcation points. To analyze this point, WSS was measured along the inner wall of one branch belong to generation 1, taken from

the bifurcation point of the first generation (i.e., the carina) to the bifurcation point of the second generation.

Figure 4-11 and Figure 4-12 shown the measured WSS vs x/L normalized distance. In line with the analysis of the velocity profiles, the WSS also have an underestimate calculated by the OF-BC. It is evident how the continuous line and the dashed lines overlap along the trajectory and move away from each other near the bifurcation points, i.e. at the beginning and end of the plotted curves. These differences between the WSS values are more noticeable for the low Re numbers, where we have errors of up to 15 % between the peak values.

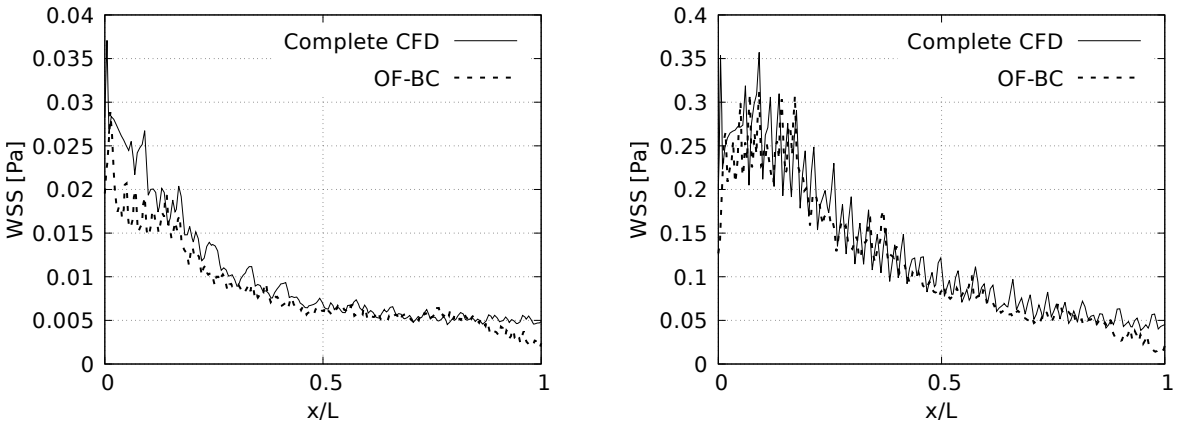

(a) Re = 500 (b) Re = 2000

Figure 4-11.: Wall shear stress comparison for *Homothety model*

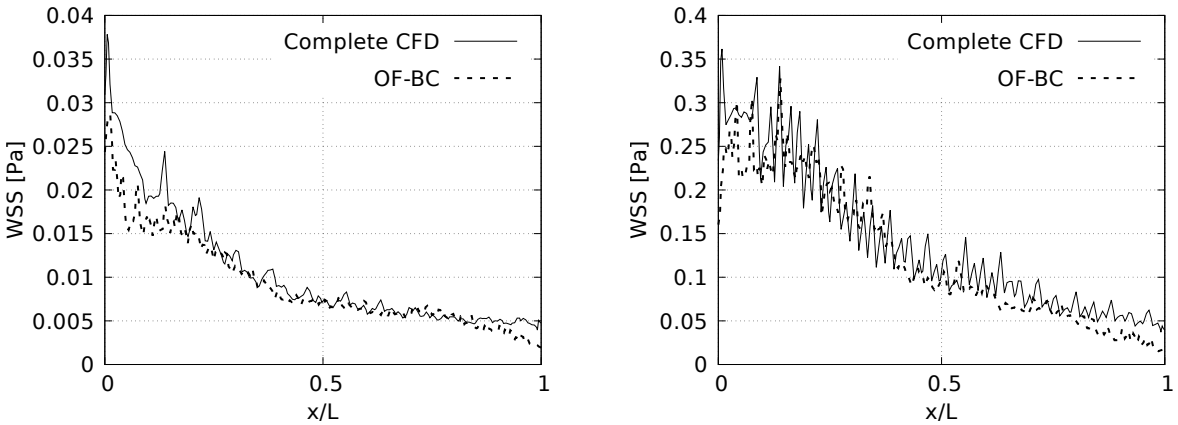

(a) Re = 500 (b) Re = 2000

Figure 4-12.: Wall shear stress comparison for *Beta model*

4.1.4. Computational cost analysis

An important feature to analyze is the computational cost simulation in both complete CFD simulation and OF-BC application. All simulations ran for a total of 0.5 seconds. This time ensure the full fluid development (for both Re 500 and Re 2000). A summary of the simulation times spent in each case is shown in the Table **4-4**. The percentage of improvement was calculated using the same formula as in Eq. 4-11, where V_{CFD} is the time spent in the complete CFD simulation and V_{HYB} is the time spent in the hybrid simulation (CFD + OF−BC). As can be seen, the savings in simulation time derived from the use of OF-BC is remarkable. Clearly the improvement in computational cost starts with having a shorter 3D model. This achievement allows a considerable reduction in the number of cells in the computational domains. While models with 5 million cells were used for the complete CFD simulations, this was reduced to 1.5 cells with the OF-BC by eliminating the three corresponding generations. Another important aspect is the simplicity of the programmed boundary conditions. As they are simple mathematical models, they do not require high computational resources to be calculated at each time step.

	Homothety model			**Beta model**		
	Meshing	**Re 500**	**Re 2000**	**Meshing**	**Re 500**	**Re 2000**
Full CFD simulation	0.34 h	2.6 h	19.8 h	0.3 h	2.2 h	19 h
CFD + OF-BC	0.13 h	0.8 h	7 h	0.12 h	0.7 h	6.7 h
Improvement	61.7 %	69.2 %	64.6 %	60 %	68.2 %	64.7 %

Table 4-4.: Computational cost analysis

4.2. Application cases

In order to test the capability of the developed boundary conditions, two application cases were developed: an analysis of airways in asthma condition using a synthetic model, and a study on airway collapse using a real patient-specific model.

4.2.1. CASE I: Asthmatic human airways

As described in the background, the condition of asthma is reflected in a contraction of the airways, reducing the cross section of the branches. In the study realized by Tsega and Katiyar [111], a comparative analysis of airflow behavior across airways in healthy and asthmatic condition is performed using separate geometries covering two different zones: from generation 3 to 7 (first zone) and from generation 10 to 14 (second zone). Off-plane models were implemented in Tsega and Katiyar [111] study. The particularity of these models is that they present angles between the branches in both coronal and sagittal planes.

The mean objective of this first application case was to compare the behavior of the pressure drop calculated with the application of the OF-BC against the results obtained by Tsega and Katiyar [111], and to expand the results to more generations than those already simulated.

◇ **Geometry**

Two geometries were modeled: a healthy and an asthmatic models covering the third and four generation. Mean dimensions can be seen in Table **1-2**. The subcarinal angle is 70^o. These dimensions are exactly the same as those implemented in the Tsega and Katiyar [111] study.

◇ **Numerical Model**

For this study, the working fluid is air. The governing equations are described in Eqs. 2-6 and 2-7. The preferred numerical configuration described in section 2.2.2 was selected. The average number of tetrahedral cells was 1e6.

◇ **Boundary conditions**

An uniform velocity profile was established at the inlet, corresponding to a volumetric flow of 15 L/min, covering the laminar regimen with Re 484 (healthy) and Re 1089 (asthmatic). No-slip boundary condition for the wall was applied. For the outlets, the OF-BC was set up, selecting for this application the *pressureBetaAirwaysModel*. Using the dimensions of the table, ratios $alpha_2$ and *beta* were calculated. Figure **4-13** and Figure **4-14** show these factors from generation 5 to 16 for healthy and asthmatic cases, respectively. For the two cases of analysis, the following settings were configured:

1. For results validation with those obtained by Tsega and Katiyar [111], an α_2 and β average between generation 5,6 and 7 was required. The continuous line in Figure **4-13** and Figure **4-14** show this average: for the healthy model $\alpha_2 = 0{,}80$ and $\beta = 3{,}2$ and for the asthmatic $\alpha_2 = 0{,}79$ and $\beta = 7{,}4$.
2. For the extended analysis, considering all generations of the conducting zone, an average from generation 5 to 16 was calculated. The dashed line in Figure **4-13** and Figure **4-14** shows this average: for the healthy model $\alpha_2 = 0{,}85$ and $\beta = 3{,}3$ and for the asthmatic $\alpha_2 = 0{,}83$ and $\beta = 8$.

◇ **Results**

Figure **4-15** shows a comparison between the pressure distributions on the wall obtained by Tsega and Katiyar [111] ((a) and (c)) vs the results obtained by applying the OF-BC ((b) and (d)). It is noted that OF-BC is correctly capturing the pressure drops distributions, including the high values that develop at the bifurcation point and in

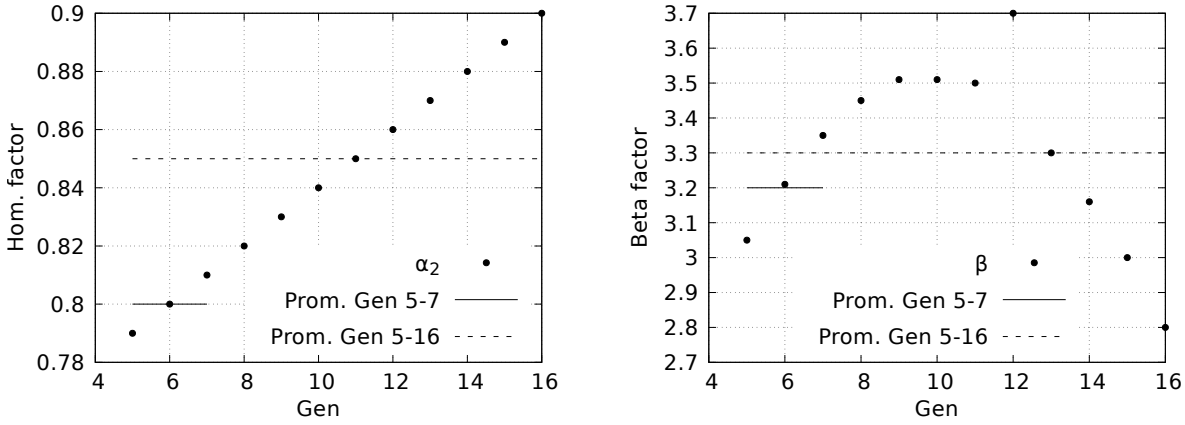

(a) α_2 Factor (b) β Factor

Figure 4-13.: Homothety and beta factor for healthy airways

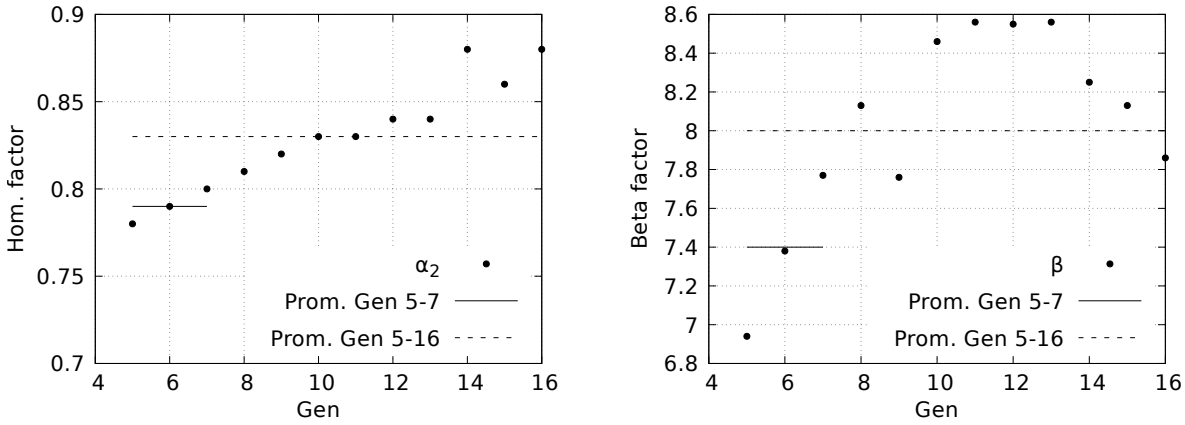

(a) α_2 Factor (b) β Factor

Figure 4-14.: Homothety and beta factor for asthmatic airways

the inlet. Regarding to the maximum pressure, a peak of 3,92 $[Pa]$ for the healthy case and 91,3 $[Pa]$ for the asthmatic case were reported by Tsega and Katiyar [111]. With the use of the OF-BC, values of 3,40 $[Pa]$ and 96,08 $[Pa]$ were obtained. These results reflect what was discussed in the validation of the models: For slender branches ($\beta = 7$ in the asthmatic case) and low Re (1089), the pressure calculation is very accurate, since the relative error between the maximum peak obtained by Tsega and Katiyar [111] and the one calculated by our simulation is only 5 %. On the other hand, for not so slender branches ($beta = 3{,}2$) and low Re (484), accurate results are still obtained, with a relative error of 13.3 %.

Once the results were compared with the 5-generation geometry of Tsega and Katiyar [111], the extended study of the behavior of healthy versus asthmatic airways covering the respiratory conduction zone, from generation 3 to generation 16, was performed.

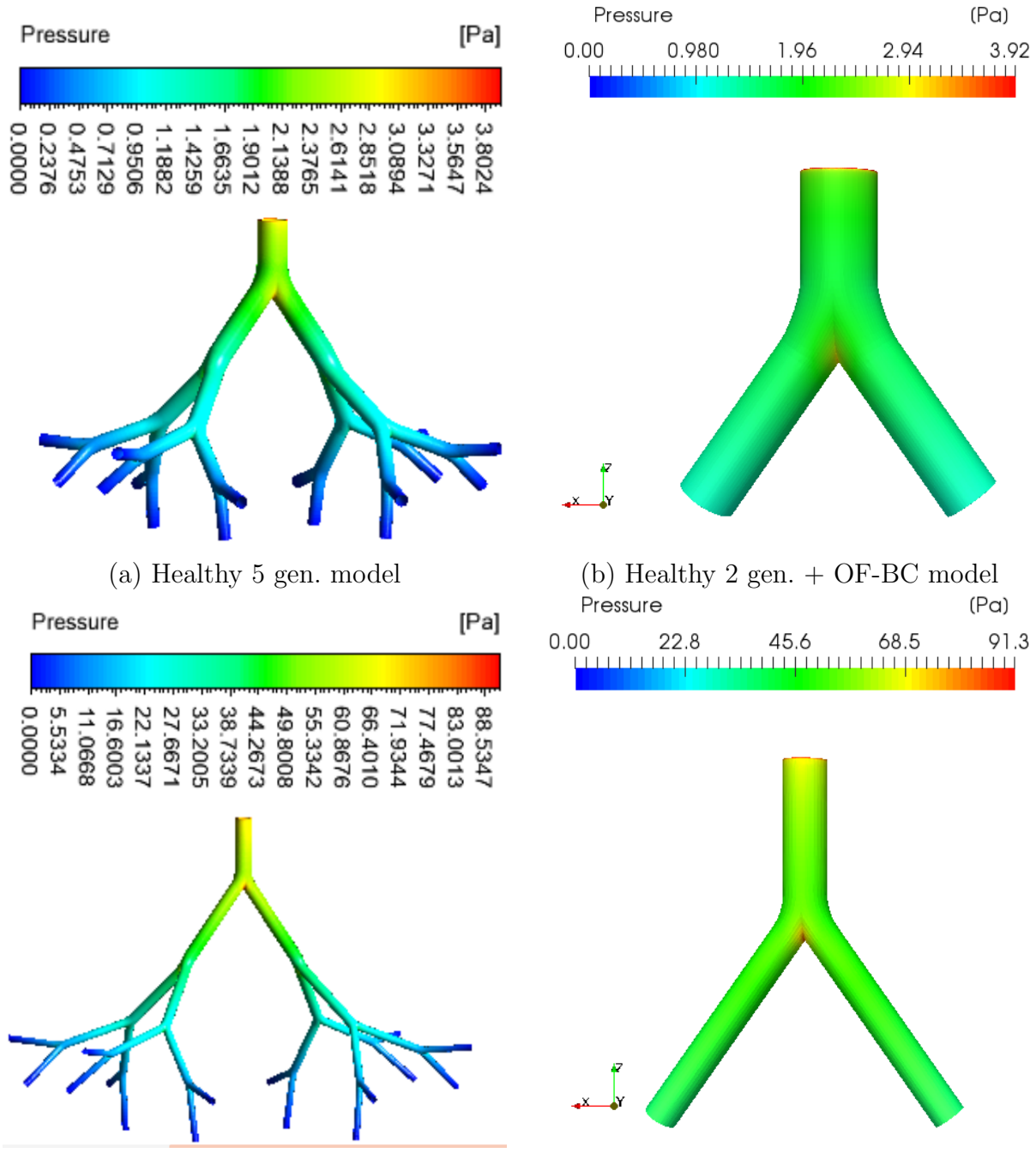

(a) Healthy 5 gen. model

(b) Healthy 2 gen. + OF-BC model

(c) Asthmatic 5 gen. model

(d) Asthmatic 2 gen. + OF-BC model

Figure 4-15.: Wall pressure distribution. Items (a) and (c) taken from Tsega and Katiyar [111]

Figure **4-16** shows the comparison between pressure drops,velocity profiles and wall shear stresses. Two vertical axes were used in these plots: a green axis for the healthy condition on the left side, and a blue axis for the asthmatic condition on the right side,

each with its own scale.

Figure 4-16 (a) shows the pressure drop measured across the axial axis of the branches from generation 0 to 1. As expected, the pressure peak due to the gradients is observed. The large difference in scales for each axis evidences the effect of the airway narrowing, increasing the inlet pressure from 2,8 $[Pa]$ to 96 $[Pa]$. The maximum pressure values developed in each case were 6,66 $[Pa]$ and 128,6 $[Pa]$, for the healthy and the asthmatic condition, respectively.

The velocity profiles can be seen in Figure 4-16 (b). These curves were taken on the coronal plane, in the middle of a branch belonging to generation 1. The remarkable velocity increase due to cross-sectional contraction from the healthy to the asthmatic case is evidenced, with a peak growing from 1,54 $[m/s]$ to 7,5 $[m/s]$.

Figure 4-16 (c) illustrates the wall shear stresses measured on the inner wall of a branch of generation 1. In line with the results obtained for velocity, a significant increase in shear stresses is visualized for asthmatic airways, specially in the vicinity of the bifurcation point where a maximum value of 2,7 $[Pa]$ is reached, in contrast to the stress value of 0,19 $[Pa]$ developed by healthy airways.

4.2.2. CASE II: Patient-specific analysis

The main objective of this application was to show how the boundary condition based on homothety ratios can be applied in real airway models.

- **Geometry**

  The same real specific patient model segmented in the *Comparative study between synthetic and real airway models* was selected for this analysis (See Figure 3-1 and 3-2). Figure 4-17 shows the post-processed model with the respective branch names that will be used in this study.

- **Numerical model**

  For this study, the working fluid is air. The governing equations are described in Eqs. 2-6 and 2-7. The preferred numerical configuration described in section 2.2.2 was selected, with the only difference that the *pimpleFoam* solver is applied. The average number of tetrahedral cells was 4e6.

- **Boundary conditions**

  Total conducting respiratory zone were performed. The computational CFD domain cover from trachea (Gen 0) to secondary bronchi (Gen 4), and with the OF-BC the respective missing generations were modeled. Two healthy and collapsed airway cases were explored following the next set up:

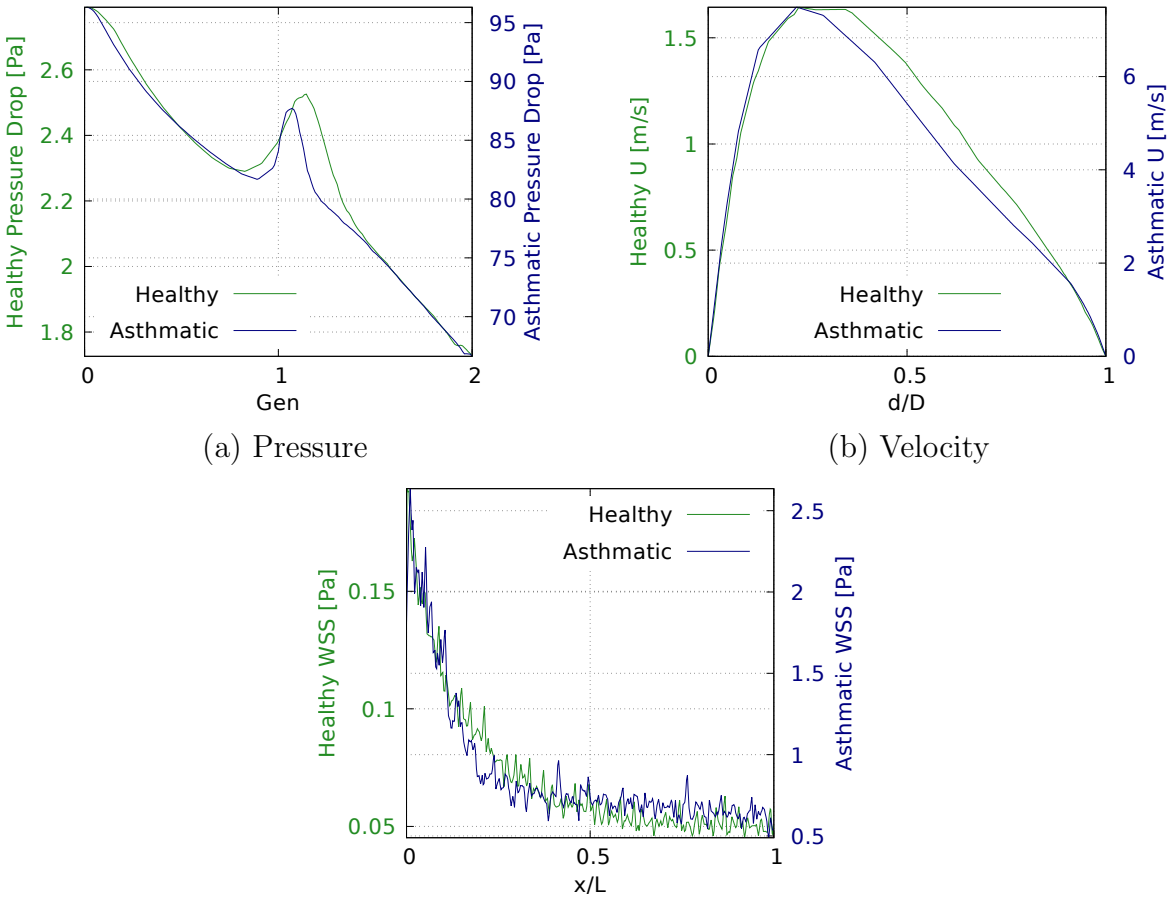

(a) Pressure

(b) Velocity

(c) WSS

Figure 4-16.: Healthy and asthmatic airways comparison

- For healthy case, all outlets cover up to generation 16, with a factor $\alpha_2 = 0{,}8$ and $\beta = 3{,}25$.
- For the collapsed airways case, the outlets deriving from the Left main bronchi cover up to generation 16 with $\alpha_2 = 0{,}8$ and $\beta = 3{,}25$. On the other hand, the outlets deriving from the Right main bronchi cover only one more generation with $\alpha_2 = 0{,}8$ and $\beta = 3{,}25$.

The *pressureBetaAirwaysModel* condition was selected to configured these cases. For the volumetric flow a factor of $\alpha_3 = 0{,}5$ is considered.

The area of the inlet patch was 2.6e-4. Although this patch does not have an exact geometric shape, a circle approximation was assumed to determine the diameter. With this value, two Re numbers of 500 and 1600 were calculated and performed. A non-slip condition in the walls was applied.

- **Results**

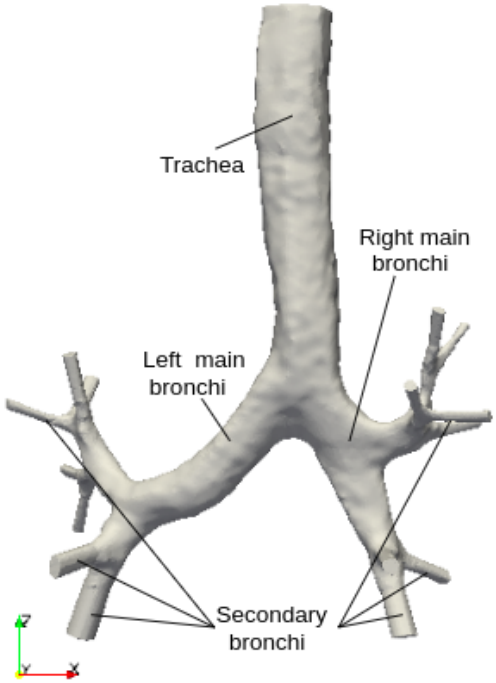

Figure 4-17.: Real specific-patient airways model

Figure 4-18 shows the comparison of the velocity streamlines for Re 500. For the healthy conditions, a relatively uniform streamlines distribution in both right and left sides is noticeable, with a maximum velocity peak of 1,025 $[m/s]$, located in the last CFD generation modeled deriving from the Left main bronchi. On the other hand, in the collapsed airways simulation, it can be observed a velocity increase towards the branches deriving from the left main bronchi, reaching a peak of $1,254$ $[m/s]$. In a similar way, for a Re 1600, a peak of $3,423$ $[m/s]$ is obtained for the healthy condition and it increases to $3,951$ $[m/s]$ in the collapsed case. These velocity changes imply a percentage increase of 22 % for Re 500 and 15 % for Re 1600.

Wall pressure distribution for Re 1600 are shown in Figure 4-19. In healthy airways, a maximum pressure peak of 24,39 $[Pa]$ is generated. In turn, the minimum pressure value of 11,39 $[Pa]$ is located in the terminal branches. As expected, in the case of collapsed airways, a decrease in pressure is evidenced due to the missing generations. A maximum value of 19,27 $[Pa]$ and a minimum of 4 $[Pa]$ is observed. This implies a decrease of approximately 20 % for the maximum pressure peak, and a reduction of more than 50 % in the minimum pressure values reached. Accordingly, for Re 500 a decrease of the minimum pressure of the same percentage is evidenced, going from 3,15 $[Pa]$ to 1,59 $[Pa]$.

Figure 4-20 illustrates the wall shear stresses for Re 1600. A scale from 0 $[Pa]$ to

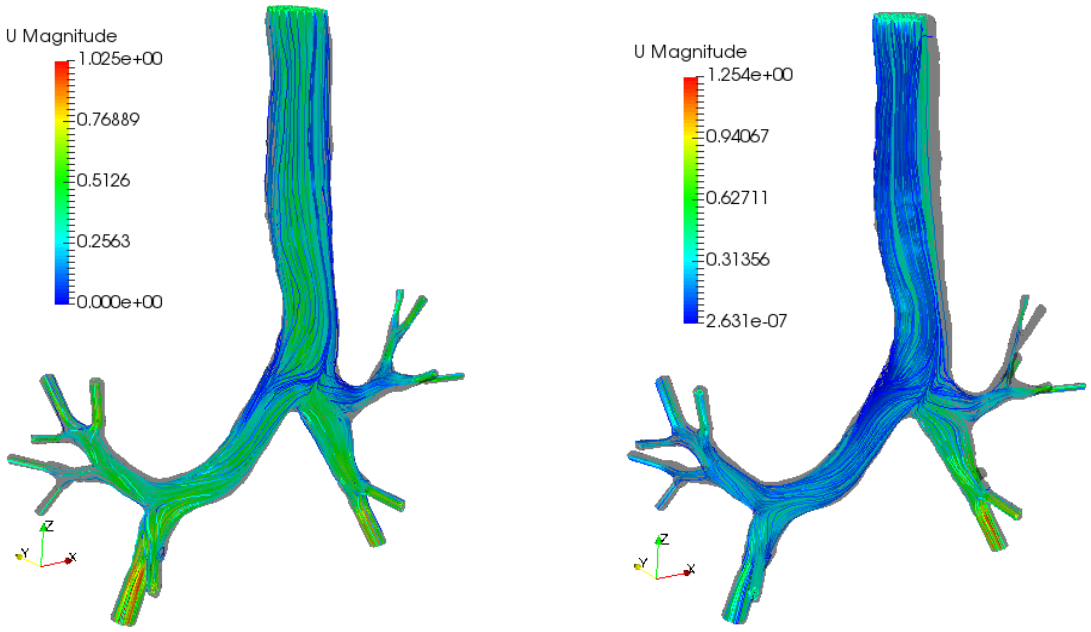

(a) Healthy airway (b) Collapse airway

Figure 4-18.: Velocity streamlines for Re=500

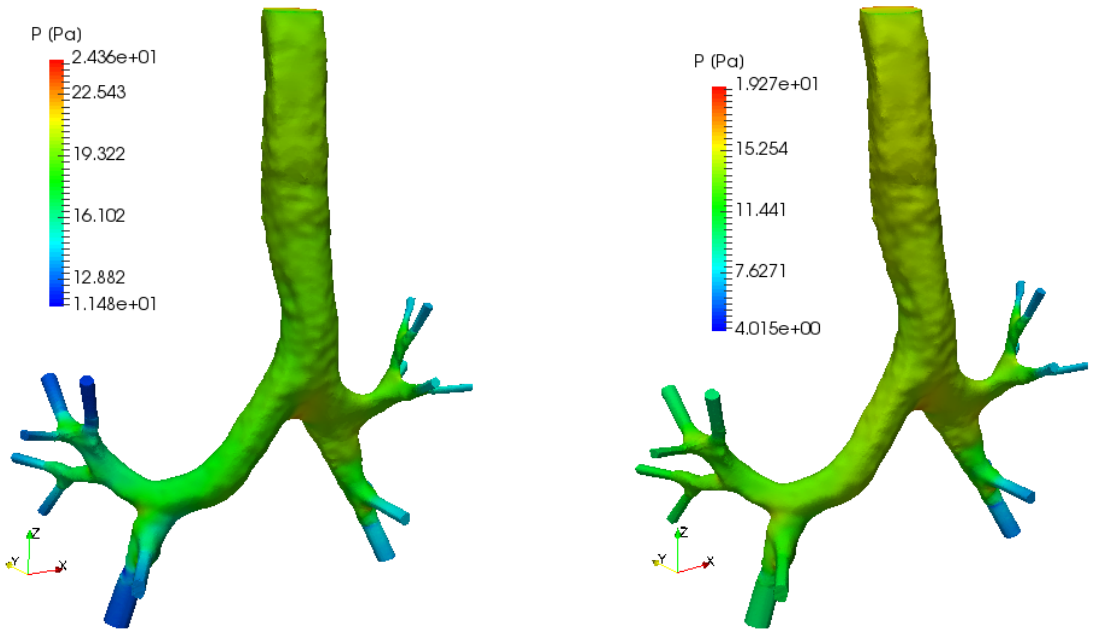

(a) Healthy airway (b) Collapse airway

Figure 4-19.: Pressure wall distribution for Re=1600

0,3 $[Pa]$ was applied for both plots, in order to clearly observe the behavior of the WSS. It is remarkable how the stresses increase and redistribute towards the branches

derived from the Left main bronchi when the collapse occurs, generating overstresses in all the bifurcation points on these branches. This re-distribution of the WSS is in line with the streamline patterns, evidencing how the zone affected by the loss of generations impacts the flow behavior through the airways. A maximum stress of 0,89 $[Pa]$ is developed in the collapse case, value which represents an increase of 33 % compared to the 0,67 $[Pa]$ generated in the healthy case. A percentage increase of 15 % is observed for Re 500.

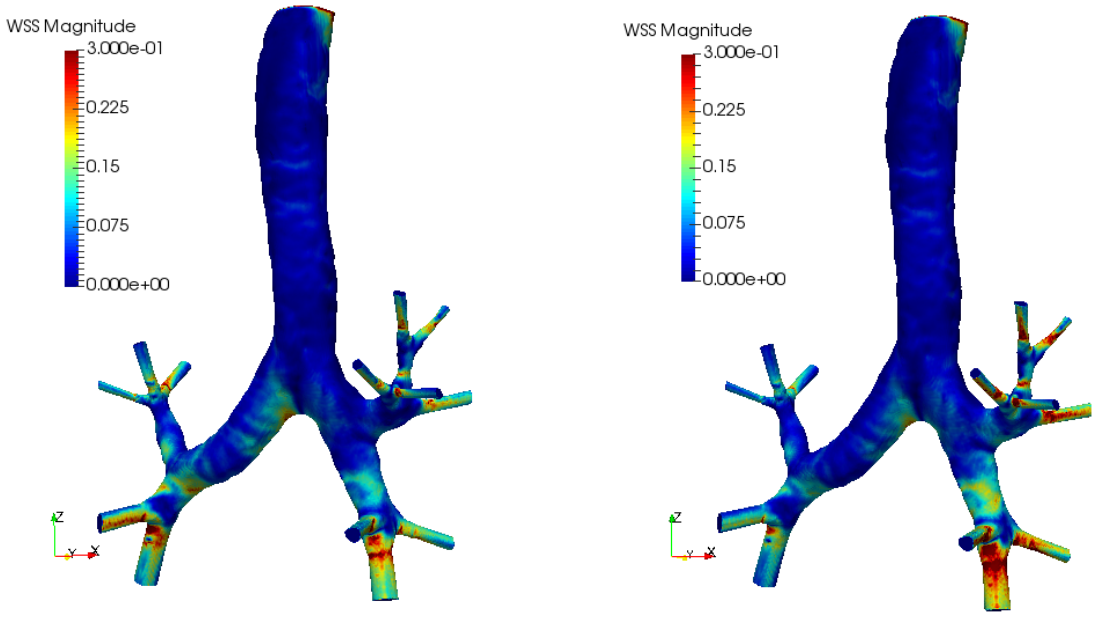

(a) Healthy airway (b) Collapse airway

Figure 4-20.: Wall shear stresses for Re=1600

4.3. Algorithm performance for pulsating flows

Flow through the airways has an essentially pulsatile behavior. As indicated in research work by Xia et al. [123], Adler and Brücker [1] and Bauer and Brücker [8], fluid oscillation is generally simplified as a sinusoidal function. This implies that, for example, for the beta model equation is defined as

$$\Delta P_T(t) = \frac{16\ \mu\ \beta}{\pi\ r_0^3}\ Q_0(t)\ \left(1 + \frac{\alpha_2^{-3N}\alpha_3(\alpha_2^{3N} - \alpha_3^N)}{\alpha_2^3 - \alpha_3}\right) \tag{4-12}$$

Some experiments to analyze the behavior of the boundary condition with the Beta model for pulsating flows were developed. They are described below.

◇ **Geometry**

Two airways geometries with the configuration shown in Figure 4-6 were employed: The first is the 5-generation geometry used to validate the beta model (see Figure 3-3 and *Geometry 2* column in Table 4-2), and the second is a 2-generation geometry coming from the elimination of the last three generations of the previous model.

◇ **Numerical model**

For this study, the working fluid is air. The governing equations are described in Eqs. 2-6 and 2-7. For this case two differences with the preferred numerical configuration described in section 2.2.2 were implemented: the selection of pimple foam as solver and the change of the temporal scheme to Crank-Nicholson. These changes are due to select better performance schemes for oscillating flows. The average number of tetrahedral cells was 1.5e6.

◇ **Boundary conditions**

An uniform oscillating sinusoidal velocity was applied at the inlet for both geometries. A peak velocity equivalent to Re=500 was selected, and two different frequencies were analyzed:

1. Wo = 4.14 equivalent to a frequency close to conventional mechanical ventilation (CMV) with 30 breath cycles per minute.
2. Wo = 8.29 equivalent to high frequency oscillatory ventilation (HFOV) with 120 breath cycles per minute.

Two breathing cycles were performed, implying a total simulation time of 4 seconds for Wo = 4.14 and 1 second for Wo = 8.29.

A non-slip condition in the walls was applied.

For the pressure setting, in the case of the full 5-generation geometry a fixed pressure of 0 was imposed. On the other hand, for the case of the 2-generation cut geometry the Beta boundary condition was set using the values observed in *Geometry 2* column in the Table 4-3.

4.3.1. Pressure and velocity curves analysis

For the analysis results, two probes were placed in the airways tree, one in the middle of the trachea and the other in the middle of a branch of generation 1. A comparison of the pressures over time using the complete CDF simulation vs OF-BC is shown in Figures 4-21 and 4-22 for $Wo = 8{,}29$ and $Wo = 4{,}14$, respectively.
As is evident in both cases, although the trends are well captured, the pressure values over time obtained with the OF-BC are smaller in magnitude. This difference is more noticeable for the larger Wo number. With Hagen-Poiseuille's law it is possible to calculate the value

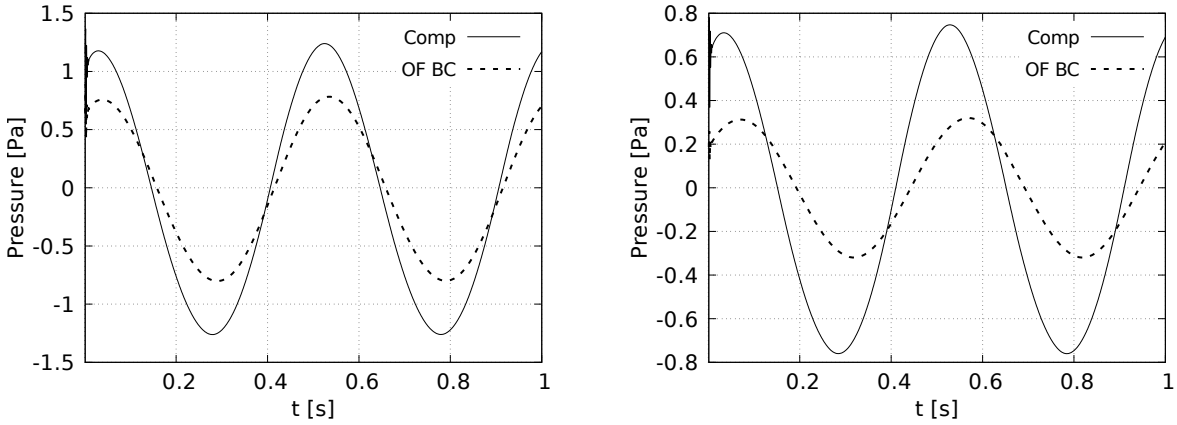

(a) Trachea probe (b) 1 generation probe

Figure 4-21.: Pressure vs time comparison. Wo = 8.29

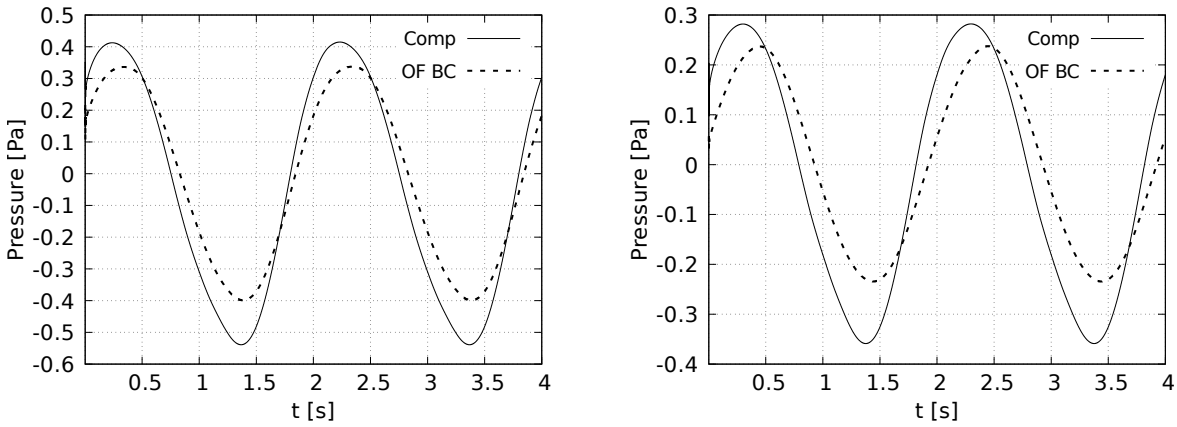

(a) Trachea probe (b) 1 generation probe

Figure 4-22.: Pressure vs time comparison. Wo = 4.14

of the constant pressure gradient between two points of a pipe. As indicated by Islam et al. [47], the pulsatile flow is driven by an oscillating pressure gradient, which can be defined as:

$$P = P_s + P_0 e^{iwt} \tag{4-13}$$

Where P is the pressure, P_s is the static pressure, i.e. the calculated pressure by Hagen-Poiseuille's law and P_0 is the pressure component generated by the oscillatory nature of the flow. This explains the reason for the underestimation of pressure using only Hagen-Poiseuille's law.

Figure **4-23** and Figure **4-24** show the behavior of velocity and pressure over time.

Under an oscillation condition, viscoelastic materials behave as a function of frequency. As indicated by Miri et al. [73], one of the main characteristics is the phase angle (δ), which varies between 0^o for a fully elastic material, between 0^o and 90^o for viscoelastic materials

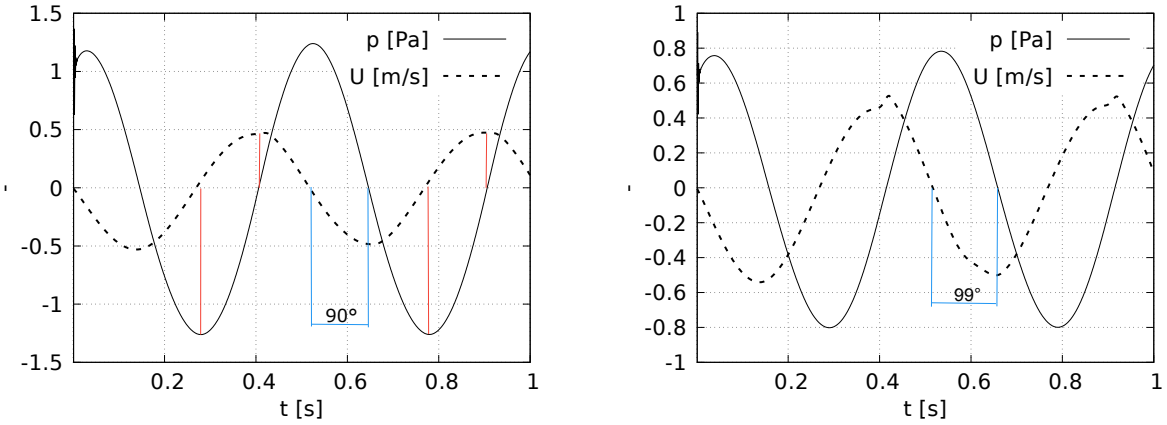

(a) Complete CFD (b) CFD + OF-BC

Figure 4-23.: Pressure and velocity vs time at trachea probe. Wo = 8.29

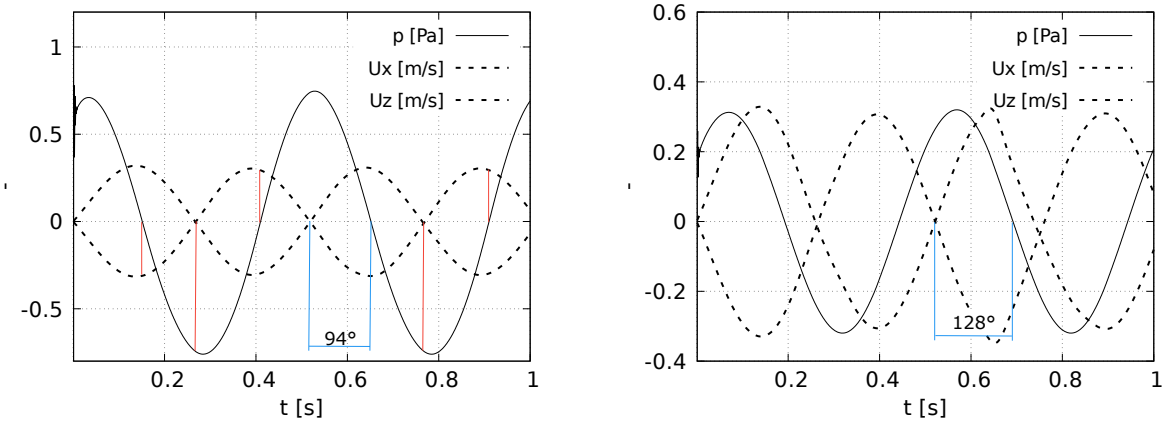

(a) Complete CFD (b) CFD + OF-BC

Figure 4-24.: Pressure and velocity vs time at generation 1 probe. Wo = 8.29. The red lines represent the points where for a maximum pressure, there is a minimum velocity.

and 90^o for a purely viscous fluid. For our case analysis this phase angle can be visualized through the pressure and velocity curves. For the phase angle measurement, it is calculated for each sensor (in the complete CFD simulation) how much x-axis advance equals $\pi/2$, i.e. 90^o. Thus, for the case of the trachea, the advance equivalent to 90^o is 0.125 s, and for the first generation sensor it is 0.118 s. As shown in Figure **4-23** (a) and Figure **4-24** (a), in both the tracheal sensor and the daughter branch sensor, an offset between the curves of approximately 90^o is evident. When the pressure is at a peak value, the velocity is almost at a value of 0, and vice versa (red lines in the graphs). For the tracheal sensor, this behavior is captured accurately using the OF-BC (Figure **4-23** (b)). However, in the first generation sensor this angle is far from 90^o (**4-24** (b)).

Analyzing the results obtained, it is observed that the *beta model* requires a correction in order to be applied to pulsating flows.

5. Conclusions and recommendations

5.1. Conclusions

In this research work, a study of different phenomena associated with the flow within human airways was developed. The main focus was on the application of techniques that simplify the complexity associated with the airways numerical simulations. A review on hybrid simulation methodologies applied to biofluids was developed, with the intention of recognizing the different strategies used for the simplification of this type of computational simulations. The first simplification implemented was a Spatial complexity reduction. This application consisted in the comparison between the use of synthetic vs. real patient-specific airway geometries, considering that synthetic models reduce the expense of modeling and complexity of airway geometry. The patient-specific model was segmented from computed tomography medical images. The synthetic model was based on the first 5 generations of the model proposed by Weibel. The results showed that, despite the geometrical differences between models, the pressure and shear stress distributions as well as the velocity streamlines were similar. Differences were found to be less than 5 % for peak velocity and 25 % for peak pressure. In fact, the wall pressure distributions show a similar trend for both models for each of the generations. Similarly, the wall shear stresses show a close distribution for the synthetic and real models, with the particularity that the bifurcation points of the synthetic model generate higher stress concentrations, due to the fact that they are straight joints. Anyhow, the maximum peak of WSS is reached in the real airways model, since the surfaces of these models, either by the process of segmentation or by the biological behavior of the airways walls, tend to present perturbations that act as a kind of stress concentrators. These results are shown as a confirmation for the extensive use of synthetic models in all types of numerical simulations, obtaining representative results that adequately capture the flow phenomena with respect to real patient-specific geometries, with the advantage of the parameterization and simplification of the geometric model itself. From this conclusion, a particular interest in the effect of some morphological parameters on the flow through the synthetic models was concerned. Specifically, the effect of the variation of the bifurcation angle (BA) and the carina rounding radius (CRR) on the flow. For this purpose, a series of numerical simulations were developed. The main focus was to detail and quantify the influence of the BA and CRR variations on the respiratory process examining both the inhalation and exhalation stages. Numerical experiments were performed on airway models set up for seven different angles and three rounding radius, using two symmetrical models (Weibel et al. [117] for BA analysis

and Lee et al. [59] model for CRR). The respiratory mechanisms of human inhalation and exhalation were decoupled and hence considered as independent processes in contrast with some previous works where pulsating flow is adopted (Xia et al. [123]; Adler and Brücker [1]; Bauer and Brücker [8]). During inhalation process, larger values for BA bring about a greater narrowing of the velocity profile, trendy to the inner wall on the coronal plane. In turn, velocity profiles on the sagittal plane show a deceleration across the axial axis. A local growth of the pressure drop is also observed with larger pressure values being obtained as the BA increases. This behaviour was specially noticeable in the region nearby the mean bifurcation. Maximum wall shear stress are developed at this point, and has a tendency to decrease as the angle increase. On the other hand, larger values of CRR are linked with the increment of the velocity across the bifurcation, as a higher pressure drop. For a straight joint, maximun WSS is located exactly in the joint, and it will be moving across the airway as the radius grows (and hence the smoothing). In both BA and CRR studies, there is evidence of a particular relationship between the vortical structures and the velocity an vorticity profiles. There are a dependency of the location of the peak velocity profile, the miminum vorticity magnitud and the saddle point (seen across the secondary patterns). This behaviour is kept as the velocity increase, even when new vortex appears. For exhalation process, an acceleration in the middle of the trachea is evidenced. This behaviour is greater for smaller BA in both coronal and sagittal planes. Moreover, the wall shear stress exhibits a particular increase in the first half of the branch for all cases. This behaviour may be related to the resistance and oscillations produced by the changes in the cross section area as the flow is transported through the branches. As in the inhalation process, there is a relationship between the V-W profiles and the vortical structures. Even in the trachea, where there is symmetry in the secondary flow patterns in both the coronal and sagittal planes, this behavior occurs in up to three points. It is important to mention that, in this exhalation stage, although changes of pressure drop and WSS were observed for the different BA, those were practically unnoticeable, making clear that these flow parameters are not really dependant of the BA in contrast to the effect appreciated during the inhalation stage.

A second approach to simplify and reduce complexity in airway simulations was implemented, using a hybrid simulation methodology. For this case, a 3D to 0D spatial reduction was developed, within the application and implementation of a pressure boundary condition (BC) based on human airway homothety factors. This BC, presented and validated in this work, provides an accurate tool to predict the pressure drop for a certain number of generations within the airway conduction zone. The derivation of the mathematical model starts with the assumption that the flow through the airways behaves like a Hagen-Poiseuille's flow. The bronchial tree is also considered to have a fractal geometry, which changes in size by constants known as homothety ratios. With these two assumptions, two pressure drop calculation models were presented: the *homothety model* and the *beta model*. A sensitivity analysis was carried out by generating random values for these ratios and to measure their influence on the final pressure calculation. A statistical analysis allows to determine that the effect of this

randomness does not strongly impact the pressure predictions, therefore the consideration of constant homothety ratios is justified. The condition was implemented through the open source OpenFOAM and tested with two Re numbers in the laminar regime and with several types of geometries. The results obtained show a good adjustment of the pressure with respect to those obtained by simulating the complete geometry. For low Reynolds numbers, the errors are within 10 %, even for the less slender pipes. However, for high Re numbers, the models predict with a higher error, ranging up to 20 %, and even 40 % for a system with very low slender branches. This indicates that the models perform well for velocity ranges not exceeding Re 2000, and with improved accuracy for slender branches. Likewise, the velocity and wall shear stress fields are also captured with about 10 % error rates. It is worth noting that the computational cost between full CFD modeling and the use of OF-BC was reduced in almost 3 times, obtaining improvements of more than 60 % in simulation times. Therefore, the use of OF-BC presents a good relationship between the reliability of the results and the computational cost. Two application cases were implemented to measure the robustness of the boundary condition. The first case was the analysis of airways in asthma condition. In this study, it was observed how this disease leads to more critical values, increasing pressure drop by more than 35 times and shear stress by more than 17 times. In addition, a validation with the work done by Tsega and Katiyar [111] yielded errors of about 10 % in the pressure prediction, thus demonstrating again the closeness of our mathematical model with a full CFD simulation. For the second case, a patient-specific airway model was employed to simulate a condition of airway collapse, considering a complete loss of branches on one side of the bronchial tree. The redistribution of wall shear stresses and streamline velocities leads to a critical condition in the zone of the collapsed airways, increasing up to 33 % the maximum WSS. An analysis of the behavior of the homothety boundary condition for pulsating flows was performed using the same geometry for the validation of the static pressure boundary condition. Two Womersley numbers were tested characterizing normal mechanical ventilation and high frequency oscillatory ventilation states. The results show how the boundary condition captures only a part of the pressure drop (the static part), but is not able to adjust to the effects produced by the oscillation itself. This is reflected in an underestimation of the pressure values over time, more noticeable for larger Wo. At the same time, it can be observed that the boundary also captures the phase angle between pressure and velocity for the trachea zone, but it is far from the expected value of 90Â° in the first generation. This shows that the boundary condition requires a modification to allow it to correctly include the oscillating effects, in order to be used in pulsatile flows.

5.2. Recommendations

The comparison study between synthetic and real patient-specific airway geometries was developed by applying only one model for both cases: the weibel model and a single medical image segmentation. Future work should focus on doing an analysis that covers a broader

spectrum of models (both synthetic and segmented), and thus generalize the results.
The results of the carina rounding radius effect were obtained only for the respiratory inhalation process. To complement the results, an analysis of the effect for respiratory exhalation is required.
An improvement of the perfomance of the boundary conditions based on homothety ratios for oscillating flows is necessary. As observed in the results, an adjustment at each time step is required for the algorithm to calculate more accurately the pressure drops.
The robustness and capability of boundary conditions including impedance is evidenced in the literature. In fact, it is observed how this inclusion allows to bring up the mechanical properties of the airway walls. Future work should be related to the implementation and adjustment of the homothety boundary condition taking into account the impedance of the bronchial tree.
As well as exploring a dimensional reduction methodology, it is also indispensable to investigate and implement coupled algorithms for the analysis of airway phenomena. Inclusions such as FSI to take into account the deformation of the airway walls, or DEM methods for particle inhalation analysis, which added to the reduction methodology already developed, lead to a robust model for multiphysics analysis.

A. Appendix: Compilation files for Boundary Conditions

A.1. pressureHomothetyAirwaysModel

A.1.1. pressureHomothetyAirwaysModel.C

```
/*---------------------------------------------------------------------------*\
  =========                 |
  \\      /  F ield         | OpenFOAM: The Open Source CFD Toolbox
   \\    /   O peration     |
    \\  /    A nd           | Copyright (C) 2011 OpenFOAM Foundation
     \\/     M anipulation  |
-------------------------------------------------------------------------------
License
    This file is part of OpenFOAM.

    OpenFOAM is free software: you can redistribute it and/or modify it
    under the terms of the GNU General Public License as published by
    the Free Software Foundation, either version 3 of the License, or
    (at your option) any later version.

    OpenFOAM is distributed in the hope that it will be useful, but WITHOUT
    ANY WARRANTY; without even the implied warranty of MERCHANTABILITY or
    FITNESS FOR A PARTICULAR PURPOSE.  See the GNU General Public License
    for more details.

    You should have received a copy of the GNU General Public License
    along with OpenFOAM.  If not, see <http://www.gnu.org/licenses/>.

\*---------------------------------------------------------------------------*/

#include "pressureHomothetyAirwaysModelFvPatchScalarField.H"
#include "addToRunTimeSelectionTable.H"
#include "fvPatchFieldMapper.H"
#include "volFields.H"
#include "surfaceFields.H"
#include "mathematicalConstants.H"

#define PI_ constant::mathematical::pi


// * * * * * * * * * * * * * * * * Constructors  * * * * * * * * * * * * * * * * //

Foam::pressureHomothetyAirwaysModelFvPatchScalarField::
pressureHomothetyAirwaysModelFvPatchScalarField
(
    const fvPatch& p,
    const DimensionedField<scalar, volMesh>& iF
)
:
    fixedValueFvPatchScalarField(p, iF),
    UName_("U"),
    phiName_("none"),
    rhoName_("none"),
    L0_(1.0),
    alpha1_(1.0),
    alpha2_(1.0),
    alpha3_(1.0),
    nu0_(0.0),
    N_(0.0),
```

```
    pRef_(p.size(), 0.0),
    r0_(1.0),
    factorP_(0.0),
    isFactorOK_(false),
    patchArea_(0.0),
    nNonOrthCorr_(0),
    nThisCorrections_(0)
{}


Foam::pressureHomothetyAirwaysModelFvPatchScalarField::
pressureHomothetyAirwaysModelFvPatchScalarField
(
    const fvPatch& p,
    const DimensionedField<scalar, volMesh>& iF,
    const dictionary& dict
)
:
    fixedValueFvPatchScalarField(p, iF),
    UName_(dict.lookupOrDefault<word>("U", "U")),
    phiName_(dict.lookupOrDefault<word>("phi", "phi")),
    rhoName_(dict.lookupOrDefault<word>("rho", "none")),
    L0_(readScalar(dict.lookup("L0"))),
    alpha1_(readScalar(dict.lookup("alpha1"))),
    alpha2_(readScalar(dict.lookup("alpha2"))),
    alpha3_(readScalar(dict.lookup("alpha3"))),
    nu0_(0.0),
    N_(readScalar(dict.lookup("N"))),
    pRef_("pRef", dict, p.size()),
    r0_(0.0),
    factorP_(0.0),
    isFactorOK_(false),
    patchArea_(0.0),
    nNonOrthCorr_(0),
    nThisCorrections_(0)
{
    //- Calculating initial value of pressure for the patch
    if (dict.found("value"))
    {
        fvPatchField<scalar>::operator=
        (
            scalarField("value", dict, p.size())
        );
    }
    else
    {
        fvPatchField<scalar>::operator=(pRef_);
    }

    //- Correct the values of area and radius
    Info<< nl << "Executing getPatchArea for patch : "<< this->patch().name() << endl;
    getPatchArea();
    Info<<"Executing correctRadius for patch : "<< this->patch().name() << endl;
    correctRadius();

    //- Get the multiplication factor of the tree
    if (!isFactorOK_)
    {
        Info<< "Executing calculateFactor  for patch : " << this->patch().name() << nl << endl;
        calculateFactor();
        isFactorOK_ = true;
    }

}


Foam::pressureHomothetyAirwaysModelFvPatchScalarField::
pressureHomothetyAirwaysModelFvPatchScalarField
(
    const pressureHomothetyAirwaysModelFvPatchScalarField& ptf,
    const fvPatch& p,
    const DimensionedField<scalar, volMesh>& iF,
    const fvPatchFieldMapper& mapper
)
:
    fixedValueFvPatchScalarField(ptf, p, iF, mapper),
    UName_(ptf.UName_),
    phiName_(ptf.phiName_),
    rhoName_(ptf.rhoName_),
    L0_(ptf.L0_),
    alpha1_(ptf.alpha1_),
    alpha2_(ptf.alpha2_),
```

```
    alpha3_(ptf.alpha3_),
    nu0_(ptf.nu0_),
    N_(ptf.N_),
    pRef_(ptf.pRef_, mapper),
    r0_(ptf.r0_),
    factorP_(ptf.factorP_),
    isFactorOK_(ptf.isFactorOK_),
    patchArea_(ptf.patchArea_),
    nNonOrthCorr_(ptf.nNonOrthCorr_),
    nThisCorrections_(ptf.nNonOrthCorr_)
{}


Foam::pressureHomothetyAirwaysModelFvPatchScalarField::
pressureHomothetyAirwaysModelFvPatchScalarField
(
    const pressureHomothetyAirwaysModelFvPatchScalarField& tppsf
)
:
    fixedValueFvPatchScalarField(tppsf),
    UName_(tppsf.UName_),
    phiName_(tppsf.phiName_),
    rhoName_(tppsf.rhoName_),
    L0_(tppsf.L0_),
    alpha1_(tppsf.alpha1_),
    alpha2_(tppsf.alpha2_),
    alpha3_(tppsf.alpha3_),
    nu0_(tppsf.nu0_),
    N_(tppsf.N_),
    pRef_(tppsf.pRef_),
    r0_(tppsf.r0_),
    factorP_(tppsf.factorP_),
    isFactorOK_(tppsf.isFactorOK_),
    patchArea_(tppsf.patchArea_),
    nNonOrthCorr_(tppsf.nNonOrthCorr_),
    nThisCorrections_(tppsf.nNonOrthCorr_)
{}


Foam::pressureHomothetyAirwaysModelFvPatchScalarField::
pressureHomothetyAirwaysModelFvPatchScalarField
(
    const pressureHomothetyAirwaysModelFvPatchScalarField& tppsf,
    const DimensionedField<scalar, volMesh>& iF
)
:
    fixedValueFvPatchScalarField(tppsf, iF),
    UName_(tppsf.UName_),
    phiName_(tppsf.phiName_),
    rhoName_(tppsf.rhoName_),
    L0_(tppsf.L0_),
    alpha1_(tppsf.alpha1_),
    alpha2_(tppsf.alpha2_),
    alpha3_(tppsf.alpha3_),
    nu0_(tppsf.nu0_),
    N_(tppsf.N_),
    pRef_(tppsf.pRef_),
    r0_(tppsf.r0_),
    factorP_(tppsf.factorP_),
    isFactorOK_(tppsf.isFactorOK_),
    patchArea_(tppsf.patchArea_),
    nNonOrthCorr_(tppsf.nNonOrthCorr_),
    nThisCorrections_(tppsf.nNonOrthCorr_)
{}


// * * * * * * * * * * * * * * * * Member Functions  * * * * * * * * * * * * * * * //

void Foam::pressureHomothetyAirwaysModelFvPatchScalarField::autoMap
(
    const fvPatchFieldMapper& m
)
{
    fixedValueFvPatchScalarField::autoMap(m);
    pRef_.autoMap(m);
}


void Foam::pressureHomothetyAirwaysModelFvPatchScalarField::rmap
(
    const fvPatchScalarField& ptf,
    const labelList& addr
```

```
)
{
    fixedValueFvPatchScalarField::rmap(ptf, addr);

    const pressureHomothetyAirwaysModelFvPatchScalarField& tiptf =
        refCast<const pressureHomothetyAirwaysModelFvPatchScalarField>(ptf);

    pRef_.rmap(tiptf.pRef_, addr);
}

void Foam::pressureHomothetyAirwaysModelFvPatchScalarField::getPatchArea
(
)
{
    scalar patchArea = gSum( patch().magSf() );

    reduce(patchArea, sumOp<scalar>());

    patchArea_ = patchArea ;

}

void Foam::pressureHomothetyAirwaysModelFvPatchScalarField::correctRadius
(
)
{
    if ( patchArea_ < SMALL )
    {
        r0_ = 2.0*SMALL;
    }
    else
    {
        r0_ = sqrt(patchArea_/PI_);
         Info<< "The calculated radius is   " << r0_ << endl;
    }

}

void Foam::pressureHomothetyAirwaysModelFvPatchScalarField::getViscosityValue
(
)
{
    const dictionary& transportProperties_ =
        this->db().objectRegistry::lookupObject<IOdictionary>("transportProperties");
    dimensionedScalar dimensionedNu_ = transportProperties_.lookup("nu", 0.0);
    nu0_ = dimensionedNu_.value() ;
}

void Foam::pressureHomothetyAirwaysModelFvPatchScalarField::calculateFactor
(
)
{
    factorP_ = (8.0 * nu0_ * L0_ )/(PI_ * pow(r0_,4)) *
        (-(alpha1_*alpha3_* pow(alpha2_,-4.0*N_) * (pow(alpha2_,4.0*N_)-pow(alpha3_,N_)
        *pow(alpha1_,N_)))/(alpha1_*alpha3_-pow(alpha2_,4)));
    Info<< "The calculated factorP is   " << factorP_ << endl;
}

void Foam::pressureHomothetyAirwaysModelFvPatchScalarField::updateCoeffs
(
    const scalarField& pRefp,
    const vectorField& Up,
    const scalar& factorPp
)
{

    if (this->updated())
    {
        return;
    };


    if (!isFactorOK_)
    {
        calculateFactor();
        isFactorOK_ = true;
    }

    getViscosityValue();

    if (phiName_ == "none" && rhoName_ == "none")
    {
```

```
        scalar patchFlux = (-1.0) * gSum( patch().Sf() & Up );

        reduce(patchFlux, sumOp<scalar>());

         Info<< "The calculated patch flux is   " << patchFlux << endl;

        operator==( factorPp* nu0_ * patchFlux + pRefp );

    }
    else if (rhoName_ == "none")
    {
        const fvsPatchField<scalar>& phip =
            patch().lookupPatchField<surfaceScalarField, scalar>(phiName_);

        scalar patchFlux = gSum( phip );

        reduce(patchFlux, sumOp<scalar>());

         Info<< "The calculated patch flux is   " << patchFlux << endl;

        operator==( factorPp* nu0_ * patchFlux + pRefp );

    }
    else
    {
        FatalErrorIn
        (
            "pressureHomothetyAirwaysModelFvPatchScalarField::updateCoeffs()"
        )   << " rho or phi set inconsistently, rho = " << rhoName_
            << ", phi = " << phiName_ << ".\n"
            << "    Set either rho or psi or neither depending on the "
               "definition of total pressure." << nl
            << "    Set the unused variable(s) to 'none'.\n"
            << "    on patch " << this->patch().name()
            << " of field " << this->dimensionedInternalField().name()
            << " in file " << this->dimensionedInternalField().objectPath()
            << exit(FatalError);
    }

    fixedValueFvPatchScalarField::updateCoeffs();

    // Info<< "This is the internal debug line A5: finished updateCoeffs  " << endl
    //     << "++++++++++++++++++++++++++++++++++++++" << nl << endl;
}


void Foam::pressureHomothetyAirwaysModelFvPatchScalarField::updateCoeffs()
{
    updateCoeffs
    (
        pRef(),
        patch().lookupPatchField<volVectorField, vector>(UName()),
        factorPp()
    );
}


void Foam::pressureHomothetyAirwaysModelFvPatchScalarField::write(Ostream& os) const
{
    fvPatchScalarField::write(os);
    writeEntryIfDifferent<word>(os, "U", "U", UName_);
    writeEntryIfDifferent<word>(os, "phi", "phi", phiName_);
    writeEntryIfDifferent<word>(os, "rho", "rho", rhoName_);
    os.writeKeyword("L0") << L0_ << token::END_STATEMENT << nl;
    os.writeKeyword("alpha1") << alpha1_ << token::END_STATEMENT << nl;
    os.writeKeyword("alpha2") << alpha2_ << token::END_STATEMENT << nl;
    os.writeKeyword("alpha3") << alpha3_ << token::END_STATEMENT << nl;
    os.writeKeyword("nu0") << nu0_ << token::END_STATEMENT << nl;
    os.writeKeyword("N") << N_ << token::END_STATEMENT << nl;
    pRef_.writeEntry("pRef", os);
    writeEntry("value", os);
}


// * * * * * * * * * * * * * * * * * * * * * * * * * * * * * * * * * * * * * //

namespace Foam
{
    makePatchTypeField
    (
        fvPatchScalarField,
        pressureHomothetyAirwaysModelFvPatchScalarField
```

```
    );
}

// ************************************************************************* //
```

A.1.2. pressureHomothetyAirwaysModel.H

```
/*---------------------------------------------------------------------------*\
  =========                 |
  \\      /  F ield         | OpenFOAM: The Open Source CFD Toolbox
   \\    /   O peration     |
    \\  /    A nd           | Copyright (C) 2011-2012 OpenFOAM Foundation
     \\/     M anipulation  |
-------------------------------------------------------------------------------
License
    This file is part of OpenFOAM.

    OpenFOAM is free software: you can redistribute it and/or modify it
    under the terms of the GNU General Public License as published by
    the Free Software Foundation, either version 3 of the License, or
    (at your option) any later version.

    OpenFOAM is distributed in the hope that it will be useful, but WITHOUT
    ANY WARRANTY; without even the implied warranty of MERCHANTABILITY or
    FITNESS FOR A PARTICULAR PURPOSE.  See the GNU General Public License
    for more details.

    You should have received a copy of the GNU General Public License
    along with OpenFOAM.  If not, see <http://www.gnu.org/licenses/>.

Class
    Foam::pressureHomothetyAirwaysModelFvPatchScalarField

Group
    grpInletBoundaryConditions grpOutletBoundaryConditions

Description
    This boundary condition provides a value of pressure for a bifurcated
    symmetrical airways model based on HOMOTHETY coeficients for LENGTH,
    RADIUS and VLOUMETRIC FLOW


    \heading Patch usage

    \table
        Property     | Description                                | Required    | Default value
        U            | velocity field name                        | yes         | U
        phi          | flux field name                            | yes         | phi
        rho          | fluid density                              | no          | rho
        L0           | Lentgh of last simulated generation        | yes         | L0
        alpha1       | Homothety Lenght factor                    | yes         | alpha1
        alpha2       | Homothety radius factor                    | yes         | alpha2
        alpha3       | Homothety Vol flow factor                  | yes         | alpha3
        N            | Number of missing generation               | yes         | N
        pref         | static pressure reference                  | no          | 0
    \endtable

    Example of the boundary condition specification:
    \verbatim
    myPatch
    {
        type            pressureHomothetyAirwaysModel;
        U               U;
        phi             phi;
        rho             none;
        beta            6;
        alpha2          0.8;
        alpha3          0.5;
        N               10;
        pRef            0;
    }
    \endverbatim

Note
    The default boundary behaviour is for subsonic, incompressible flow.
-------------------  ************************************  -------------------

SeeAlso
    Foam::fixedValueFvPatchField
```

```
    Boundary condition heavily based on the totalPressure BC

SourceFiles
    pressureHomothetyAirwaysModelFvPatchScalarField.C

\*---------------------------------------------------------------------------*/

#ifndef pressureHomothetyAirwaysModelFvPatchScalarField_H
#define pressureHomothetyAirwaysModelFvPatchScalarField_H

#include "fixedValueFvPatchFields.H"

// * * * * * * * * * * * * * * * * * * * * * * * * * * * * * * * * * * * * * //

namespace Foam
{

/*---------------------------------------------------------------------------*\
    Class pressureHomothetyAirwaysModelFvPatchScalarField Declaration
\*---------------------------------------------------------------------------*/

class pressureHomothetyAirwaysModelFvPatchScalarField
:
    public fixedValueFvPatchScalarField
{
    // Private data

        //- Name of the velocity field
        word UName_;

        //- Name of the flux transporting the field
        word phiName_;

        //- Name of the density field used to normalise the mass flux
        word rhoName_;

        //- Reference Length at the Zero generation of the tree
        scalar L0_;

        //- Lentgth - Diameter ratio
        scalar alpha1_;

        //- Homothety coefficient for radius
        scalar alpha2_;

        //- Homothety coefficient for volumetric flow rate
        scalar alpha3_;

        //- Dynamic viscosity at the Zero generation of the tree
        scalar nu0_;

        //- Number of missing generations for this patch or partial tree
        scalar N_;

        //- Reference pressure at the end of the branchial tree
        scalarField pRef_;

        //- Reference radius at the Zero generation of the tree
        scalar r0_;

        //- new pressure calculated by formula
        scalar factorP_;

        //- Boolean to check if factor has been calculated yet or not.
        bool isFactorOK_;

        //- Scalar with the value of the area of the patch
        scalar patchArea_;


        //- number of non Orthogonal correctors
        int nNonOrthCorr_;
        int nThisCorrections_;

        //- Boolean to check if the BC has already been calculated, in a time step

public:

    //- Runtime type information
    TypeName("pressureHomothetyAirwaysModel");
```

```
// Constructors

    //- Construct from patch and internal field
    pressureHomothetyAirwaysModelFvPatchScalarField
    (
        const fvPatch&,
        const DimensionedField<scalar, volMesh>&
    );

    //- Construct from patch, internal field and dictionary
    pressureHomothetyAirwaysModelFvPatchScalarField
    (
        const fvPatch&,
        const DimensionedField<scalar, volMesh>&,
        const dictionary&
    );

    //- Construct by mapping given a
    //  pressureHomothetyAirwaysModelFvPatchScalarField
    //  onto a new patch
    pressureHomothetyAirwaysModelFvPatchScalarField
    (
        const pressureHomothetyAirwaysModelFvPatchScalarField&,
        const fvPatch&,
        const DimensionedField<scalar, volMesh>&,
        const fvPatchFieldMapper&
    );

    //- Construct as copy
    pressureHomothetyAirwaysModelFvPatchScalarField
    (
        const pressureHomothetyAirwaysModelFvPatchScalarField&
    );

    //- Construct and return a clone
    virtual tmp<fvPatchScalarField> clone() const
    {
        return tmp<fvPatchScalarField>
        (
            new pressureHomothetyAirwaysModelFvPatchScalarField(*this)
        );
    }

    //- Construct as copy setting internal field reference
    pressureHomothetyAirwaysModelFvPatchScalarField
    (
        const pressureHomothetyAirwaysModelFvPatchScalarField&,
        const DimensionedField<scalar, volMesh>&
    );

    //- Construct and return a clone setting internal field reference
    virtual tmp<fvPatchScalarField> clone
    (
        const DimensionedField<scalar, volMesh>& iF
    ) const
    {
        return tmp<fvPatchScalarField>
        (
            new pressureHomothetyAirwaysModelFvPatchScalarField(*this, iF)
        );
    }


// Member functions

    // Access

        //- Return the name of the velocity field
        const word& UName() const
        {
            return UName_;
        }

        //- Return reference to the name of the velocity field
        //  to allow adjustment
        word& UName()
        {
            return UName_;
        }

        //- Return the name of the flux field
        const word& phiName() const
```

```
{
    return phiName_;
}

//- Return reference to the name of the flux field
//  to allow adjustment
word& phiName()
{
    return phiName_;
}

//- Return the name of the density field
const word& rhoName() const
{
    return rhoName_;
}

//- Return reference to the density field
word& rhoName()
{
    return rhoName_;
}

//- Return the radius of the branch zero (parent)
scalar L0() const
{
    return L0_;
}

//- Return reference to  the radius of the branch zero (parent)
scalar& L0()
{
    return L0_;
}

//- Return the Homothety coefficient for the length
scalar alpha1() const
{
    return alpha1_;
}

//- Return reference to the Homothety coefficient for the length
scalar& alpha1()
{
    return alpha1_;
}

//- Return the Homothety coefficient for the radius
scalar alpha2() const
{
    return alpha2_;
}

//- Return reference to the Homothety coefficient for the radius
scalar& alpha2()
{
    return alpha2_;
}

//- Return the Homothety coefficient for the volumetric flow rate
scalar alpha3() const
{
    return alpha3_;
}

//- Return reference to the Homothety coefficient for
//  the volumetric flow rate
scalar& alpha3()
{
    return alpha3_;
}

//- Return the Dynamic viscosity
//  (as a non-dimensional scalar) at the branch zero (parent)
scalar nu0() const
{
    return nu0_;
}

//- Return reference to the Dynamic viscosity
//  (as a non-dimensional scalar) at the branch zero (parent)
scalar& nu0()
```

```
    {
        return nu0_;
    }

    //- Return the number of missing generations
    scalar N() const
    {
        return N_;
    }

    //- Return reference to the number of missing generations
    scalar& N()
    {
        return N_;
    }

    //- Return the reference pressure
    const scalarField& pRef() const
    {
        return pRef_;
    }

    //- Return reference to the reference pressure to allow adjustment
    scalarField& pRef()
    {
        return pRef_;
    }

    //- Return the radius of the branch zero (parent)
    scalar r0() const
    {
        return r0_;
    }

    //- Return reference to  the radius of the branch zero (parent)
    scalar& r0()
    {
        return r0_;
    }

    //- Return the factor for new pressure
    scalar factorPp() const
    {
        return factorP_;
    }

    //- Return reference to  the factor for new pressure
    scalar& factorPp()
    {
        return factorP_;
    }


// Mapping functions

    //- Map (and resize as needed) from self given a mapping object
    virtual void autoMap
    (
        const fvPatchFieldMapper&
    );

    //- Reverse map the given fvPatchField onto this fvPatchField
    virtual void rmap
    (
        const fvPatchScalarField&,
        const labelList&
    );


// Evaluation functions
//
//  //- Evaluate the "zero" branch (parent) resistant
    void calculateFactor
    (
    );

    //- Calculate the area of the patch
    void getPatchArea
    (
    );

    //- Calculate the area of the patch
```

```
            void correctRadius
            (
            );

            //- Get viscosity value from main database
            void getViscosityValue
            (
            );

            //- Update the coefficients associated with the patch field
            //  using the given patch total pressure and velocity fields
            virtual void updateCoeffs
            (
                const scalarField& pRefp,
                const vectorField& Up,
                const scalar& factorPp
            );

            //- Update the coefficients associated with the patch field
            virtual void updateCoeffs();


        //- Write
        virtual void write(Ostream&) const;
};


// * * * * * * * * * * * * * * * * * * * * * * * * * * * * * * * * * * * * * * * * * * * * //

} // End namespace Foam

// * * * * * * * * * * * * * * * * * * * * * * * * * * * * * * * * * * * * * * * * * * * * //

#endif

// ************************************************************************* //
```

A.2. pressureBetaAirwaysModel

A.2.1. pressureBetaAirwaysModel.C

```
/*---------------------------------------------------------------------------*\
  =========                 |
  \\      /  F ield         | OpenFOAM: The Open Source CFD Toolbox
   \\    /   O peration     |
    \\  /    A nd           | Copyright (C) 2011 OpenFOAM Foundation
     \\/     M anipulation  |
-------------------------------------------------------------------------------
License
    This file is part of OpenFOAM.

    OpenFOAM is free software: you can redistribute it and/or modify it
    under the terms of the GNU General Public License as published by
    the Free Software Foundation, either version 3 of the License, or
    (at your option) any later version.

    OpenFOAM is distributed in the hope that it will be useful, but WITHOUT
    ANY WARRANTY; without even the implied warranty of MERCHANTABILITY or
    FITNESS FOR A PARTICULAR PURPOSE.  See the GNU General Public License
    for more details.

    You should have received a copy of the GNU General Public License
    along with OpenFOAM.  If not, see <http://www.gnu.org/licenses/>.

\*---------------------------------------------------------------------------*/

#include "pressureBetaAirwaysModelFvPatchScalarField.H"
#include "addToRunTimeSelectionTable.H"
#include "fvPatchFieldMapper.H"
#include "volFields.H"
#include "surfaceFields.H"
#include "mathematicalConstants.H"

#define PI_ constant::mathematical::pi
```

```
// * * * * * * * * * * * * * * * * * * Constructors  * * * * * * * * * * * * * * * * * * //

Foam::pressureBetaAirwaysModelFvPatchScalarField::
pressureBetaAirwaysModelFvPatchScalarField
(
    const fvPatch& p,
    const DimensionedField<scalar, volMesh>& iF
)
:
    fixedValueFvPatchScalarField(p, iF),
    UName_("U"),
    phiName_("none"),
    rhoName_("none"),
    beta_(0.0),
    alpha2_(0.0),
    alpha3_(0.0),
    nu0_(0.0),
    N_(0.0),
    pRef_(p.size(), 0.0),
    r0_(1.0),
    factorP_(0.0),
    isFactorOK_(false),
    patchArea_(0.0),
    nNonOrthCorr_(0),
    nThisCorrections_(0)
{}


Foam::pressureBetaAirwaysModelFvPatchScalarField::
pressureBetaAirwaysModelFvPatchScalarField
(
    const fvPatch& p,
    const DimensionedField<scalar, volMesh>& iF,
    const dictionary& dict
)
:
    fixedValueFvPatchScalarField(p, iF),
    UName_(dict.lookupOrDefault<word>("U", "U")),
    phiName_(dict.lookupOrDefault<word>("phi", "phi")),
    rhoName_(dict.lookupOrDefault<word>("rho", "none")),
    beta_(readScalar(dict.lookup("beta"))),
    alpha2_(readScalar(dict.lookup("alpha2"))),
    alpha3_(readScalar(dict.lookup("alpha3"))),
    nu0_(0.0),
    N_(readScalar(dict.lookup("N"))),
    pRef_("pRef", dict, p.size()),
    r0_(0.0),
    factorP_(0.0),
    isFactorOK_(false),
    patchArea_(0.0),
    nNonOrthCorr_(0),
    nThisCorrections_(0)
{

    //- Calculating initial value of pressure for the patch
    if (dict.found("value"))
    {
        fvPatchField<scalar>::operator=
        (
            scalarField("value", dict, p.size())
        );
    }
    else
    {
        fvPatchField<scalar>::operator=(pRef_);
    }

    //- Correct the values of area and radius
    Info<< nl << "Executing getPatchArea for patch : "<< this->patch().name() << endl;
    getPatchArea();
    Info<<"Executing correctRadius for patch : "<< this->patch().name() << endl;
    correctRadius();

    //- Get the multiplication factor of the tree
    if (!isFactorOK_)
    {
        Info<< "Executing calculateFactor  for patch : " << this->patch().name() << nl << endl;
        calculateFactor();
        isFactorOK_ = true;
    }

}
```

```
Foam::pressureBetaAirwaysModelFvPatchScalarField::
pressureBetaAirwaysModelFvPatchScalarField
(
    const pressureBetaAirwaysModelFvPatchScalarField& ptf,
    const fvPatch& p,
    const DimensionedField<scalar, volMesh>& iF,
    const fvPatchFieldMapper& mapper
)
:
    fixedValueFvPatchScalarField(ptf, p, iF, mapper),
    UName_(ptf.UName_),
    phiName_(ptf.phiName_),
    rhoName_(ptf.rhoName_),
    beta_(ptf.beta_),
    alpha2_(ptf.alpha2_),
    alpha3_(ptf.alpha3_),
    nu0_(ptf.nu0_),
    N_(ptf.N_),
    pRef_(ptf.pRef_, mapper),
    r0_(ptf.r0_),
    factorP_(ptf.factorP_),
    isFactorOK_(ptf.isFactorOK_),
    patchArea_(ptf.patchArea_),
    nNonOrthCorr_(ptf.nNonOrthCorr_),
    nThisCorrections_(ptf.nNonOrthCorr_)
{}


Foam::pressureBetaAirwaysModelFvPatchScalarField::
pressureBetaAirwaysModelFvPatchScalarField
(
    const pressureBetaAirwaysModelFvPatchScalarField& tppsf
)
:
    fixedValueFvPatchScalarField(tppsf),
    UName_(tppsf.UName_),
    phiName_(tppsf.phiName_),
    rhoName_(tppsf.rhoName_),
    beta_(tppsf.beta_),
    alpha2_(tppsf.alpha2_),
    alpha3_(tppsf.alpha3_),
    nu0_(tppsf.nu0_),
    N_(tppsf.N_),
    pRef_(tppsf.pRef_),
    r0_(tppsf.r0_),
    factorP_(tppsf.factorP_),
    isFactorOK_(tppsf.isFactorOK_),
    patchArea_(tppsf.patchArea_),
    nNonOrthCorr_(tppsf.nNonOrthCorr_),
    nThisCorrections_(tppsf.nNonOrthCorr_)
{}


Foam::pressureBetaAirwaysModelFvPatchScalarField::
pressureBetaAirwaysModelFvPatchScalarField
(
    const pressureBetaAirwaysModelFvPatchScalarField& tppsf,
    const DimensionedField<scalar, volMesh>& iF
)
:
    fixedValueFvPatchScalarField(tppsf, iF),
    UName_(tppsf.UName_),
    phiName_(tppsf.phiName_),
    rhoName_(tppsf.rhoName_),
    beta_(tppsf.beta_),
    alpha2_(tppsf.alpha2_),
    alpha3_(tppsf.alpha3_),
    nu0_(tppsf.nu0_),
    N_(tppsf.N_),
    pRef_(tppsf.pRef_),
    r0_(tppsf.r0_),
    factorP_(tppsf.factorP_),
    isFactorOK_(tppsf.isFactorOK_),
    patchArea_(tppsf.patchArea_),
    nNonOrthCorr_(tppsf.nNonOrthCorr_),
    nThisCorrections_(tppsf.nNonOrthCorr_)
{}


// * * * * * * * * * * * * * * * * Member Functions  * * * * * * * * * * * * * * * * //
```

```
void Foam::pressureBetaAirwaysModelFvPatchScalarField::autoMap
(
    const fvPatchFieldMapper& m
)
{
    fixedValueFvPatchScalarField::autoMap(m);
    pRef_.autoMap(m);
}


void Foam::pressureBetaAirwaysModelFvPatchScalarField::rmap
(
    const fvPatchScalarField& ptf,
    const labelList& addr
)
{
    fixedValueFvPatchScalarField::rmap(ptf, addr);

    const pressureBetaAirwaysModelFvPatchScalarField& tiptf =
        refCast<const pressureBetaAirwaysModelFvPatchScalarField>(ptf);

    pRef_.rmap(tiptf.pRef_, addr);
}

void Foam::pressureBetaAirwaysModelFvPatchScalarField::getPatchArea
(
)
{
    scalar patchArea = gSum( patch().magSf() );

    reduce(patchArea, sumOp<scalar>());

    patchArea_ = patchArea ;
         Info<< "The calculated area is    " << patchArea_ << endl;

}

void Foam::pressureBetaAirwaysModelFvPatchScalarField::correctRadius
(
)
{
    if ( patchArea_ < SMALL )
    {
        r0_ = 2.0*SMALL;
    }
    else
    {
        r0_ = sqrt(patchArea_/PI_);
         Info<< "The calculated radius is    " << r0_ << endl;
    }

}

void Foam::pressureBetaAirwaysModelFvPatchScalarField::getViscosityValue
(
)
{
    const dictionary& transportProperties_ =
        this->db().objectRegistry::lookupObject<IOdictionary>("transportProperties");
    dimensionedScalar dimensionedNu_ = transportProperties_.lookup("nu", 0.0);
    nu0_ = dimensionedNu_.value() ;
}


void Foam::pressureBetaAirwaysModelFvPatchScalarField::calculateFactor
(
)
{
    factorP_ = (16.0 * beta_ )/(PI_ * pow(r0_,3)) *
        (alpha3_* pow(alpha2_,-3.0*N_) * (pow(alpha2_,3.0*N_)-pow(alpha3_,N_)))/(pow(alpha2_,3)-alpha3_);
    Info<< "The calculated factorP is    " << factorP_ << endl;
}

void Foam::pressureBetaAirwaysModelFvPatchScalarField::updateCoeffs
(
    const scalarField& pRefp,
    const vectorField& Up,
    const scalar& factorPp
)
{
```

```
    if (this->updated())
    {
        return;
    };

    if (!isFactorOK_)
    {
        calculateFactor();
        isFactorOK_ = true;
    }

    getViscosityValue();


    if (phiName_ == "none" && rhoName_ == "none")
    {
        scalar patchFlux = sum( patch().Sf() & Up );

        reduce(patchFlux, sumOp<scalar>());

         Info<< "The calculated patch flux is   " << patchFlux << endl;

        operator==( factorPp * nu0_ * patchFlux + pRefp );

    }

    else if (rhoName_ == "none")
    {
        const fvsPatchField<scalar>& phip =
            patch().lookupPatchField<surfaceScalarField, scalar>(phiName_);

        scalar patchFlux = gSum( phip );

        reduce(patchFlux, sumOp<scalar>());

         Info<< "The calculated patch flux is   " << patchFlux << endl;

        operator==( factorPp * nu0_ * patchFlux + pRefp );

    }
    else
    {
        FatalErrorIn
        (
            "pressureBetaAirwaysModelFvPatchScalarField::updateCoeffs()"
        )   << " rho or phi set inconsistently, rho = " << rhoName_
            << ", phi = " << phiName_ << ".\n"
            << "    Set either rho or psi or neither depending on the "
               "definition of total pressure." << nl
            << "    Set the unused variable(s) to 'none'.\n"
            << "    on patch " << this->patch().name()
            << " of field " << this->dimensionedInternalField().name()
            << " in file " << this->dimensionedInternalField().objectPath()
            << exit(FatalError);
    }

    fixedValueFvPatchScalarField::updateCoeffs();

}


void Foam::pressureBetaAirwaysModelFvPatchScalarField::updateCoeffs()
{
    updateCoeffs
    (
        pRef(),
        patch().lookupPatchField<volVectorField, vector>(UName()),
        factorPp()
    );
}


void Foam::pressureBetaAirwaysModelFvPatchScalarField::write(Ostream& os) const
{
    fvPatchScalarField::write(os);
    writeEntryIfDifferent<word>(os, "U", "U", UName_);
    writeEntryIfDifferent<word>(os, "phi", "phi", phiName_);
    writeEntryIfDifferent<word>(os, "rho", "rho", rhoName_);
    os.writeKeyword("beta") << beta_ << token::END_STATEMENT << nl;
    os.writeKeyword("alpha2") << alpha2_ << token::END_STATEMENT << nl;
    os.writeKeyword("alpha3") << alpha3_ << token::END_STATEMENT << nl;
    os.writeKeyword("nu0") << nu0_ << token::END_STATEMENT << nl;
```

```
    os.writeKeyword("N") << N_ << token::END_STATEMENT << nl;
    pRef_.writeEntry("pRef", os);
    writeEntry("value", os);
}


// * * * * * * * * * * * * * * * * * * * * * * * * * * * * * * * * * * * * * * * * * * * * * * * * * * * * * //

namespace Foam
{
    makePatchTypeField
    (
        fvPatchScalarField,
        pressureBetaAirwaysModelFvPatchScalarField
    );
}

// ************************************************************************* //
```

A.2.2. pressureBetaAirwaysModel.H

```
/*---------------------------------------------------------------------------*\
  =========                 |
  \\      /  F ield         | OpenFOAM: The Open Source CFD Toolbox
   \\    /   O peration     |
    \\  /    A nd           | Copyright (C) 2011-2012 OpenFOAM Foundation
     \\/     M anipulation  |
-------------------------------------------------------------------------------
License
    This file is part of OpenFOAM.

    OpenFOAM is free software: you can redistribute it and/or modify it
    under the terms of the GNU General Public License as published by
    the Free Software Foundation, either version 3 of the License, or
    (at your option) any later version.

    OpenFOAM is distributed in the hope that it will be useful, but WITHOUT
    ANY WARRANTY; without even the implied warranty of MERCHANTABILITY or
    FITNESS FOR A PARTICULAR PURPOSE.  See the GNU General Public License
    for more details.

    You should have received a copy of the GNU General Public License
    along with OpenFOAM.  If not, see <http://www.gnu.org/licenses/>.

Class
    Foam::pressureBetaAirwaysModelFvPatchScalarField

Group
    grpInletBoundaryConditions grpOutletBoundaryConditions

Description
    This boundary condition provides a value of pressure for a bifurcated
    symmetrical airways model based on HOMOTHETY coeficients for LENGTH,
    RADIUS and VLOUMETRIC FLOW


    \heading Patch usage

    \table
        Property     | Description                                | Required    | Default value
        U            | velocity field name                        | yes         | U
        phi          | flux field name                            | yes         | phi
        rho          | fluid density                              | no          | rho
        beta         | Lenght/diameter relation                   | yes         | alpha1
        alpha2       | Homothety radius factor                    | yes         | alpha2
        alpha3       | Homothety Vol flow factor                  | yes         | alpha3
        N            | Number of missing generation               | yes         | N
        pref         | static pressure reference                  | no          | 0
    \endtable

    Example of the boundary condition specification:
    \verbatim
    myPatch
    {
        type            pressureBetaAirwaysModel;
        U               U;
        phi             phi;
        rho             none;
        beta            6;
        alpha2          0.8;
```

```
        alpha3          0.5;
        N               10;
        pRef            0;
    }
    \endverbatim

Note
    The default boundary behaviour is for subsonic, incompressible flow.
-------------------  ************************************  -------------------

SeeAlso
    Foam::fixedValueFvPatchField
    Boundary condition heavily based on the totalPressure BC

SourceFiles
    pressureBetaAirwaysModelFvPatchScalarField.C

\*---------------------------------------------------------------------------*/

#ifndef pressureBetaAirwaysModelFvPatchScalarField_H
#define pressureBetaAirwaysModelFvPatchScalarField_H

#include "fixedValueFvPatchFields.H"

// * * * * * * * * * * * * * * * * * * * * * * * * * * * * * * * * * * * * * //

namespace Foam
{

/*---------------------------------------------------------------------------*\
    Class pressureBetaAirwaysModelFvPatchScalarField Declaration
\*---------------------------------------------------------------------------*/

class pressureBetaAirwaysModelFvPatchScalarField
:
    public fixedValueFvPatchScalarField
{
    // Private data

        //- Name of the velocity field
        word UName_;

        //- Name of the flux transporting the field
        word phiName_;

        //- Name of the density field used to normalise the mass flux
        word rhoName_;

        //- Lentgth - Diameter ratio
        scalar beta_;

        //- Homothety coefficient for radius
        scalar alpha2_;

        //- Homothety coefficient for volumetric flow rate
        scalar alpha3_;

        //- Dynamic viscosity at the Zero generation of the tree
        scalar nu0_;

        //- Number of missing generations for this patch or partial tree
        scalar N_;

        //- Reference pressure at the end of the branchial tree
        scalarField pRef_;

        //- Reference radius at the Zero generation of the tree
        scalar r0_;

        //- new pressure calculated by formula
        scalar factorP_;

        //- Boolean to check if factor has been calculated yet or not.
        bool isFactorOK_;

        //- Scalar with the value of the area of the patch
        scalar patchArea_;


        //- number of non Orthogonal correctors
        int nNonOrthCorr_;
        int nThisCorrections_;
```

```
        //- Boolean to check if the BC has already been calculated, in a time step

public:

    //- Runtime type information
    TypeName("pressureBetaAirwaysModel");


    // Constructors

        //- Construct from patch and internal field
        pressureBetaAirwaysModelFvPatchScalarField
        (
            const fvPatch&,
            const DimensionedField<scalar, volMesh>&
        );

        //- Construct from patch, internal field and dictionary
        pressureBetaAirwaysModelFvPatchScalarField
        (
            const fvPatch&,
            const DimensionedField<scalar, volMesh>&,
            const dictionary&
        );

        //- Construct by mapping given a
        //  pressureBetaAirwaysModelFvPatchScalarField
        //  onto a new patch
        pressureBetaAirwaysModelFvPatchScalarField
        (
            const pressureBetaAirwaysModelFvPatchScalarField&,
            const fvPatch&,
            const DimensionedField<scalar, volMesh>&,
            const fvPatchFieldMapper&
        );

        //- Construct as copy
        pressureBetaAirwaysModelFvPatchScalarField
        (
            const pressureBetaAirwaysModelFvPatchScalarField&
        );

        //- Construct and return a clone
        virtual tmp<fvPatchScalarField> clone() const
        {
            return tmp<fvPatchScalarField>
            (
                new pressureBetaAirwaysModelFvPatchScalarField(*this)
            );
        }

        //- Construct as copy setting internal field reference
        pressureBetaAirwaysModelFvPatchScalarField
        (
            const pressureBetaAirwaysModelFvPatchScalarField&,
            const DimensionedField<scalar, volMesh>&
        );

        //- Construct and return a clone setting internal field reference
        virtual tmp<fvPatchScalarField> clone
        (
            const DimensionedField<scalar, volMesh>& iF
        ) const
        {
            return tmp<fvPatchScalarField>
            (
                new pressureBetaAirwaysModelFvPatchScalarField(*this, iF)
            );
        }


    // Member functions

        // Access

            //- Return the name of the velocity field
            const word& UName() const
            {
                return UName_;
            }
```

```
//- Return reference to the name of the velocity field
//  to allow adjustment
word& UName()
{
    return UName_;
}

//- Return the name of the flux field
const word& phiName() const
{
    return phiName_;
}

//- Return reference to the name of the flux field
//  to allow adjustment
word& phiName()
{
    return phiName_;
}

//- Return the name of the density field
const word& rhoName() const
{
    return rhoName_;
}

//- Return reference to the density field
word& rhoName()
{
    return rhoName_;
}

//- Return the Homothety coefficient for the length
scalar beta() const
{
    return beta_;
}

//- Return reference to the Homothety coefficient for the length
scalar& beta()
{
    return beta_;
}

//- Return the Homothety coefficient for the radius
scalar alpha2() const
{
    return alpha2_;
}

//- Return reference to the Homothety coefficient for the radius
scalar& alpha2()
{
    return alpha2_;
}

//- Return the Homothety coefficient for the volumetric flow rate
scalar alpha3() const
{
    return alpha3_;
}

//- Return reference to the Homothety coefficient for
//  the volumetric flow rate
scalar& alpha3()
{
    return alpha3_;
}

//- Return the Dynamic viscosity
//  (as a non-dimensional scalar) at the branch zero (parent)
scalar nu0() const
{
    return nu0_;
}

//- Return reference to the Dynamic viscosity
//  (as a non-dimensional scalar) at the branch zero (parent)
scalar& nu0()
{
    return nu0_;
}
```

```
        //- Return the number of missing generations
        scalar N() const
        {
            return N_;
        }

        //- Return reference to the number of missing generations
        scalar& N()
        {
            return N_;
        }

        //- Return the reference pressure
        const scalarField& pRef() const
        {
            return pRef_;
        }

        //- Return reference to the reference pressure to allow adjustment
        scalarField& pRef()
        {
            return pRef_;
        }

        //- Return the radius of the branch zero (parent)
        scalar r0() const
        {
            return r0_;
        }

        //- Return reference to  the radius of the branch zero (parent)
        scalar& r0()
        {
            return r0_;
        }

        //- Return the factor for new pressure
        scalar factorPp() const
        {
            return factorP_;
        }

        //- Return reference to  the factor for new pressure
        scalar& factorPp()
        {
            return factorP_;
        }


    // Mapping functions

        //- Map (and resize as needed) from self given a mapping object
        virtual void autoMap
        (
            const fvPatchFieldMapper&
        );

        //- Reverse map the given fvPatchField onto this fvPatchField
        virtual void rmap
        (
            const fvPatchScalarField&,
            const labelList&
        );


    // Evaluation functions
    //
    //  //- Evaluate the "zero" branch (parent) resistant
        void calculateFactor
        (
        );

        //- Calculate the area of the patch
        void getPatchArea
        (
        );

        //- Calculate the area of the patch
        void correctRadius
        (
        );
```

```
            //- Get viscosity value from main database
            void getViscosityValue
            (
            );

            //- Update the coefficients associated with the patch field
            //  using the given patch total pressure and velocity fields
            virtual void updateCoeffs
            (
                const scalarField& pRefp,
                const vectorField& Up,
                const scalar& factorPp
            );

            //- Update the coefficients associated with the patch field
            virtual void updateCoeffs();


        //- Write
        virtual void write(Ostream&) const;
};


// * * * * * * * * * * * * * * * * * * * * * * * * * * * * * * * * * * * * * * * * * * * * //

} // End namespace Foam

// * * * * * * * * * * * * * * * * * * * * * * * * * * * * * * * * * * * * * * * * * * * * //

#endif

// ************************************************************************* //
```

Bibliografía

[1] Katrin Adler and Christoph Brücker. Dynamic flow in a realistic model of the upper human lung airways. *Experiments in Fluids*, 43(2):411–423, 2007.

[2] S Manuchehr Alavi, Theodore E Keats, and William M O'Brien. The angle of tracheal bifurcation: its normal mensuration. *American Journal of Roentgenology*, 108(3):546–549, 1970.

[3] Andrea Aliverti and Antonio Pedotti. *Mechanics of breathing: new insights from new technologies*. Springer, 2014.

[4] WJ Bair. The icrp human respiratory tract model for radiological protection. *Radiation Protection Dosimetry*, 60(4):307–310, 1995.

[5] Maria C Basil and Edward E Morrisey. Respiratory bronchioles: a unique structure in the human lung. *Lung Stem Cells in Development, Health and Disease*, 91:114, 2021.

[6] Jason HT Bates. *Lung mechanics: an inverse modeling approach*. Cambridge University Press, 2009.

[7] K Bauer and Ch Brücker. The role of ventilation frequency in airway reopening. *Journal of Biomechanics*, 42(8):1108–1113, 2009.

[8] Katrin Bauer and Christoph Brücker. The influence of airway tree geometry and ventilation frequency on airflow distribution. *Journal of biomechanical engineering*, 137(8), 2015.

[9] Mehdi Behbahani, M Behr, M Hormes, U Steinseifer, D Arora, O Coronado, and M Pasquali. A review of computational fluid dynamics analysis of blood pumps. *European Journal of Applied Mathematics*, 20(4):363–397, 2009.

[10] Tim Behrens. Openfoam's basic solvers for linear systems of equations. *Chalmers, Department of Applied Mechanics*, 18(02), 2009.

[11] Philipp Berg, Gabor Janiga, and Dominique Thevenin. Investigation of the unsteady blood flow in cerebral aneurysms with stent using the open-source software openfoam®. In *Proc. Open Source CFD International Conference (OSCIC)*, pages 1–8, 2011.

[12] Bruno Blais, David Vidal, Francois Bertrand, Gregory S Patience, and Jamal Chaouki. Experimental methods in chemical engineering: Discrete element methodâ€"dem. *The Canadian Journal of Chemical Engineering*, 97(7):1964–1973, 2019.

[13] Pablo J Blanco, Márcio R Pivello, Santiago A Urquiza, and Raúl A Feijóo. Building coupled 3d–1d–0d models in computational hemodynamics. In *1st International Conference on Mathematical and Computational Biomedical Engineering-CMBE2009*, 2009.

[14] Mark Brouns, Santhosh T Jayaraju, Chris Lacor, Johan De Mey, Marc Noppen, Walter Vincken, and Sylvia Verbanck. Tracheal stenosis: a flow dynamics study. *Journal of Applied Physiology*, 102(3):1178–1184, 2007.

[15] Rajnish Kaur Calay, Jutarat Kurujareon, and Arne Erik Holdø. Numerical simulation of respiratory flow patterns within human lung. *Respiratory physiology & neurobiology*, 130(2):201–221, 2002.

[16] João PF Campos, Karla RB Melo, and Gabriela C Lopes. Implementation, validation and application of a lubrication force model in cfd-dem simulations. *Brazilian Journal of Chemical Engineering*, 39(2):429–440, 2022.

[17] E García Castillo, M Chicot Llano, DA Rodríguez Serrano, and E Zamora García. Ventilación mecánica no invasiva e invasiva. *Medicine-Programa de Formación Médica Continuada Acreditado*, 11(63):3759–3767, 2014.

[18] Kwang K Chang, Ki Beom Kim, Mark W McQuilling, and Reza Movahed. Fluid structure interaction simulations of the upper airway in obstructive sleep apnea patients before and after maxillomandibular advancement surgery. *American Journal of Orthodontics and Dentofacial Orthopedics*, 153(6):895–904, 2018.

[19] Jie Chen, Xi-Yun Lu, and Wen Wang. Non-newtonian effects of blood flow on hemodynamics in distal vascular graft anastomoses. *Journal of Biomechanics*, 39(11): 1983–1995, 2006.

[20] JT Chen, Charles E Putman, Laurence W Hedlund, NS Dahmash, and L Roberts. Widening of the subcarinal angle by pericardial effusion. *American Journal of Roentgenology*, 139(5):883–887, 1982.

[21] Xiaole Chen, Wenqi Zhong, Xianguang Zhou, Baosheng Jin, and Baobin Sun. Cfd–dem simulation of particle transport and deposition in pulmonary airway. *Powder technology*, 228:309–318, 2012.

[22] Jiwoong Choi, Guohua Xia, Merryn H Tawhai, Eric A Hoffman, and Ching-Long Lin. Numerical study of high-frequency oscillatory air flow and convective mixing in a ct-based human airway model. *Annals of biomedical engineering*, 38(12):3550–3571, 2010.

[23] Rajesh Chowdhary, Virendra Singh, AE Tattersfield, SD Sharma, Subir Kar, and AB Gupta. Relationship of flow and cross-sectional area to frictional stress in airway models of asthma. *Journal of Asthma*, 36(5):419–426, 1999.

[24] Simoni Christou, Thanasis Chatziathanasiou, Stelios Angeli, Pantelis Koullapis, Fotos Stylianou, Josué Sznitman, Haiwei Henry Guo, and Stavros C Kassinos. Anatomical variability in the upper tracheobronchial tree: sex-based differences and implications for personalized inhalation therapies. *Journal of Applied Physiology*, 130(3):678–707, 2021.

[25] Dogan Ciloglu and Adem Karaman. A numerical simulation of the airflow and aerosol particle deposition in a realistic airway model of a healthy adult. *Journal of Pharmaceutical Sciences*, 2022.

[26] Mitchel J Colebank, M Umar Qureshi, Sudarshan Rajagopal, Richard A Krasuski, and Mette S Olufsen. A multiscale model of vascular function in chronic thromboembolic pulmonary hypertension. *American Journal of Physiology-Heart and Circulatory Physiology*, 321(2):H318–H338, 2021.

[27] Patricia Corieri. *Experimental and numerical investigation of flows in bifurcations within lung airways*. PhD thesis, Ph. D. thesis, von Karman Institute for Fluid Dynamics, Université Libre de â€¦, 1994.

[28] HL Dailey, HC Yalcin, and SN Ghadiali. Fluid-structure modeling of flow-induced alveolar epithelial cell deformation. *Computers & structures*, 85(11-14):1066–1071, 2007.

[29] JW De Backer, WG Vos, CD Gorlé, P Germonpré, B Partoens, FL Wuyts, Paul M Parizel, and W De Backer. Flow analyses in the lower airways: patient-specific model and boundary conditions. *Medical engineering & physics*, 30(7):872–879, 2008.

[30] Wo R Dean. Xvi. note on the motion of fluid in a curved pipe. *The London, Edinburgh, and Dublin Philosophical Magazine and Journal of Science*, 4(20):208–223, 1927.

[31] Zhenya Fan, David W Holmes, Emilie Sauret, Mohammad S Islam, Suvash C Saha, Zoran Ristovski, and YuanTong Gu. A multiscale modeling method incorporating spatial coupling and temporal coupling into transient simulations of the human airways. *International Journal for Numerical Methods in Fluids*, 93(9):2905–2920, 2021.

[32] Yu Feng and Clement Kleinstreuer. Ddpm-dem simulations of particulate flows in human tracheobronchial airways. In *ASME International Mechanical Engineering Congress and Exposition*, volume 56222, page V03BT03A030. American Society of Mechanical Engineers, 2013.

[33] Jerry Fine. *Applied biofluid mechanics*. McGraw-Hill Education, 2017.

[34] Brendan T Finucane, Albert H Santora, and Ban Chi-Ho Tsui. *Principles of airway management*. Springer, 2003.

[35] Luca Formaggia, Alfio Quarteroni, and Allesandro Veneziani. *Cardiovascular Mathematics: Modeling and simulation of the circulatory system*, volume 1. Springer Science & Business Media, 2010.

[36] Frank E Fresconi and Ajay K Prasad. Secondary velocity fields in the conducting airways of the human lung. *Journal of Biomechanical Engineering*, 129:722–732, 2007.

[37] Lennart Fries, Sergiy Antonyuk, Stefan Heinrich, Daniel Dopfer, and Stefan Palzer. Collision dynamics in fluidised bed granulators: A dem-cfd study. *Chemical engineering science*, 86:108–123, 2013.

[38] Manikantam G Gaddam and Arvind Santhanakrishnan. Effects of varying inhalation duration and respiratory rate on human airway flow. *Fluids*, 6(6):221, 2021.

[39] T Gemci, Valery Ponyavin, Y Chen, H Chen, and R Collins. Computational model of airflow in upper 17 generations of human respiratory tract. *Journal of Biomechanics*, 41(9):2047–2054, 2008.

[40] AS Green. Modelling of peak-flow wall shear stress in major airways of the lung. *Journal of Biomechanics*, 37(5):661–667, 2004.

[41] Fernando Gutiérrez Muñoz. Ventilación mecánica. *Acta médica peruana*, 28(2):87–104, 2011.

[42] Pamela H Haskin and Lawrence R Goodman. Normal tracheal bifurcation angle: a reassessment. *American Journal of Roentgenology*, 139(5):879–882, 1982.

[43] Beatriz Herranz, María Dolores Álvarez, and Jara Pérez-Jiménez. Association of plasma and urine viscosity with cardiometabolic risk factors and oxidative status. a pilot study in subjects with abdominal obesity. *PloS one*, 13(10):e0204075, 2018.

[44] Werner Hofmann. Modelling inhaled particle deposition in the human lungâ€"a review. *Journal of Aerosol Science*, 42(10):693–724, 2011.

[45] K Horsfield and G Cumming. Angles of branching and diameters of branches in the human bronchial tree. *The Bulletin of mathematical biophysics*, 29(2):245–259, 1967.

[46] Keith Horsfield, Gladys Dart, Dan E Olson, Giles F Filley, and Gordon Cumming. Models of the human bronchial tree. *Journal of applied physiology*, 31(2):207–217, 1971.

[47] Md Mahfuzul Islam, Huiru Li, Huidan Yu, and Xiaoping Du. Physics-based regression vs. cfd for hagen-poiseuille and womersley flows and uncertainty quantification. In *Eleventh International Conference on Computational Fluid Dynamics*, volume ICCFD11, pages ICCFD11–3301. ICCFD, 2022.

[48] M Ismail, A Comerford, and WA3130232 Wall. Coupled and reduced dimensional modeling of respiratory mechanics during spontaneous breathing. *International journal for numerical methods in biomedical engineering*, 29(11):1285–1305, 2013.

[49] Dalibor Jajcevic, Eva Siegmann, Charles Radeke, and Johannes G Khinast. Large-scale cfd–dem simulations of fluidized granular systems. *Chemical Engineering Science*, 98: 298–310, 2013.

[50] M Elshin Joel and M Anburajan. 3d modeling of stenotic internal carotid artery treated with stent: a cfd analysis of blood. In *International Conference on Computer, Networks and Communication Engineering (ICCNCE 2013)*, pages 148–151. Atlantis Press, 2013.

[51] Nasrul Hadi Johari, Jegatis Balaiyah, and Zulkifli Ahmad. Effect of chronic obstructive pulmonary disease on airflow motion using computational fluid dynamics analysis. In *2014 International Conference on Computer, Communications, and Control Technology (I4CT)*, pages 249–254. IEEE, 2014.

[52] Roger D Kamm. Airway wall mechanics. *Annual review of biomedical engineering*, 1 (1):47–72, 1999.

[53] Min-Yeong Kang, Jeongeun Hwang, and Jin-Won Lee. Effect of geometric variations on pressure loss for a model bifurcation of the human lung airway. *Journal of biomechanics*, 44(6):1196–1199, 2011.

[54] Bipinchandra Khade, AR Waheed, Nisha Yadav, and CV Diwan. Study of sub carinal angle of human trachea by computerized tomography. *Int J Anat Res*, 4(3):2828–32, 2016.

[55] Hyoung-Ho Kim, Young Ho Choi, Seung Bae Lee, Yasutaka Baba, Kyung-Wuk Kim, and Sang-Ho Suh. Numerical analysis of the urine flow in a stented ureter with no peristalsis. *Bio-medical materials and engineering*, 26(s1):S215–S223, 2015.

[56] J Kren, Miroslav Horák, F Zát'ura, and Mít'a Rosenberg. Mathematical model of the male urinary tract. *Biomedical Papers of the Medical Faculty of the University Palacky, Olomouc, Czechoslovakia*, 145(2):91–96, 2001.

[57] Swashna Lal. *Assessing the Impact of E-cigarette Particle Size on Aerosol Transport and Deposition in the Lung*. PhD thesis, ResearchSpace@ Auckland, 2022.

[58] Bart N Lambrecht and Hamida Hammad. The immunology of asthma. *Nature immunology*, 16(1):45–56, 2015.

[59] Dongyoub Lee, Seong S Park, George A Ban-Weiss, Michelle V Fanucchi, Charles G Plopper, and Anthony S Wexler. Bifurcation model for characterization of pulmonary architecture. *The Anatomical Record: Advances in Integrative Anatomy and Evolutionary Biology: Advances in Integrative Anatomy and Evolutionary Biology*, 291(4): 379–389, 2008.

[60] Michael G Levitzky. *Pulmonary physiology*, volume 1. : McGraw-Hill Education,, 2018.

[61] Tina A Lewis, Yang-Sheng Tzeng, Erin L McKinstry, Angela C Tooker, Kwansoo Hong, Yanping Sun, Joey Mansour, Zachary Handler, and Mitchell S Albert. Quantification of airway diameters and 3d airway tree rendering from dynamic hyperpolarized 3he magnetic resonance imaging. *Magnetic Resonance in Medicine: An Official Journal of the International Society for Magnetic Resonance in Medicine*, 53(2):474–478, 2005.

[62] Chen Lin, Jui-Heng Lee, and Chih-Min Hsieh. The correlation between subcarinal angle and left atrial volume. *Age (years old)*, 67(16.4):15–96, 2012.

[63] Yang Liu, RMC So, and CH Zhang. Modeling the bifurcating flow in a human lung airway. *Journal of biomechanics*, 35(4):465–473, 2002.

[64] Duncan A Lockerby, Carlos A Duque-Daza, Matthew K Borg, and Jason M Reese. Time-step coupling for hybrid simulations of multiscale flows. *Journal of Computational Physics*, 237:344–365, 2013.

[65] M Malve, S Chandra, JL Lopez-Villalobos, EA Finol, A Ginel, and M Doblare. Cfd analysis of the human airways under impedance-based boundary conditions: application to healthy, diseased and stented trachea. *Computer methods in biomechanics and biomedical engineering*, 16(2):198–216, 2013.

[66] Benoit Mandelbrot. *Fractals*. Freeman San Francisco, 1977.

[67] Elaine N Marieb and K Hoehn. Urinary system. *Essentials of Human Anatomy and Physiology*, pages 501–526, 2006.

[68] TB Martonen, Y Yang, and ZQ Xue. Effects of carinal ridge shapes on lung airstreams. *Aerosol science and technology*, 21(2):119–136, 1994.

[69] TB Martonen, X Guan, and RM Schreck. Fluid dynamics in airway bifurcations: I. primary flows. *Inhalation toxicology*, 13(4):261–279, 2001.

[70] Benjamin Mauroy, M Filoche, ER Weibel, and B Sapoval. An optimal bronchial tree may be dangerous. *Nature*, 427(6975):633–636, 2004.

[71] Puneet Mehra. *Fluid-Structure Interaction Modeling of Human Upper Airway Collapse in Obstructive Sleep Apnea*. PhD thesis, University of Cincinnati, 2019.

[72] Douglas J Minnich and Douglas J Mathisen. Anatomy of the trachea, carina, and bronchi. *Thoracic surgery clinics*, 17(4):571–585, 2007.

[73] Taghi Miri et al. Viscosity and oscillatory rheology. *Practical food rheology: An interpretive approach*, pages 7–28, 2011.

[74] Joe J Monaghan. Smoothed particle hydrodynamics. *Annual review of astronomy and astrophysics*, 30:543–574, 1992.

[75] Joseph J Monaghan. Smoothed particle hydrodynamics and its diverse applications. *Annual Review of Fluid Mechanics*, 44:323–346, 2012.

[76] JG Murray, AL Brown, EA Anagnostou, and R Senior. Widening of the tracheal bifurcation on chest radiographs: value as a sign of left atrial enlargement. *AJR. American journal of roentgenology*, 164(5):1089–1092, 1995.

[77] Justus Kavita Mutuku, Wei-Hsin Chen, et al. Flow characterization in healthy airways and airways with chronic obstructive pulmonary disease (copd) during different inhalation conditions. *Aerosol and Air Quality Research*, 18(10):2680–2694, 2018.

[78] Achuth Nair Balachandran Nair, Stefan Pirker, and Mahdi Saeedipour. Resolved cfd-dem simulation of blood flow with a reduced-order rbc model. *Computational Particle Mechanics volume*, 9:759–774, 2021.

[79] Pietro Nardelli, Kashif A Khan, Alberto Corvò, Niamh Moore, Mary J Murphy, Maria Twomey, Owen J Oâ€™Connor, Marcus P Kennedy, Raúl San José Estépar, Michael M Maher, et al. Optimizing parameters of an open-source airway segmentation algorithm using different ct images. *Biomedical engineering online*, 14(1):1–24, 2015.

[80] Matthew E Nipper and J Brandon Dixon. Engineering the lymphatic system. *Cardiovascular engineering and technology*, 2(4):296–308, 2011.

[81] Yang-Yao Niu and Ding-Yu Chang. Cfd simulation of shear stress and secondary flows in urethra. *Biomedical Engineering: Applications, Basis and Communications*, 19(02): 117–127, 2007.

[82] Mette S Olufsen. Structured tree outflow condition for blood flow in larger systemic arteries. *American journal of physiology-Heart and circulatory physiology*, 276(1): H257–H268, 1999.

[83] Mette S Olufsen, Charles S Peskin, Won Yong Kim, Erik M Pedersen, Ali Nadim, and Jesper Larsen. Numerical simulation and experimental validation of blood flow in arteries with structured-tree outflow conditions. *Annals of biomedical engineering*, 28 (11):1281–1299, 2000.

[84] Jesús Manuel Fernández Oro. *Técnicas numéricas en ingeniería de fluidos: introducción a la dinámica de fluidos computacional (CFD) por el método de volúmenes finitos*. Reverté, 2012.

[85] Marco Paggi, Andrea Amicarelli, and Pietro Lenarda. Sph modelling of hydrodynamic lubrication along rough surfaces. *Lubricants*, 7(12):103, 2019.

[86] TJ Pedley, RC Schroter, and MF Sudlow. Energy losses and pressure drop in models of human airways. *Respiration physiology*, 9(3):371–386, 1970.

[87] TJ Pedley, RC Schroter, and MF Sudlow. The prediction of pressure drop and variation of resistance within the human bronchial airways. *Respiration physiology*, 9(3):387–405, 1970.

[88] TJ Pedley, RC Schroter, and MF Sudlow. Flow and pressure drop in systems of repeatedly branching tubes. *Journal of Fluid Mechanics*, 46(2):365–383, 1971.

[89] K Perktold and D Hilbert. Numerical simulation of pulsatile flow in a carotid bifurcation model. *Journal of biomedical engineering*, 8(3):193–199, 1986.

[90] Svetla Petkova, Alamgir Hossain, Jamal Naser, and Enzo Palombo. Cfd modelling of blood flow in portal vein hypertension with and without thrombosis. In *Third International Conference on CFD in the Minerals and Process Industries CSIRO, Melborne, Australia*, pages 10–12, 2003.

[91] AK Politis, GP Stavropoulos, MN Christolis, FG Panagopoulos, NS Vlachos, and NC Markatos. Numerical modeling of simulated blood flow in idealized composite arterial coronary grafts: Steady state simulations. *Journal of Biomechanics*, 40(5): 1125–1136, 2007.

[92] R Ponzini, R Da Vià, S Bnà, C Cottini, and A Benassi. Coupled cfd-dem model for dry powder inhalers simulation: validation and sensitivity analysis for the main model parameters. *Powder Technology*, 385:199–226, 2021.

[93] Christian J Roth, Mahmoud Ismail, Lena Yoshihara, and Wolfgang A Wall. A comprehensive computational human lung model incorporating inter-acinar dependencies: Application to spontaneous breathing and mechanical ventilation. *International journal for numerical methods in biomedical engineering*, 33(1):e02787, 2017.

[94] Christian J Roth, Lena Yoshihara, Mahmoud Ismail, and Wolfgang A Wall. Computational modelling of the respiratory system: discussion of coupled modelling approaches and two recent extensions. *Computer Methods in Applied Mechanics and Engineering*, 314:473–493, 2017.

[95] Conor A Ruzycki, Emadeddin Javaheri, and Warren H Finlay. The use of computational fluid dynamics in inhaler design. *Expert opinion on drug delivery*, 10(3):307–323, 2013.

[96] Daisy Sahni, Yatindra Kumar Batra, and Subramanyam Rajeev. Anatomical dimensions of trachea, main bronchi, subcarinal and bronchial angles in fetuses measured ex vivo. *Pediatric Anesthesia*, 18(11):1029–1034, 2008.

[97] Andreas Schmidt, Stephan Zidowitz, Andres Kriete, Thorsten Denhard, Stefan Krass, and Heinz-Otto Peitgen. A digital reference model of the human bronchial tree. *Computerized Medical Imaging and Graphics*, 28(4):203–211, 2004.

[98] RC Schroter and MF Sudlow. Flow patterns in models of the human bronchial airways. *Respiration physiology*, 7(3):341–355, 1969.

[99] Enrico Sciubba. A critical reassessment of the hess–murray law. *Entropy*, 18(8):283, 2016.

[100] Shahrokh Shahriari and Damien Garcia. Meshfree simulations of ultrasound vector flow imaging using smoothed particle hydrodynamics. *Physics in Medicine & Biology*, 63(20):205011, 2018.

[101] Lauralee Sherwood. The urinary system. *Human physiology from cells to system. 8th ed. Canada: Brooks/Cole*, pages 504–26, 2013.

[102] Yubing Shi, Patricia Lawford, and Rodney Hose. Review of zero-d and 1-d models of blood flow in the cardiovascular system. *Biomedical engineering online*, 10(1):1–38, 2011.

[103] Pejman Shojaee and Hanieh Niroomand-Oscuii. Cfd analysis of drug uptake and elimination through vascularized cancerous tissue. *Biomedical Physics & Engineering Express*, 5(3):035032, 2019.

[104] Rakesh Kumar Shukla, Vivek Kumar Srivastav, Akshoy Ranjan Paul, and Anuj Jain. Fluid structure interaction studies of human airways. *Sādhanā*, 45(1):1–6, 2020.

[105] Venkataramana K Sidhaye, Kelly S Schweitzer, Michael J Caterina, Larissa Shimoda, and Landon S King. Shear stress regulates aquaporin-5 and airway epithelial barrier function. *Proceedings of the National Academy of Sciences*, 105(9):3345–3350, 2008.

[106] B Snyder and DE Olson. Flow development in a model airway bronchus. *Journal of Fluid Mechanics*, 207:379–392, 1989.

[107] Brooke N Steele, Mette S Olufsen, and Charles A Taylor. Fractal network model for simulating abdominal and lower extremity blood flow during resting and exercise conditions. *Computer Methods in Biomechanics and Biomedical Engineering*, 10(1): 39–51, 2007.

[108] Carlos Jose Suarez, Suzanne M Dintzis, and Charles W Frevert. Respiratory. In *Comparative anatomy and histology*, pages 121–134. Elsevier, 2012.

[109] Melody A Swartz. The physiology of the lymphatic system. *Advanced drug delivery reviews*, 50(1-2):3–20, 2001.

[110] Shahab Taherian, Hamid Rahai, Bernardo Z Gomez, Thomas Waddington, and Jeremy R Bonifacio. Tracheal stenosis: a cfd approach for evaluation of drug delivery. In *ASME International Mechanical Engineering Congress and Exposition*, volume 57380, page V003T03A096. American Society of Mechanical Engineers, 2015.

[111] E Tsega and V Katiyar. Numerical simulations of inspiratory airflow in healthy and asthmatic human airways. *Am J Biomed Eng*, 9:5–12, 2019.

[112] Caroline Van Ertbruggen, Charles Hirsch, and Manuel Paiva. Anatomically based three-dimensional model of airways to simulate flow and particle transport using computational fluid dynamics. *Journal of applied physiology*, 98(3):970–980, 2005.

[113] Lorenzo Vasquez Giuliano, Antonio Buffo, Marco Vanni, Alessandra Sabina Lanotte, Valentina Arima, Monica Bianco, Francesca Baldassarre, and Graziano Frungieri. Response of shear-activated nanotherapeutic particles in a clot-obstructed blood vessel by cfd-dem simulations. *The Canadian Journal of Chemical Engineering*, 2022.

[114] Xiang-Qi Wang, Arun S Mujumdar, and Christopher Yap. Effect of bifurcation angle in tree-shaped microchannel networks. *Journal of Applied Physics*, 102(7):073530, 2007.

[115] YUAN WANG. *CFD-DEM Simulation of Particle Transport and Deposition in Human Airway*. PhD thesis, Monash University, 2017.

[116] Mark A Warner and Bela Patel. Mechanical ventilation. *Benumof and Hagberg's airway management*, pages 981–997, 2013.

[117] Ewald R Weibel, Andre F Cournand, and Dickinson W Richards. *Morphometry of the human lung*, volume 1. Springer, 1963.

[118] Geoffrey B West, James H Brown, and Brian J Enquist. A general model for the origin of allometric scaling laws in biology. *Science*, 276(5309):122–126, 1997.

[119] John Burnard West. *Pulmonary pathophysiology: the essentials*. Lippincott Williams & Wilkins, 2008.

[120] John Burnard West. *Respiratory physiology: the essentials*. Lippincott Williams & Wilkins, 2012.

[121] BR Wiggs, R Moreno, JC Hogg, C Hilliam, and PD Pare. A model of the mechanics of airway narrowing. *Journal of Applied Physiology*, 69(3):849–860, 1990.

[122] BR Wiggs, C Bosken, PD Pare, A James, and JC Hogg. A model of airway narrowing in asthma and in chronic obstructive pulmonary disease1-3. *Am Rev Respir Dis*, 145: 1251–1258, 1992.

[123] Guohua Xia, Merryn H Tawhai, Eric A Hoffman, and Ching-Long Lin. Airway wall stiffening increases peak wall shear stress: a fluid–structure interaction study in rigid and compliant airways. *Annals of biomedical engineering*, 38(5):1836–1853, 2010.

[124] XL Yang, Yang Liu, RMC So, and JM Yang. The effect of inlet velocity profile on the bifurcation copd airway flow. *Computers in biology and medicine*, 36(2):181–194, 2006.

[125] Lena Yoshihara, Mahmoud Ismail, and Wolfgang A Wall. Bridging scales in respiratory mechanics. In *Computer Models in Biomechanics*, pages 395–407. Springer, 2013.

[126] Bin Zhang, Shuang Liu, Yinxia Liu, Bo Wu, Xuhui Zhang, Xin Wang, Xuezhi Liang, Xiaoming Cao, Dongwen Wang, and Chin-Lee Wu. Novel cfd modeling approaches to assessing urine flow in prostatic urethra after transurethral surgery. *Scientific Reports*, 11(1):1–9, 2021.

[127] Peng Zhang, Na Zhang, Yuefan Deng, and Danny Bluestein. A multiple time stepping algorithm for efficient multiscale modeling of platelets flowing in blood plasma. *Journal of computational physics*, 284:668–686, 2015.

[128] Yao Zhao and Baruch B Lieber. Steady inspiratory flow in a model symmetric bifurcation. *Journal of biomechanical engineering*, 116(4):488–496, 1994.